Reduction of combusted iron using hydrogen

Document status and date:
Published: 15/05/2023

Document Version:
Publisher's PDF, also known as Version of Record (includes final page, issue and volume numbers)

Please check the document version of this publication:

• A submitted manuscript is the version of the article upon submission and before peer-review. There can be important differences between the submitted version and the official published version of record. People interested in the research are advised to contact the author for the final version of the publication, or visit the DOI to the publisher's website.
• The final author version and the galley proof are versions of the publication after peer review.
• The final published version features the final layout of the paper including the volume, issue and page numbers.

Link to publication

Download date: 05. Oct. 2023

Reduction of combusted iron using hydrogen

Conrad Hessels

Reduction of combusted iron using hydrogen

PROEFSCHRIFT

ter verkrijging van de graad van doctor aan de Technische Universiteit Eindhoven, op gezag van de rector magnificus prof.dr. S.K. Lenaerts, voor een commissie aangewezen door het College voor Promoties, in het openbaar te verdedigen op maandag 15 mei 2023 om 13:30

door

Cornelius Josephus Maria Hessels

geboren te Breda

Dit proefschrift is goedgekeurd door de promotoren en de samenstelling van de promotiecommissie is als volgt:

voorzitter:	prof.dr.ir. D.M.J. Smeulders	
promotor:	prof.dr.ir. N.G. Deen	
copromotoren:	dr. Y. Tang	
	dr.ir. T.A.M. Homan	
leden:	prof.dr.ir. M.G.D. Geers	
	prof.dr.ir. J.R. van Ommen	(Technische Universiteit Delft)
	prof.dr. D. Pallarès	(Chalmers Tekniska Högskola)
adviseur:	dr. E.N. Makarova	(Pometon S.p.A.)

"Scale-up is still not an exact science, but is rather that mix of physics, mathematics, witchcraft, history and common sense that we call engineering."

John M. Matsen, 1997 [1]

TU/e EINDHOVEN UNIVERSITY OF TECHNOLOGY

Summary

The transition of renewable energy requires, besides the production of solar and wind energy, ways to efficiently store and transport large amounts of energy. Micron-sized iron powder has recently emerged as a promising dense energy carrier for such a carbon-neutral future via cyclic combustion and reduction, especially for seasonal storage and intercontinental transport. Iron is abundant, affordable, and non-toxic, while in powder form can be combusted in slightly altered (existing) power plants to produce energy based on demand. The combustion products (iron oxide) can be captured and reduced ("recharged"/"regenerated") back to iron powder using green hydrogen (hydrogen produced from renewable energy). This research focuses on experimentally investigating/exploring the intrinsic properties in and challenges of this reduction process.

Firstly, the intrinsic reaction rates of the reduction of iron oxide fines, produced by iron combustion, with hydrogen are investigated using thermogravimetric analysis. Isothermal reduction experiments are conducted at the temperature range of 400-900 °C and at hydrogen concentrations of 25-100 vol%. Scanning electron microscope images show that the morphology of the reduction products depends on the reduction temperature but not on the hydrogen concentration. Reduction at higher temperatures leads to larger pore sizes. Based on an extended Hancock-Sharp "lnln"-method the appropriate gas-solid reaction models are determined, suggesting that the reduction can be described by a single-step phase boundary-controlled reaction at temperatures below 600 °C, whereas a multistep mechanism is required for the description of reactions at higher temperatures. Sintering of the powder occurs above 600 °C, possibly limiting the reaction.

Therefore, sintering is studied in more detail in a packed bed reactor, at various temperatures under inert (nitrogen) and reducing (hydrogen) conditions. Compression tests are used to quantify the degree of sintering. A sintering model, based on the formation of a solid bridge through solid state diffusion of iron atoms, is used to match the experimental results. Sintering of combusted iron occurs at temperatures $\geq$ 575 °C in both nitrogen and hydrogen atmospheres and the sintering strength increases exponentially with temperature. It is found that the observed decrease in reduction rate at high temperatures is not caused by the sintering process but by the formation of wüstite as an intermediate species leading to the formation of a dense iron layer. Iron whiskers are found to form at high temperatures ($\geq$ 700 °C) in combination with low reduction rates ($\leq$ 25 vol% H_2), leading to the production of sub-micron fines, which should be avoided for health and safety reasons.

For industrial implementation of the reduction process, fluidized beds are more practical than packed bed reactors. Therefore, the reduction and fluidization behavior of combusted iron powder is studied in a lab-scale cylindrical fluidized bed in the last part of this research. The minimum fluidization velocity u_{mf} is measured as a function of temperature between 10 and 600 °C for both hydrogen and nitrogen as fluidizing gas. The results start to deviate from the existing Ergun correlation at temperatures above 285 °C, both for nitrogen and hydrogen. A new correlation, taking the cohesive inter-particle solid bridge force into account, is proposed in this work to predict the

minimum fluidization velocity at high temperature. 5 hours reduction experiments are carried out at constant excess velocity with 50, 75 and 100 vol% of H_2 and temperatures between 350 and 550 °C. Gradual defluidization occurs when the temperature exceeds 525 °C. A maximum reduction degree of 62% is obtained at 534 °C and 100 vol% H_2.

Overall, this research contributes to the understanding and development of iron oxide reduction using green hydrogen (green steelmaking) and the metal energy carrier cycle specifically.

Samenvatting

De omschakeling naar duurzame energie vereist, naast het opwekken van wind- en zonne-energie, ook een manier om grote hoeveelheden energie efficiënt op te slaan en te transporteren. Cyclische verbranding en reductie van ijzerpoeder heeft de potentie om een efficiënte energiedrager te worden, specifiek voor seizoenopslag en intercontinentaal transport. IJzer is een veelvoorkomend materiaal, is goedkoop, niet-giftig, en kan zeer waarschijnlijk (in poedervorm) verbrand worden in bestaande kolencentrales met minimale aanpassing. Het verbrande ijzerpoeder (nu ijzeroxide) kan gemakkelijk afgevangen en gereduceerd ("geregenereerd") worden met behulp van duurzaam geproduceerd waterstof. Dit onderzoek richt zich op het experimenteel bestuderen van dit reductieproces.

In de eerste plaats zijn de intrinsieke eigenschappen van de chemische reactie tussen ijzeroxide poeder, geproduceerd door ijzerpoederverbranding, met waterstof onderzocht, met behulp van "thermogravimetrische analyse". Experimenten op constante temperatuur zijn uitgevoerd op temperaturen tussen 400 en 900 °C en met waterstof concentraties van 25-100 vol%, waarbij de massa van het poeder nauwkeurig wordt bijgehouden in de tijd. Afbeeldingen, gemaakt met een elektronenmicroscoop, laten zien dat de morfologie van het gereduceerde poeder afhankelijk is van de reductietemperatuur, maar niet van de waterstofconcentratie. Reduceren op hogere temperaturen leidt tot de formatie van grotere poriën. Op basis van een verbeterde Hancock-Sharp "lnln"-methode is het reactiemechanisme ontrafelt. Hieruit blijkt dat de reductie op lage temperatuur < 600 °C beschreven kan worden door een één-traps kinetische gelimiteerd krimpende kern model. Op hogere temperaturen blijkt een meer-traps mechanisme nodig te zijn voor het beschrijven van het reductiegedrag. Boven de 600°C treed sinteren van deeltjes op, waardoor de reactie mogelijk wordt beperkt.

Het sinteren is daarom in meer detail bestudeert in een gepakte kolom reactor. Het sintergedrag is gemeten onder inerte (met stikstof) en reducerende (met waterstof) condities. Een drukbank is gebruikt om de mate van sinteren te kwantificeren. Een sintermodel, gebaseerd op het vormen van een vaste brug tussen poederdeeltjes door middel van diffusie van ijzeratomen, is gebruikt om de drukbank-resultaten verder te interpreteren. Sinteren van verbrand ijzerpoeder treedt op bij temperaturen vanaf 575 °C in een omgeving van zowel stikstof and waterstof, en neemt exponentieel toe met de temperatuur. De waargenomen afname van de reductiesnelheid bij hoge temperaturen blijkt niet veroorzaakt te worden door het sinteren, maar door de vorming van wüstiet als intermediaire ijzeroxide tijdens het reductieproces. Hoge temperaturen (≥ 700 °C) in combinatie met een lage waterstofconcentratie (≤ 25 vol% H_2) leidt tot de van ijzer-"haren" op het oppervlakte van de poederdeeltjes. Deze "haren" zijn fragiel en kunnen daardoor leiden tot (sub-)micron deeltjes, die vanwege gezondheidsredenen en explosiegevaar moeten worden vermeden.

Voor industriële toepassing en opschaling van het reductieproces zijn wervelbedden praktischer dan gepakte kolom reactoren. Daarom is, als laatste, het fluïdizatiegedrag van het verbrande poeder experimenteel onderzocht in een cilindrisch wervelbed. De minimale gassnelheid voor fluïdizatie (u_{mf}) is gemeten als functie van de temperatuur tussen 10 en 600 °C voor zowel waterstof als stikstof als fluïdisatiegas. De experi-

mentele resultaten beginnen af te wijken van de bestaande Ergun-vergelijking voor minimale gassnelheid vanaf temperaturen boven 285 °C, zowel voor stikstof als voor waterstof. In dit werk is daarom een nieuwe correlatie voorgesteld om de minimale gassnelheid bij hoge temperaturen te voorspellen, waarbij de krachten tussen deeltjes meegenomen wordt. Er zijn daarna reductie-experimenten van 5 uur uitgevoerd bij een constante overmaat aan gassnelheid (bovenop de minimale gassnelheid vereist voor fluïdizatie) op temperaturen tussen 350 en 550 °C en met waterstofconcentraties van 50, 75 en 100 vol%. Geleidelijke defluïdisatie treedt op vanaf 525 °C. Een maximale reductiegraad van 62% is bereikt bij 534 °C en met behulp van 100 vol% H_2.

Dit onderzoek draagt bij aan de verdere ontwikkeling van ijzeroxidereductie met behulp van waterstof (voor duurzame staalproductie) en draagt specifiek bij aan het gebruik van ijzer als energiedrager.

Contents

Nomenclature

Physical constants

g	gravitational constant, m^2/s
k	Boltzmann constant, J/K
R	molar gas constant, $J/(mol \cdot K)$

Variables

χ	molar fraction, -
δ	lattice spacing, m
η	dynamic viscosity, $Pa \cdot s$
γ	surface free energy, N/m
ψ	dimensionless constant, -
ρ	density, kg/m^3
σ	tensile strength, Pa
ε	void fraction, -
ξ	empirical factor, -
A	cross-sectional/projected area, m^2
a	curvature radius, m
C	concentration, mol/m^3
D	bed diameter, m
D_s	surface diffusion coefficient, m^2/s
$D_{0,s}$	frequency factor, m^2/s
d_{32}	Sauter mean diameter, m
E_a	activation energy, J/mol
f	mathematical function, -
F_c	cohesive force, N
g	mathematical function, -
H	static bed height, m
K	equilibrium constant, -
k_{app}	apparent reaction rate, 1/s

M	molar mass, kg/mol
m	mass, kg
N	total amount, -
n	Avrami exponent, -
p	pressure, Pa
T	temperature, K
t	time, s
u	fluid velocity, m/s
v	relative particle velocity, m/s
W	pellet diameter, m
X	reduction degree / conversion, -
x	neck radius, m

Subscript

0	superficial / initial
b	bulk
e	excess
F	iron (ferrite)
g	gas
H	hematite
i,j	components
inf	final
melt	melting
mf	minimum fluidization
M	magnetite
n	normalized
p	particle
sb	solid bridge
s	solid
tot	total
W	wüstite

1 Introduction

1

Abstract

The worlds switch to renewable energy will lead to a large mismatch between energy supply and demand, both spatially and temporally. This leads to a need to transport and store renewable energy. Iron powder has certain characteristics that make it a promising energy carrier, especially for seasonal storage and intercontinental energy transport. A cyclic process of combustion and regeneration (reduction) can be envisioned. Different processes currently exist for iron oxide/ore reduction, which are briefly mentioned. Finally, an outline of the thesis is given.

1.1 Motivation

Humans hunger for energy and its appetite for fossil fuels has caused a significant rise in global temperatures and changes of our climate with irreversible consequences. Several "climate tipping points" might have already been surpassed [2]. It is therefore urgent to reduce our fossil fuel usage and replace it with renewable energy. The European Union has committed to this goal by implementing policies to reduce the net greenhouse gas emissions by at least 55% by 2030 compared to 1990 and becoming climate neutral by 2050 [3]. However, renewable energies pose a challenge in the form of energy storage and transport, due to the fluctuating production capacity. Seasonal (summer-winter) mismatches, for countries further from the equator, require vast amounts of energy to be stored efficiently and safely. Assuming 100% domestic production from wind and solar energy, this requires ~ 200 PJ of seasonal storage capacity (around 10% of the total energy demand) for the Netherlands, based on data from "Energie Beheer Nederland" (EBN) [4].

Moreover, not all locations are suitable or efficient for renewable energy production. Places closer to the equator obtain more solar energy year-round and places close to oceans typically endure more and stronger winds. It might therefore be more efficient/effective to place PV solar farms and wind parks in places with most sun and wind, and to transport the energy to places where the demand is high. The International Energy Agency (IEA) predicts renwable energy production costs of approximately half the price in Spain and northern Africa compared to northern Europe in 2030 [5]. To make use of this "cheap" renewable energy, an efficient method to transport this energy over large distances would be needed.

1.2 Metal energy carrier cycle

Figure 1.1 shows the energy density and specific energy of fossil fuels, commonly thought of renewable energy carriers (biofuels, ammonia, hydrogen and batteries), and various metal powders. It shows that metal powders show energy densities comparable to existing energy carriers (fossil fuels). This in combination with the fact that metals (such as Al and Fe) are abundant in the earth's crust, don't need to be
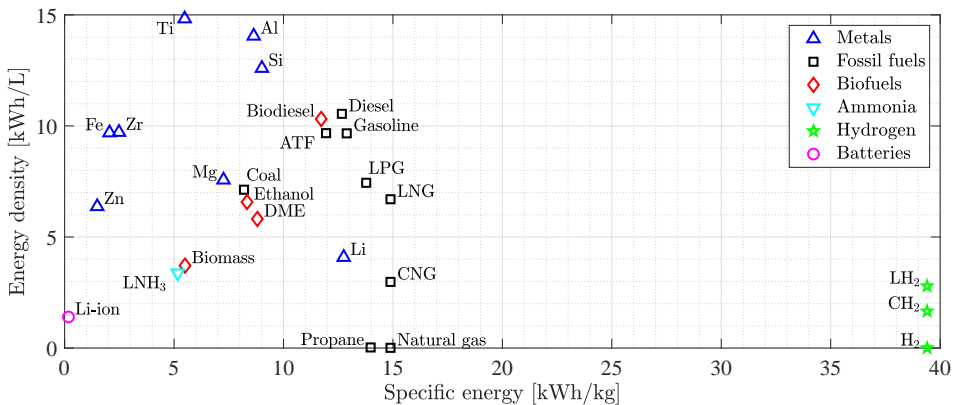
Figure 1.1: Energy by volume and mass for common dense energy carriers. Values for solid materials (metals, coal and biomass) are multiplied by 60% to estimate practical energy densities of powders/pellets. Values for metals from Fischer *et al.* [8]. Other abbreviations used: CH_2 = compressed hydrogen; LH_2 = liquified hydrogen; CNG = compressed natural gas; LNG = liquified natural gas; LPG = liquified propane gas; ATF = aviation turbine fuel; LNH_3 = liquified ammonia; DME = dimethyl ether.

stored under pressure or cryogenic conditions, and existing infrastructure for powder handling exists, gives the potential of using metals to transport and store renewable energy. The concept of using metal powder (specifically sponge iron) as energy carrier was first introduced by Mignard and Pritchard [6], and was later extended to multiple types of metals by Bergthorson *et al.* [7]. In the envisioned "metal energy carrier cycle", renewable energy is used to energize metal powder using a suitable reduction process at locations and times that renewable energy is available, this powder is then transported and/or stored, and is combusted (oxidized) to extract the energy.

This thesis focuses on the reduction process of iron-oxide powder for this energy carrier cycle due to the advantages iron has over other metals. Micron-sized iron powder is expected to burn heterogeneously (almost entirely in liquid state), forming similar micron-sized iron-oxide particles [7]. Furthermore, iron-oxide is readily available and ferrous powders make up nearly 50% of the worlds current metal powder production capacity [9]. Finally, industrial fossil-free iron-oxide reduction technologies, for the purpose of green steelmaking, currently already exist [10, 11]. In these processes iron ores are typically reduced using pure hydrogen, producing (sponge) direct reduced iron (DRI) and water vapor. This step transfers the energy from green hydrogen into the iron powder.

$$Fe_xO_y + y\ H_2 \rightarrow x\ Fe + y\ H_2O$$
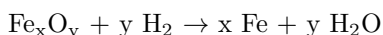
The subsequent combustion process, releasing heat, would follow:

$$x\ Fe + \tfrac{1}{2}\ y\ O_2 \rightarrow Fe_xO_y$$
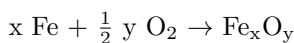
Although different industrial iron-oxide reduction technologies already exist, not all are equally suited for use in the metal energy carrier cycle.

1.3 Industrial processes for iron production

Over 90% of the global iron production occurs via a conventional blast furnace, in which coke (coal) is mixed with iron ore to produce molten iron [12]. The rest of the iron is produced using various smelting reduction methods (SRI), producing molten iron, and direct reduction (DRI) methods, producing sponge iron. Most of these processes rely on the use of (gasified) coal, natural gas or syngas (mixture of CO and H_2) as a reducing agent. An extensive overview of most existing SRI and DRI methods can be found in Battle *et al.* [13] and Schenk [14].

DRI methods are of most interest for the metal energy carrier cycle, since the production of molten iron (via blast furnace and SRI) would require a subsequent gas or water atomization step to (re-)produce combustible powder. As a second requirement, the reduction process should be able to be carried out using hydrogen alone. Table 1.1 shows an overview of existing DRI processes utilizing pure hydrogen. Out of these, the Circored process is most mature, with a 63 ton/h hot briquette iron plant in operation from 1999-2001 in Trinidad, producing a total of around 300.000 tons of hot briquette iron [10]. It was shut down do to a lack of natural gas supply (which was used for the hydrogen production). The Circored process employs a first stage high temperature circulating fluidized bed reactor in combination with a second stage lower temperature bubbling fluidized bed reactor. The other two hydrogen-only DRI processes, relying on shaft furnace reduction, are still in pilot test scale. Therefore, the use of a fluidized bed reactor seems most promising for use in the metal energy carrier cycle.

Reduction of iron ores/oxides using hydrogen has been researched extensively for green steelmaking. However, the kinetic results vary significantly between different ores and iron-oxides used as well as the experimental conditions [15, 16]. Therefore, no generic model exists and kinetic measurements are needed for new materials.

Similarly, sticking and sintering are common problems encountered in DRI-processes in general and specifically with the use of hydrogen [17, 18]. The sticking leads to agglomeration of powder, hindering granular solid flow in shaft furnaces and causing defluidization in fluidized beds.

Table 1.1: Hydrogen based DRI processes. Based on [11, 13, 14, 19].

Reactor type	Process	Iron ore size [mm]	Temperature [°C]
Shaft furnace	HYBRIT	~10	700-900
	HyFIT	0.02-0.06	1200-1550
Fluidized bed	Circored	0.1-2	850-900 (stage I)
			630-650 (stage II)

1.4 Goal and outline of the thesis

Although quite some knowledge exists on the reduction of iron ores, it is unclear to which extend it is applicable for the metal energy carrier cycle. Combusted iron powder is different from the iron ore typically used in the processes mentioned above. Furthermore, the particle size envisioned in the metal energy carrier cycle (< 0.1 mm) is challenging due to the influence of inter-particle forces. Finally, most existing direct reduction processes focus on steelmaking. Therefore, their product is typically melted down in an electric arc furnace. For the metal energy carrier cycle, the resulting iron powder should be combustible, meaning that properties such as retention of particle size are of importance. The objective of this research is therefore to study the reduction behavior of combusted iron powder using hydrogen.

This thesis is organized as follows. In Chapter 2 the methods and devices used to characterize the powder before and after experiments are briefly described and discusses. Subsequently, a brief summary on the metal combustion process and produced powder (feed-stock for this research) is given. Finally, the influence of impurities on the reduction process is discussed.

In Chapter 3, a study on the intrinsic reaction rate of iron oxide, produced by iron combustion, with hydrogen gas is presented. In this work, ~ 150 mg combusted powder is suspended in a relatively high flow rate of hydrogen and its weight change is accurately measured in time using a micro-balance. This is done for various temperatures and hydrogen concentrations. This weight change is then thoroughly analyzed and compared with analytical models to derive the limiting mechanisms of the reduction process. This chapter starts with a comprehensive overview of existing kinetic studies on iron oxide reduction.

In Chapter 4, the sintering of ~ 1 g combusted powder is investigated in non-reducing (nitrogen) and reducing (hydrogen) environments in a packed bed reactor. The produced pellets are compression tested to quantify the degree of sintering. A model is matched to the experimental findings and some predictions are made for when sintering occurs in metal energy carrier equipment.

In Chapter 5, a fluidized bed reactor is used to reduce ~ 750 g of combusted powder. The minimum fluidization velocity of the powder is studied in detail, since this parameter partially determines the efficiency of the reactor. Subsequently, reduction experiments in this fluidized bed reactor are presented and discussed.

Chapter 6 summarizes the work in this thesis. Recommendations are provided for further research/investigation on one side and for practical application on the energy carrier cycle on the other side.

2 Characterization

Abstract

Various measurement techniques are used in this research to analyze and characterize the iron(-oxide) powder before and after experiments. For proper interpretation of the results, it is important to understand the principles on which these techniques are based as well as their limitations. Secondly, it is crucial to also understand the iron combustion process, since this provides the starting material for the experiments carried out in this work. Lastly, the influence of impurities on both the reduction process as well as on the measurement techniques are briefly discussed. It should be noted that in the following chapters these effects are not investigated further due to the high purity iron(-oxide) used.

2.1 Measurement techniques

2.1.1 Scanning electron microscopy

A scanning electron microscope (SEM) is a device which produces images by scanning the surface of a sample with a focused beam of electrodes. The electrons interact with the atoms in surface layer of the sample and the produced signals give information about the surface structure and composition. Figure 2.1 shows an overview of the different types of signals produced. Secondary electrons (SE) reflect primarily the topology of the sample, since they can only escape from the top few nanometers of the sample. Back-scattered electrons (BSE) emerge from deeper in the sample and the signal strength is atomic number dependent. Energy-dispersive X-ray spectroscopy (EDS/EDX) can be used to measure the local (surface) elemental composition based on the characteristic X-rays emitted from the sample. However, determination of the exact iron-oxygen ratio is not possible due to the low atomic number of oxygen [21].
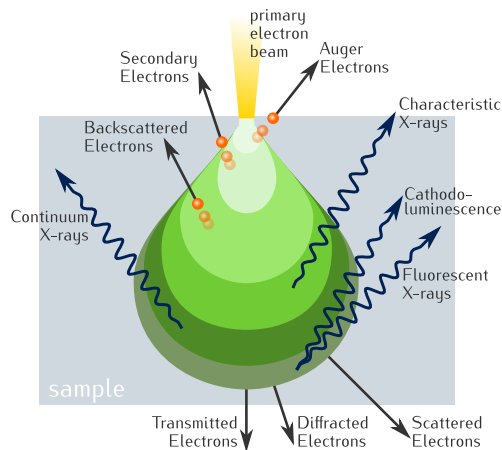

Figure 2.1: Signals produced during an electron beam - matter interaction [20].

For the SEM images in this dissertation, a FEI ESEM Quanta 600 FEG is used, using 30 kV of electron beam accelerating voltage and a spot size of 3.0 nm in high vacuum ($\leq 10^{-3}$ Pa). Typical images have a size of 2048-by-1768 pixels and per pixel accumulation times of either 3 or 10 μs. The working distance is set to 10 mm. Lens alignment and astigmatism correction are performed before each measurement session. Automatic brightness correction is used to obtain proper contrast. Images presented result from secondary electrons, unless stated otherwise. SEM imaging is deliberately not used for particle size analysis, due to the likelihood for sampling bias [22].

2.1.2 Particle size analysis

The particle size and shape distribution, i.e. the number of particles of different size and shape, is an important parameter, needed for proper interpretation of the powders behavior. Larger particles (with otherwise identical properties) typically have a smaller surface-to-volume ratio, leading to slower reaction behavior. Similarly, particles with the same volume, but a different shape, also have a different surface-to-volume ratio.

As shown by Whiting *et al.* [22], the choice of particle size measurement technique can have an effect on the distribution that is obtained. This is partly due to the amount of powder the different techniques require, but also inherently due to the way these techniques measure and define the particle size.

A Bettersizer S3 Plus is used in this work (unless stated otherwise) for the particle size analysis. It can perform both laser diffraction (LD) and dynamic image analysis (DIA) on the same sample. Prior to the measurement, the powder was dispersed in isopropyl alcohol (C_3H_8O). Ultrasound dispersion (50 W) was used during dispersion to break up any agglomerates, but was switched off (3 minutes waiting period) before measurements in order to prevent bubbles being produced.

A stirring speed of 1600 rpm is used for LD to prevent bubbles from interfering with the measurement. 5 subsequent measurements were performed on the same dispersed sample to reduce the influence of noise. The build-in Mie scattering analysis method is used to determine the particle size distribution.

The stirring speed is subsequently increased to 2500 rpm for DIA. A 10x magnification lens is used to take (backlight) images of the particles. Automatic bubble detection is used to remove (partially) transparent particles. Shape analysis is restricted to particles above at least 4 μm, since 1 pixel equals roughly 0.8 μm. A minimum of 3000 particles are acquired for each measurement. All particle sizes, measured using the dynamic image analysis method, are presented based on the area equivalent diameter $d_{p,i}$:

$$d_{p,i} = \sqrt{\frac{4 \cdot A_{i,measured}}{\pi}} \tag{2.1}$$

in which $A_{p,i,measured}$ is the measured 2D projected area of the particle. The circularity $C_{p,i}$ is subsequently defined as the perimeter of a circle with the same area equivalent diameter as the particle, divided by the actual perimeter $P_{p,i}$ of the particle:

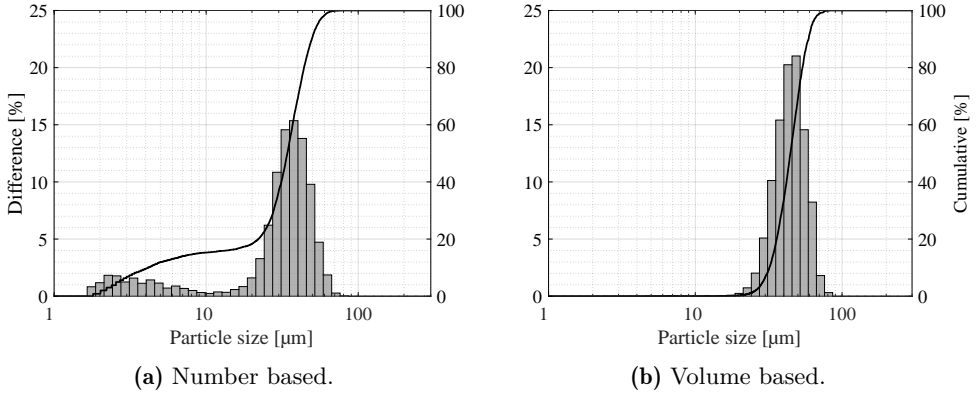$$C_{p,i} = \frac{\pi d_{p,i}}{P_{p,i}} \tag{2.2}$$

Figure 2.2: Different representations of the particle size distribution for the same powder, measured using DIA. Bars correspond to the left axis (fractions), while the solid lines correspond to the right axis (cumulative fraction).

The Sauter mean diameter is determined using the area equivalent diameter as:

$$d_{32} = \frac{\Sigma d_{\mathrm{p,i}}^3}{\Sigma d_{\mathrm{p,i}}^2} \tag{2.3}$$

All distributions in this dissertation are based on apparent volume, i.e. the fraction of the total volume that is occupied by a given particle size range. This is done since: (1) the laser diffraction method inherently measures the volume distribution and (3) the volume based distributions typically closely resemble the mass based distribution, which is most interesting from the point of the metal energy carrier cycle. Figure 2.2 shows an example of a number and volume based particle size distribution, where we can see that small particles hardly contribute to the total volume of the powder.

2.1.3 Sieving method

Several methods exist to separate particles based on their size (and shape) [23]. The method used in this research is that of dry vibratory sieving using mesh test sieves.

A RETSCH AS 200 basic vibratory sieve shaker in combination with one RETCH (32 µm aperture) and two LINKER (100 and 150 µm aperture) woven wire mesh sieves (all 100 mm in diameter) are used to filter out agglomerates and fines for use in the fluidized bed reactor in Chapter 5. The sieving time is set to 99 minutes per batch, with the amplitude set to maximum. For the research described in Chapters 3 and 4, no sieving is performed.

2.1.4 Density analysis

Several densities can be defined, when dealing with powders, dependent on the definition of the occupied volume and the packing arrangement of the particles. In the

Table 2.1: Packing densities and void fractions of mono-dispersed solid spheres [24].

Packing type	Example	Void fraction ε	Packing density
Thinnest regular	Cubic lattice	0.4764	0.5236
Very loose random	Spheres slowly settled	0.44	0.56
Loose random	Spheres dropped into bed	$0.40 - 0.41$	$0.59 - 0.60$
Poured random	Spheres poured into bed	$0.375 - 0.391$	$0.609 - 0.625$
Close random	Spheres in vibrated bed	$0.359 - 0.375$	$0.625 - 0.641$
Densest regular	FCC or HCP lattice	0.2595	0.7405

case of solid spheres of equal radius (mono-disperse), estimations for the void fraction ε and packing density are given in Table 2.1 [24]. Although these values are for mono-disperse spherical particles, which might not be fully representative for non-spherical and/or poly-disperse particles, they are used in this work to estimate densities.

If the void fraction is known, the bulk (packing) density ρ_b correlates to the particle density ρ_p by:

$$\rho_b = (1 - \varepsilon) \cdot \rho_p \tag{2.4}$$

where ε is the (inter-particle) bed voidage.

Secondly, in the case of porous/hollow particles, we can define an internal particle void fraction ε_p and correlate the particle density to the solid density ρ_s by:

$$\rho_p = (1 - \varepsilon_p) \cdot \rho_s \tag{2.5}$$

in which ρ_s is the volume occupied by the solid phase material (i.e. iron and iron-oxides). ε_p can furthermore be subdivided in a closed porosity (fully encapsulated by the solid material) and an open porosity (connected to the outside).

To determine the bulk density of the powders, A 100 mL measuring cylinder (Hirschmann Laborgeräte, DURAN glass) is used in combination with a weighing scale (Mettler Toledo PG5002-S). The powder is poured into the cylinder and subsequently vibrated to obtain close random packing. 5 measurements are averaged.

The solid density is estimated from the powder composition, in combination with the theoretical densities of the individual phases. To estimate the closed porosity, pycnometer measurements (AccuPyc II 1340 V3.00) are performed, which measures the solid density including closed pores.

2.1.5 X-ray diffraction

Iron and its oxides are crystalline, meaning that the atoms are ordered in well defined repetitive crystal structures. When illuminating these materials with a beam of X-ray light, the beam will be diffracted, producing a measurable pattern of high intensity peaks. The located (angle) of these peaks is the result of constructive and destructive interference resulting from the crystal structure of the material. The produced interference pattern is therefore a "fingerprint" of the atoms present the material in combination with their orientation to each other. If a material is composed of a mixture

(a) Iron powder.
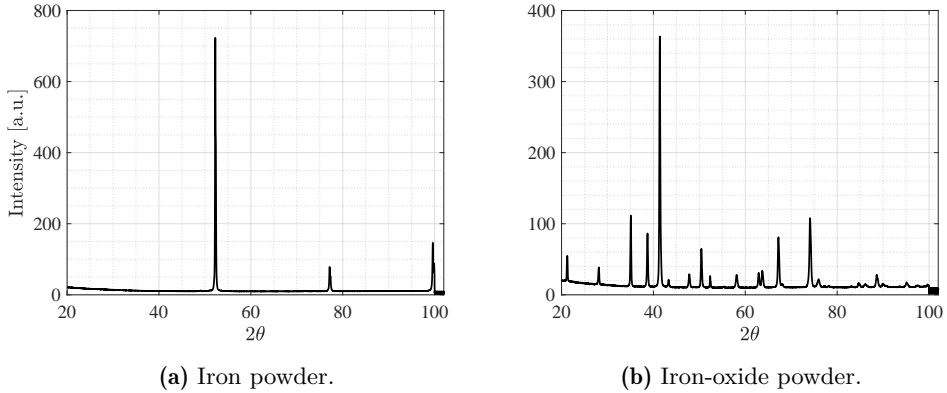
(b) Iron-oxide powder.

Figure 2.3: X-ray diffraction patterns of iron and iron-oxide powder.

of crystalline materials, the measured pattern is a linear combination of the individual components (multiplied by their mass fraction and inherent diffraction strength). On this principle X-ray diffraction is based. For a full description of the method and the ways to obtain quantitative results, the reader is referred to Bish *et al.* [25].

For this dissertation, a Bruker D2 PHASER with LYNXEYE XE-T detector is used (unless stated otherwise) to perform X-ray diffraction. A cobalt target is used instead of copper, due to limited X-ray penetration depth of copper X-rays in iron-containing samples [26]. An accelerating voltage of 30 kV in combination with a 10 mA current is used to produce the X-rays. Each scan (coupled $2\theta/\theta$ mode) measured the diffracted signal between 20 and 102° of 2θ, in steps of 0.024°, with a measurement time of 2 s per step. The total time for one scan is therefore around 2 hours. The samples are continuously rotated at 10 rotations per minute during each scan, in order to avoid effects of preffered orientation. Example patterns of both iron and iron-oxide (mixture of magnetite and hematite) can be seen in Figure 2.3. Analysis is carried out using the DiffracEva software equipped with the Crystallography Open Database. Semi-quantitative peak fitting is used to determine the composition applying a first order approximation for the background signal.

2.1.6 X-ray computed tomography

X-rays are only partially absorbed and/or reflected by a material. The amount that passes through the material is dependent on the density of the material, the type of atoms that make up the material, and the wavelength of the X-rays. In general, atoms with a higher atomic number and materials with a higher density absorb and reflect/diffract more X-rays. X-ray computed tomography employs this principle by sending a beam of X-rays through a material and measuring a 2D image of the transmitted light. By systematic rotation the sample and measuring the transmitted light, a (virtual) 3D model can be mathematically reconstructed. A visual representation of the method can be seen in Figure 2.4. This virtual 3D model can then show the external as well as internal structure of the scanned object.
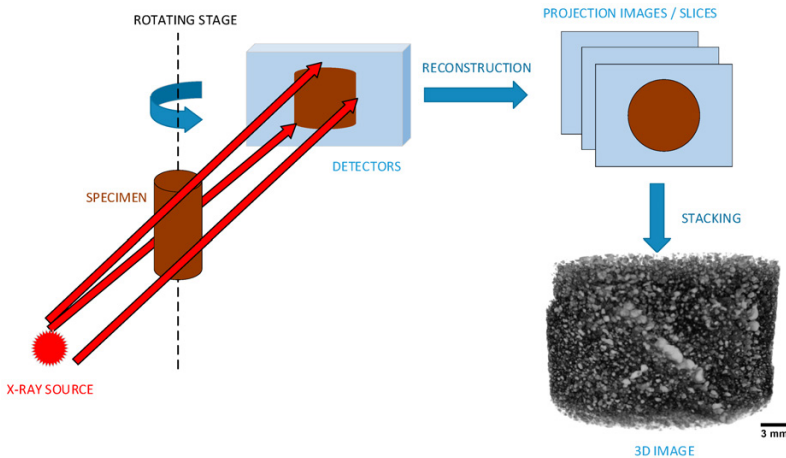
Figure 2.4: Schematic representation of μCT. Adapted from Guntoro *et al.* [27].

The sample holder used in this work (see Figure 2.5) is based on the design of du Plessis *et al.* [28]. A plastic cylinder (3 mm diameter, 5 mm height) is inserted on top of a 100 mm length glass tube (3 mm outer diameter, 1.6 mm inner diameter). A 0.7 mm diameter, 1 mm hole is subsequently drilled into the plastic. The resulting powder container volume is around 0.11 mm^3 (applying a 118° drill tip angle).

A General Electric / Phoenix Nanotom 160 NG is for the μCT-measurements. A 0.1 mm copper filter is used to reduce beam hardening effects. 1400 images were taken distributed over a full 360° rotation. An accelerating voltage of 90 kV is used in combination with a current of 170 mA. The resulting voxel size is 1.33 μm.

VG Studio MAX 2.2.3 is used for the virtual reconstruction. A Gaussian blur filter (3 voxel standard deviation) is used to reduce the amount of noise. The defect detection module, applying the VGDefX (v2.2) algorithm, is used to determine the closed porosity. Surface sealing is enabled to reduce particle surface noise artifacts. The volume analyzer module is used to determine the total volume of the solid material.

Figure 2.5: Powder holder for μCT measurements. The bottom section is made of glass, while the top part is made out of plastic.

2.2 Microstructure of combusted iron

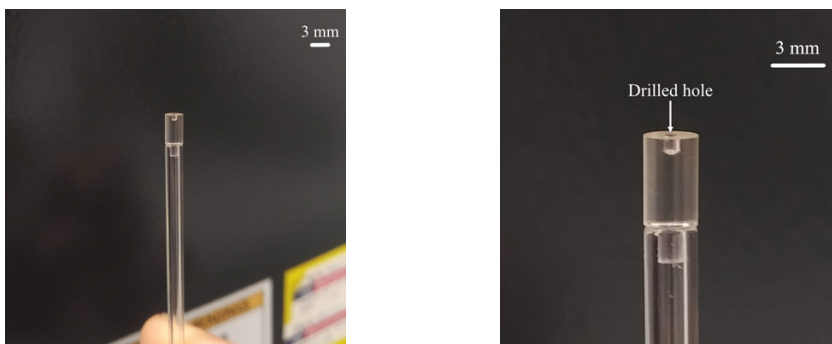Although the metal energy carrier concept is relatively new, quite some research has been performed on the combustion of iron particles. For a general overview, the reader is referred to the work of Goroshin *et al.* [29]. Most experimental research can be divided in single particle studies [30–35], small burners [36–40] and stagnant aerosols [41–43]. The numerical research can similarly be divided in single particle studies [44–47] and "flame" propagation models [48, 49]. The combustion process can typically be divided in four parts: (1) ignition in the solid-state leading to a thermal run-away and subsequent melting of the iron particle (2) combustion of the liquid iron-oxide droplet, (3) solidification to magnetite (Fe_3O_4), and (4) subsequent solid state oxidation to hematite (Fe_2O_3), assuming enough oxygen in the gas phase during the combustion process.

The ignition characteristics of iron powder (occurring in the solid state) have been studied by Mi *et al.* [50]. The underlying mechanism occurs in 5 steps: (1) diffusion of oxygen to the particle surface and subsequent absorbed onto the iron particles surface, (2) oxygen anions are incorporated into the surface oxide lattice, (3) iron cations diffuse from the metal (or lower oxide) phase deeper in the particle into the (higher) oxide phase closer to the surface, (4) diffusion of oxygen and iron ions through the oxide layers, (5) reactions at the iron/oxide interfaces. Due to the fact that iron cations have a higher diffusivity then the oxygen anions, the process is mainly dominated by outward diffusion of iron cations. The mechanism indicates that a larger surface area results in a faster ignition process and therefore possibly a thermal run-away at lower temperatures (i.e., a lower auto-ignition temperature).

After thermal run-away occurs, the particle quickly melts and the adsorption and internal diffusion in the liquid phase greatly increase. The process becomes dominated/controlled by external diffusion and convection of the oxygen towards the particle surface [49]. An initial rapid oxidation (first stage) up to one-to-one iron-oxygen molar ratio in the droplet is subsequently followed by a slower second stage oxidation. This second stage is most likely dominated by internal diffusion of oxygen in the iron-oxide melt [30]. When the oxidation has sufficiently slowed down, the particle starts to cool-down to below the melting temperature of magnetite, after which solidification occurs. A phase diagram of the iron-oxygen system can be seen in Figure 2.6.

Results from iron rod combustion indicate that the iron-oxide melt might contain more oxygen (and even nitrogen) then is required for formation of stoichiometric hematite (Fe_2O_3) [51]. Furthermore, hematite is unstable at these high temperatures. Therefore, the iron-oxide melt will solidify to magnetite ($T_{melt} = 1582$ °C) and the excess oxygen is expelled into the gas-phase (forming O_2). The production of this gaseous oxygen is thought to be one of the causes of the typically observed micro-explosions, resulting hollow shells, and particles with internal closed pores [21, 31–33, 52]. Other causes are evaporation of iron (similar to the process described by Wainwright *et al.* [53] for combustion of Al:Zr composite powders) and shrinkage cavities, similar to those observed in metal casting [54]. Figure 2.7a shows an example of the dendritic/lobe-shaped structure of the internal closed void after solidification. Similar shapes were observed from the μCT-scan (Figure 2.10).
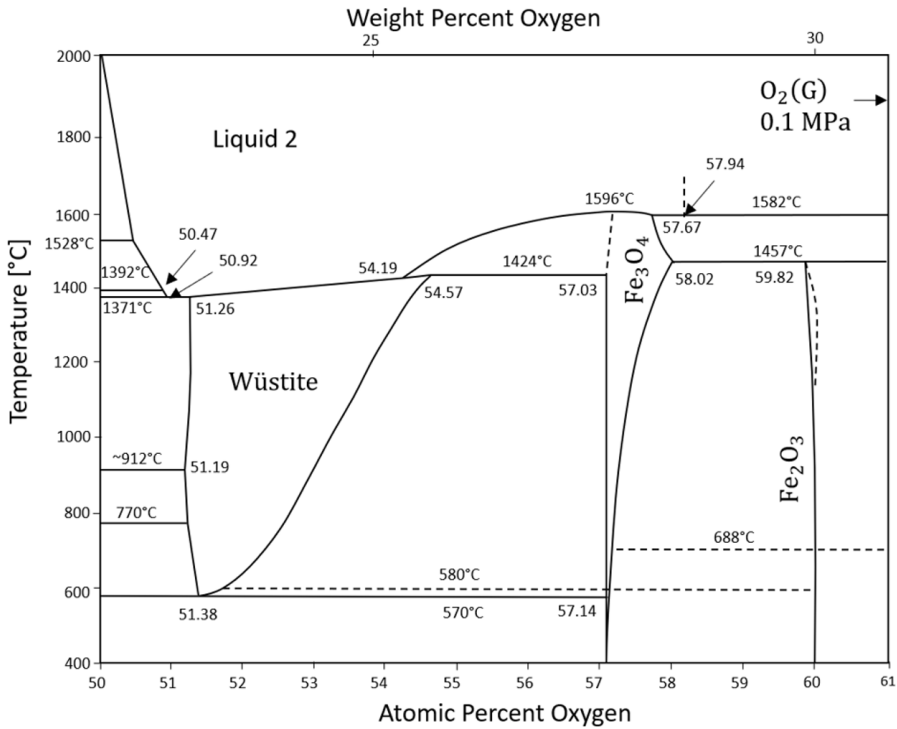
Figure 2.6: Phase diagram of the Fe-O system. Adapted from Choisez *et al.* [21].

After further cooling, the hematite phase becomes stable ($T \leq 1457$ °C) and solid state oxidation from magnetite to hematite occurs, provided sufficient temperature and oxygen. Zheng *et al.* [55, 56] found that this oxidation first occurs at the surface, producing a hematite shell with plate-like structures. These plates can also be seen in Figure 2.7a, where the particle is covered in many crystal grains, with visible grain boundaries separating them. These crystals also seem to have preferred orientation, indicated by the parallel aligned grain boundaries. After the surface is fully oxidized, hematite plates grows inwards along existing magnetite grain boundaries as well as along preferred crystalline orientations in the magnetite matrix. Choisez *et al.* [21] showed the presence of these internal hematite plates in combusted iron using electron backscatter diffraction (EBSD) on cross-sections of combusted powder (Figure 2.8).

Since the conversion to hematite can only occur in the solid-state, the temperature and oxygen concentration during the cooling down period of the powder will determine the amount of hematite formed. Single particle experiments and small burners (where the burning particles are exposed directly to room temperature) will therefore predominantly produce magnetite particles (as in [37]), while drop tube experiments and larger burners with incorporated cyclones will lead to more hematite being formed (as in [21, 57]). This is of great importance for the reduction process, since it is known that mixtures of magnetite and hematite reduce faster then either pure magnetite or hematite due to the formation of crystalline defects during reduction, acting as nucleation sites and promoting solid-state diffusion of iron atoms [58, 59].
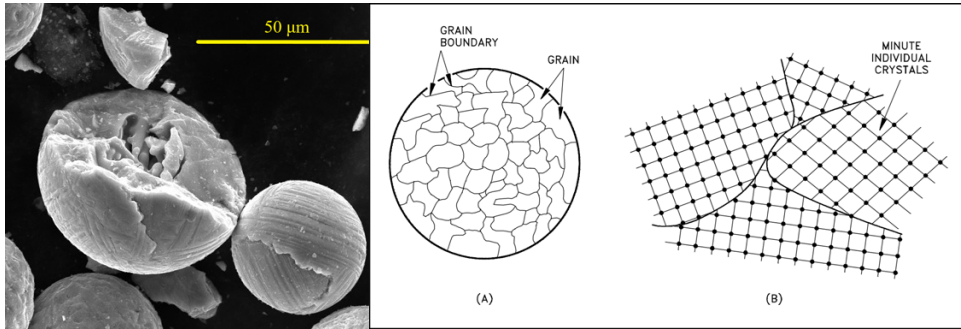
(a) Crushed powder **(b)** Graphical representation of crystal structure [60]

Figure 2.7: Scanning electron images of combusted powder and graphical representation of the underlying atomic structure of the particle. The lines on surface of the particles correspond to grain boundaries between crystals.

Furthermore, grain boundaries are known to be the prime locations where reactions take place due to their inherent meta-stable atom positions [61]. It is also well-known that the average grain size, and therefore the amount of grain boundaries, is influenced by the cooling rate of the material (faster cooling typically leads to smaller grains). This means that powder which is quenched after combustion might reduce faster.

Finally, cracks are commonly found in combusted iron particles. It is however found that these cracks propagate through existing hematite crystals, indicating that they form after the combustion process is (almost) complete [21]. The cracks are therefore most likely caused by particle collisions during the capturing or from the handling and preparation of the samples for SEM measurements.

Figure 2.9 shows a 3D reconstruction and a top-view cross-section of combusted iron
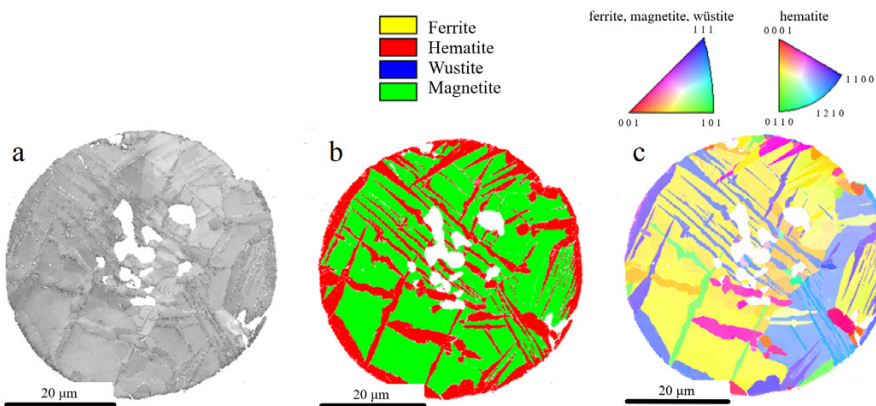

Figure 2.8: EBSD result of a cross-section from a combusted iron particle showing the hematite plates (a) image quality map, (b) phase map, and (c) crystal orientation map. Adapted from Choisez *et al.* [21].

powder ($\approx$ 0.33 mg), measured using µCT scanning. From the cross-section it can be observed that nearly all particles contain internal voids after combustion. Some bright particles can also be observed, most likely consisting of ferrite (Fe). The total solid volume was estimated to be around 0.063 mm^3. The ferrite particles accounted for around 1.4 vol% of this solid volume. Assuming a poured random packing fraction ($\varepsilon = 0.39$), the internal porosity of the powder ε_p is estimated to be 9.6 %. This internal porosity can furthermore be split into a closed fraction ($\approx$ 0.6%) and an open fraction ($\approx$ 9%). These porosities match well with results obtained using a measuring cylinder, in combination with pycnometer and X-ray diffraction measurements.

Figure 2.10 shows a reconstruction of a single particle, containing a closed internal void. A cutting plane is used to virtually remove the top half of the particle. A dendritic pore structure can be observed, similar to that in Figure 2.7a. The internal void can be estimated to occupy around 6.63% of the particle's volume.
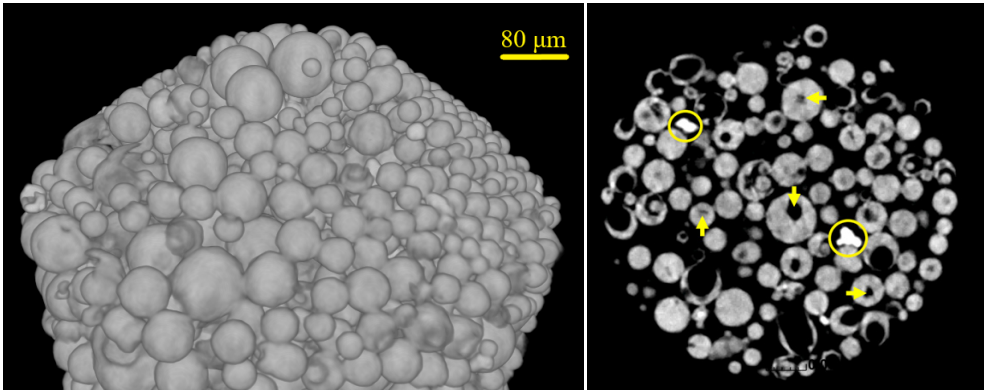
Figure 2.9: 3D reconstruction (left) and a top-view cross-section (right) of combusted iron powder. The circles in the cross-section mark bright particles, which most consist of iron (ferrite), while the arrows indicate some internal voids.

(a) Single particle   **(b)** Solid phase   **(c)** Internal void
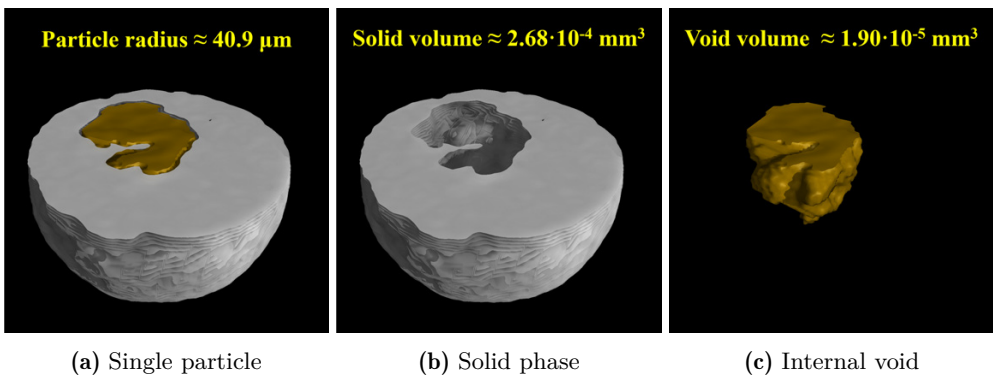
Figure 2.10: 3D reconstruction of a single particle containing a closed internal void. A cutting plane is used to make the top half of the particle transparent. The void is colored orange, while the solid material is colored gray.

2.3 Influence of impurities

The previous section, describes the typical combustion of high purity iron particles (> 99 wt% Fe). However, during the analysis of the powders used and produced in upcoming chapters, peculiar particles were occasionally observed during SEM measurement. Some examples are presented in Figure 2.11. The odd morphology of the particles is most likely the result of high local concentrations of impurities.

Although the high iron combustion temperature ($T_{\text{adiabatic}} = 1956\,^{\circ}\text{C}$) results in evaporation of many species, Choisez *et al.* [21] did find impurities being preserved in the powder during the combustion process. The results indicated that carbon and sulfur largely evaporate (and most likely oxidize) during combustion, while concentrations of nickel and copper stay nearly constant. Species like manganese, molybdenum and chromium only slightly decrease during combustion. The preserved components might affect the subsequent reduction process.

Shao *et al.* [62] found that the reduction of magnetite particles can be improved by coating the particles with magnesium-oxide MgO. The main reason is the reduced sticking tendency of the particles and therefore extended fluidization and reduction time. Similarly effect are found for CaO, SiO_2, NiO, and Al_3O_3 [14, 17, 18, 63]. In chemical looping combustion, Fe-Ti materials are often used, since (1) they show higher reactivity and stability then hematite and (2) ilmenite ($FeTiO_3$) is a naturally occuring mineral and therefore relatively easy to obtain [64].

Most studies, however, mention impurity concentrations exceeding > 1 wt%, while in this work the concentration is typically in the order of $0.1 - 1$ wt%. In the following chapters the effect of these impurities on the kinetic, sintering and fluidization measurements are therefore assumed negligible.
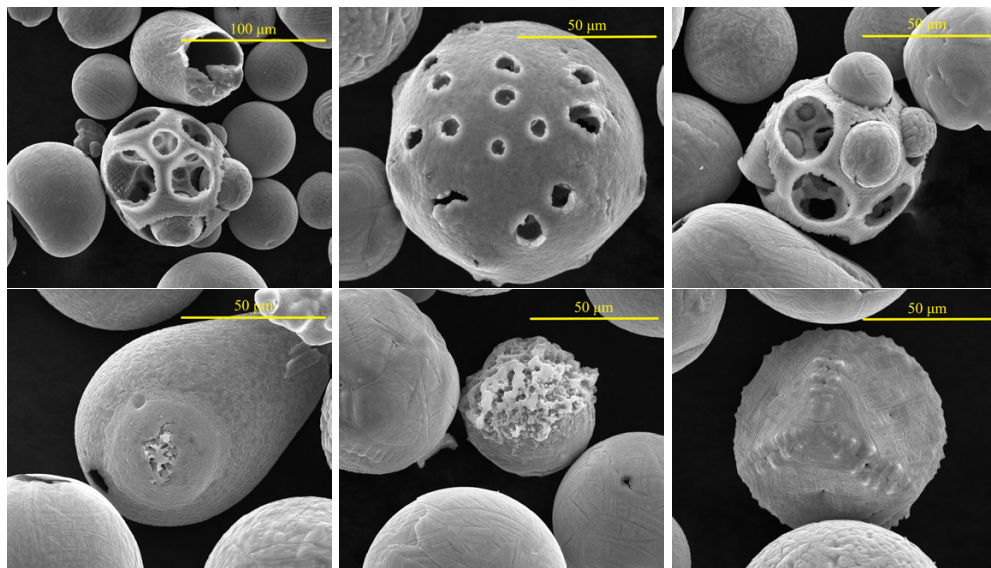

Figure 2.11: SEM images of peculiar "combusted iron" particles.

3 Kinetics

Background image: scanning electron microscope image of iron particles regenerated (reduced) with hydrogen at 700 °C.

Abstract

Hydrogen reduction of iron oxide fines, produced by iron combustion, were investigated using thermogravimetric analysis (TGA). Isothermal reduction experiments were conducted at a temperature range of 400-900 °C and at hydrogen concentrations of 25-100 vol%. Scanning electron microscopy (SEM) showed that the morphology of the reduction products depends on the reduction temperature but not on the hydrogen concentration. Reduction at higher temperatures lead to larger pore sizes. Based on an extended Hancock-Sharp "lnln"-method the appropriate gas-solid reaction models are determined, suggesting that the reduction can be described by a single-step phase boundary controlled reaction at temperatures below 600 °C, whereas a multistep mechanism is required for the description of reactions at higher temperatures.

3.1 Introduction

Many experimental studies have been reported to investigate the reaction mechanism and kinetics of direct iron reduction by hydrogen. Some representative references are listed and compared in Table 3.1. The majority of these studies were based on naturally found iron ores. Wei *et al.* [65], for instance, used limonite ore obtained from Taiyuan Heavy Industry CO., Ltd. (China). They found that the reduction of hematite ore (Fe_2O_3) to metallic iron (Fe) in their rotary drum reactor was controlled by one-dimensional formation and growth of nuclei below 850 °C, while at 900 °C the reaction was mixed controlled with diffusion limiting the reaction in the final stages of the reduction. They found that the activation energy of the reduction process (described by a single step reaction) was 51 kJ/mol. Elzohiery *et al.* [66] used taconite ore fines (20-53 μm) of the Mesabi range (U.S.) in their high temperature (1150-1350 °C) drop tube reduction experiments. They found that they could reduce their samples within several seconds and the conversion rate could best be described by one dimensional nucleation and growth with an activation energy of 193 kJ/mol. They also found that reduction had a first-order dependency on the hydrogen concentration. In their case, the effect of particle size was found to be negligible within their studied range. Similar type of experiments (high temperature drop tube) were also performed by Qu *et al.* [67] but using a different type of ore (with a similar particle size). They found that their experimental results could best be described by a 3D phase boundary reaction (shrinking core model). The apparent activation energy of this reaction was 270 kJ/mol in the temperature range 1277-1477 °C. Kuila *et al.* [68] used Indian magnetite ore from Pokphur in the Kiphere district of Nagaland. Their experiments showed that the reduction of these fines (75-180 μm) between 700-1000 °C took place in two stages. The magnetite is first reduced to wüstite and afterwards the wüstite is further reduced to metallic iron. The activation energies of the two stages were found to be 42 and 55 kJ/mol, respectively. Spreitzer and Schenk [69] performed reduction experiments on four different kinds of ores in the temperature range 600-800 °C. They used a combination of three parallel nucleation and growth models, which were able to describe all four different ores. However, the calculated apparent activation energies varied in the range 15-60 kJ/mol depending on both the type of ore and the degree

of reduction. Piotrowski *et al.* [70] reduced fine (91 µm mean diameter) hematite powder (PEA Ridge Iron Ore Co.) to wüstite in the range of 700-900 °C. They found that the reduction could best be described by a nucleation and growth model for the initial stage of the reduction, which later switched to a 1D diffusion model. The nucleation and growth model had an apparent activation energy of 58 kJ/mol. Morales-Estrella *et al.* [71] used magnetite concentrated ore from the Mesabi Range (U.S.) and performed reduction experiments using hydrogen in the temperature range of 400-900 °C. They studied both standard and activated (milled) powder. They found that sintering occured above 700 °C and therefore they only derived kinetic parameters for the temperature range of 400-500 °C. They found that the milled powder (which had a smaller mean particle size) had a higher conversion rate. Their data could be best fitted by a nucleation and growth model with an exponent of 2.5. They concluded that lattice strain due to the milling had an effect on the apparent activation energy, which was 70 kJ/mol for the as-received powder and 65 kJ/mol for the milled powder.

Natural iron ores possess large variation in size, composition and impurities, giving a partial cause to the spread in the kinetic parameters obtained in above-mentioned studies. In contrast, some studies have been performed for (synthetic) iron oxides with high purity. Pineau *et al.* [72, 73] did research on low temperature reduction of hematite and magnetite reduction using high purity oxides (>99.8 wt% Fe). They found magnetite reduction occurred via 1D nucleation and growth or phase boundary reaction at temperatures below 650 °C, while diffusion was limiting for higher temperatures (measurements where performed up to 950 °C). Hematite to iron reduction was found to be best described by a nucleation and growth model below 420 °C, while it is controlled by the phase boundary reaction at higher temperatures (up to 680 °C). Pourghahramani and Forssberg [74] used high purity hematite concentrate and found that the reaction occurs in a two step process (from hematite to magnetite to iron). They analyzed the reduction using a model free method in the temperature range 350-750 °C. The determined apparent activation energy showed a strong dependence on the extent of conversion, indicating a mixed control regime. Lin *et al.* [75] prepared their hematite sample by precipitating a $Fe(NO_3)_2 \cdot 9H_2O$ solution from Fisher Chemical Corporation. They found that the reduction behaviour could best be described by a two step mechanism. The hematite to magnetite reduction matched best with a uni-molecular model (E_a=89.13 kJ/mol), while the magnetite to metallic iron matched best with a 2D nucleation model (E_a=70.412 kJ/mol). The size of the powder used in [72, 73] is around 1-2 µm, and was unfortunately not reported in [74, 75].

As shown in these studies, even for high purity iron oxides, the reduction kinetics varies significantly due to the influence of macro-structure (particle size, porosity) and micro-structure (crystalline size, vacancies, impurities), and the experimental conditions (temperature, methods), as being pointed out by many peers [15, 16, 73, 76]. Due to this large spread of results in literature, there currently exists no generic kinetic model nor fixed parameters for iron oxide reduction. New types of materials therefore require their own kinetic measurement and analysis. The iron oxide powder for the application of metal fuel has unique characteristics, e.g., composition, size, surface morphology etc., for which, to the authors' knowledge, no study has been reported yet in literature.

Table 3.1: Summary of kinetic studies on iron oxide reduction by hydrogen in litera-
ture. RD = rotary drum reactor, DT = drop tube reactor, FB = fluidized
bed reactor, and TGA = thermogravimetric analyzer

	Source Material	Size (μm)	Reaction step	T (°C)	Model	E_a (kJ/mol^{-1})	Reactor
[65]	Limonite ore	44-89	$Fe_2O_3 \rightarrow Fe$	700-900	1D nucleation and growth + diffusion of oxygen in the dense iron layer	51	RD
[66]	Taconite ore	20-53	$Fe_3O_4 \rightarrow Fe$	1300-1550	1D nucleation and growth	193	DT
[67]	Hematite ore	45-125	$Fe_2O_3 \rightarrow Fe$	1375-1475	Diffusion of Fe^{3+}-ions in the liquid product layer	156	DT
[68]	Magnetite ore (Pokphur)	75-180	$Fe_3O_4 \rightarrow Fe$	700-1000	Pore diffusion kinetics	42 & 55	TGA
[69]	Hematite & limonite ore	250-500	$Fe_2O_3 \rightarrow Fe$	600-800	Nucleation and growth model	15-60	FB
[70]	Hematite ore (PEA Ridge Iron Ore Co.)	91	$Fe_2O_3 \rightarrow FeO$	700-900	Nucleation and growth + diffusion controlled	58.13	TGA
[71]	Magnetite ore (Mesabi Range, USA)	4-40	$Fe_3O_4 \rightarrow Fe$	400-900	Nucleation and growth	65-70	TGA
[72]	Hematite powder (Merck)	1-2	$Fe_2O_3 \rightarrow Fe_3O_4$	220-680	Nucleation and growth + phase boundary reaction	76	TGA
[72]	Hematite powder (Merck)	1-2	$Fe_3O_4 \rightarrow Fe$	220-680	Nucleation and growth + phase boundary reaction	39-88	TGA
[73]	Magnetite powder	1-2	$Fe_3O_4 \rightarrow Fe$	210-950	Diffusion	44-200	TGA
[74]	Hematite concentrate (LKAB)	-	$Fe_2O_3 \rightarrow Fe$	350-750	-	70-166	TGA
[75]	Hematite concentrate	-	$Fe_2O_3 \rightarrow Fe_3O_4$	21-900	1D nucleation and growth	89	TGA
[75]	Hematite concentrate	-	$Fe_3O_4 \rightarrow Fe$	21-900	Nucleation and growth	70	TGA

This work therefore aims to derive the reduction kinetics of iron oxides using hydrogen
with respect to this aforementioned metal fuel application. The iron oxides studied
are direct products of iron combustion. The conversion rate of the powders is studied
using isothermal thermogravimetric experiments at temperatures between 400-900 °C
and hydrogen concentrations of 25-100 vol%. The weight loss of the powder is recorded
and converted into a conversion rate. Based on an extended Hancock-Sharp "lnln"-
method [77] the appropriate gas-solid reaction models are determined, which are then
fitted to the experimental data to obtain the kinetic parameters.

This chapter is organized as follows: First, the materials and methods used are de-
scribed, after which the kinetic analysis strategy is explained. Subsequently, the
experimental results are given, followed by the kinetic analysis of these results and
conclusions of the presented work.

3.2 Materials and methods

3.2.1 Materials

The iron oxide powder used in this study is produced by combustion of high purity
(99 wt% Fe) iron powder from CNPC Powder (CNPC-FE400) in a cyclonic burner
developed by T. Spee during his master's graduation project [78]. The exact combus-
tion process is still a topic of active research [30–33, 36–40, 42, 43, 45, 49, 57], but
the general idea is that during the combustion process the iron powder melts and the
molten iron droplets react with oxygen. They solidify in the burner exhaust and are
captured using a cyclone. As a result, the iron oxide powder consists of predominantly
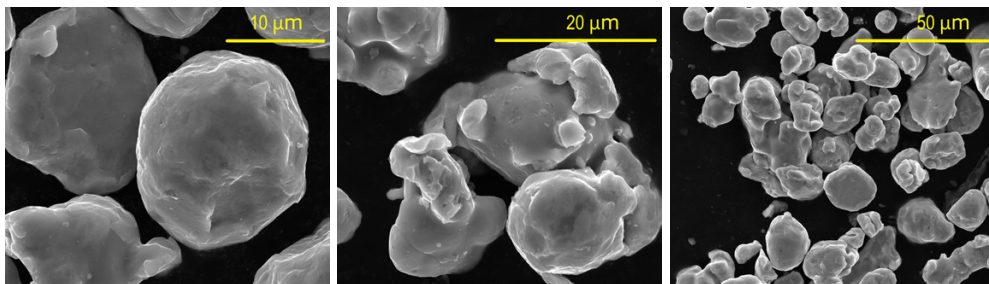
Figure 3.1: SEM images of the high purity iron powder before the combustion process.
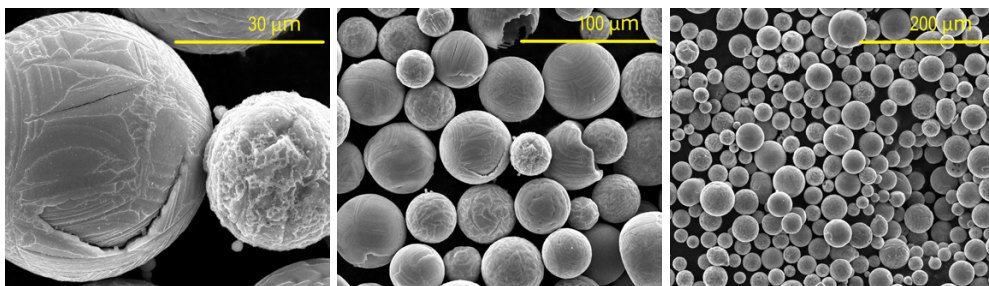
Figure 3.2: SEM images of the iron oxide powder after the combustion process.

spherical particles. SEM images (made with a FEI Quanta 600) of the powder before and after combustion can be seen in Figures 3.1 and 3.2, respectively. The particle size distribution of the combusted powder, determined using the laser diffraction method (Malvern Mastersizer 2000), is given in Figure 3.3. The specific surface area, estimated from this particle size analysis, is 330 m^2/kg. The bulk density was estimated using a measuring cylinder to be 3287 kg/m^3, resulting in a particle density of 5193 kg/m^3, assuming close random packing.

X-ray powder diffraction showed that the oxide powder consisted of about 40 wt.% hematite (Fe_2O_3), 58 wt.% magnetite (Fe_3O_4). The other 2 wt.% is made up of traces of wüstite (FeO) and iron (Fe). Due to the high purity of iron powder used in the combustion process (99 wt.% Fe), no other minerals are present in noticeable amount.

3.2.2 Thermogravimetric analyzer

TGA measurements are conducted using a thermogravimetric analyzer as seen in Figure 3.4. The setup was initially developed in the work of Coenen *et al.* [79]. It consists of an aluminum-oxide crucible (5 mm inner diameter, 10 mm height and 1 mm wall thickness), suspended within a quartz tube, which in turn is surrounded by electric heating elements. The quartz tube is on the top connected to a micro-balance (CI-Precision MK2-5M) with a sensitivity of 0.1 μg, from which the crucible is suspended using a titanium wire. A flow of nitrogen is supplied from the balance side, to prevent reactive gases from entering the balance. On the bottom side of the quartz tube, a
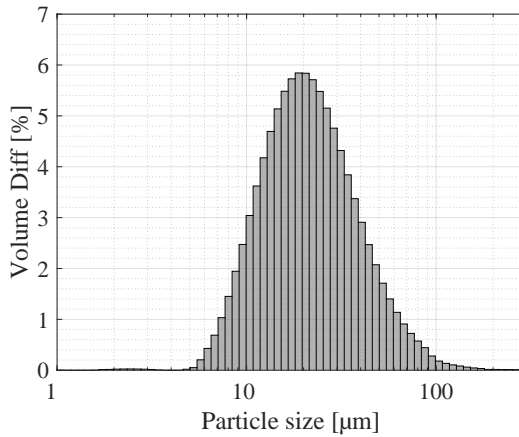
Figure 3.3: Particle size distribution (volume based) of combusted iron powder used in this research.
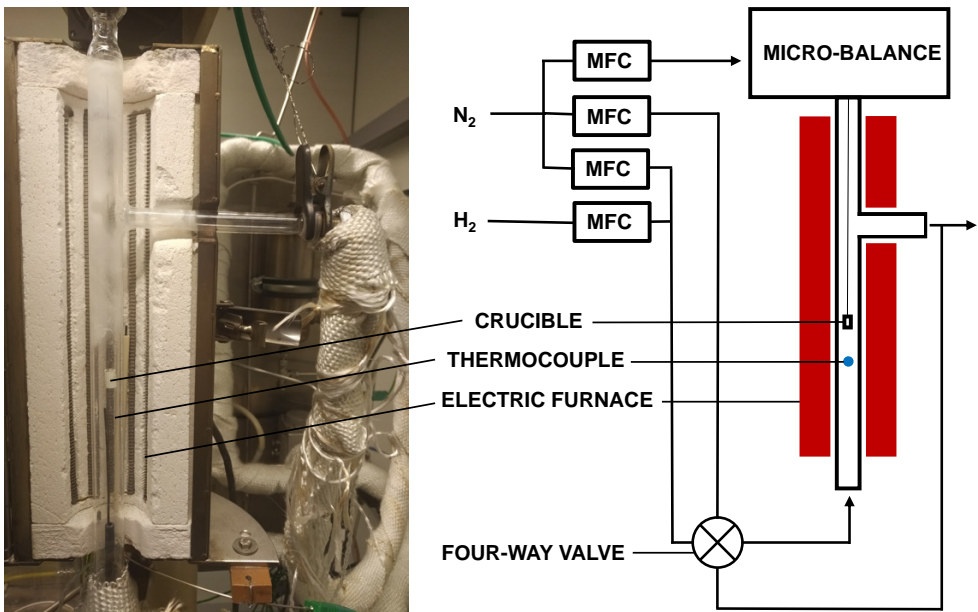

Figure 3.4: Schematic diagram of the thermogravimetric analyzer [79].

mixture of reducing and non-reducing gases can be supplied. All mass flows are controlled by Bronkhorst mass flow controllers (MFC). A thermocouple (type K) is placed just below the crucible, to measure the local temperature and to control the heating elements.

3.2.3 Experimental procedure

A cyclic reduction-oxidation (redox) experiment is carried out to investigate the cyclic behavior of combusted iron powder. More information on this experiment can be found in Appendix A.1. The results indicate that degradation of the powder occurs over multiple (redox) cycle. Therefore, individual isothermal reduction experiments are carried out to determine the reduction kinetics.

During each experiment the crucible, filled with around 150 milligram of iron oxide powder, is placed in the setup and is heated at a controlled rate of 20 °C per minute. During heat-up, nitrogen is supplied, with a flow rate of 0.5 NLPM (reference conditions: 0 °C and 1 atm) to prevent the powder from further oxidizing. When the required temperature is reached, the flow is switched to a set mixture of hydrogen and nitrogen. The mass flow rates during these experiments, where: 0.48 NLPM H_2 and 0 nl/min N_2 for the 100 vol% H_2 experiments, 0.4 NLPM H_2 and 0.4 NLPM N_2 for the 50 vol% H_2 experiments, and 0.15 NLPM H_2 and 0.45 NLPM N_2 for the 25 vol% H_2 experiments. After the set reduction time is reached, the powder is cooled down (also 20 °C/min), again in a nitrogen environment (0.5 NLPM). During the entire process, the flow rates of the gases, the temperature and the mass of the crucible are recorded each second. The crucible is also weighed before and after the experiment, both with and without powder. The conversion of the powder at any time is defined as:

$$X(t) = \frac{m_0 - m(t)}{m_0 - m_{0 \to \text{Fe}}}, \tag{3.1}$$

where m_0 is the original mass of the powder, $m(t)$ is the recorded mass at time t and $m_{0 \to \text{Fe}}$ is the theoretical mass of the sample assuming full conversion to metallic iron (using an initial composition of 40 wt.% Fe_2O_3, 58 wt.% Fe_3O_4 and 2 wt.% Fe).

3.2.4 Kinetic analysis approaches

In general, the conversion rate of a gas-solid reaction can be defined as:

$$\frac{dX}{dt} = k_{\text{app}}(T) f(X), \tag{3.2}$$

in which $k_{\text{app}}(T)$ contains the temperature dependency of the conversion rate (constant in an isothermal experiment) and $f(X)$ is a function describing the influence of the conversion extent on the conversion rate. Rate constant $k_{\text{app}}(T)$, often follows the Arrhenius equation:

$$k_{\text{app}}(T) = k_{\text{app},0} \exp\left(-\frac{E_a}{RT}\right), \tag{3.3}$$

with R the universal gas constant, $k_{\text{app},0}$ the pre-exponent factor and E_a the apparent activation energy. $k_{\text{app},0}$ and E_a and $f(X)$ are together also known as the kinetic triplet of gas-solid reactions.

Three common methods exist for extracting the kinetic parameters, each having its own respective advantages and disadvantages. These methods are (1) the model fitting method, (2) the isoconversional method and (3) the "lnln" method. The methods are briefly described below.

Table 3.2: Mathematical models describing the conversion rate dependency on the conversion.

Model	Abbreviation	$g(X)$
Internal diffusion controlled	IDM	$1 - 3(1-X)^{2/3} + 2(1-X)$
Phase boundary controlled	PBC	$1 - (1-X)^{1/3}$
Nucleation and growth	NAG	$-\ln(1-X)^{1/n}$

Different mathematical expressions exist for $f(X)$ based on theoretical kinetic models. Moreover, by integrating Equation 3.2 in time we obtain:

$$g(X) = \int_0^X \frac{1}{f(X)} dX = k_{\mathrm{app}}(T) \cdot t \tag{3.4}$$

The most common expressions for $g(X)$ for gas-solid reactions of spherical particles are given in Table 3.2.

From Equation 3.4 we can conclude that by plotting $g(X)$ as a function of time, we should obtain a straight line, assuming the correct kinetic model is used. Linear regression can thus be used to decide which model best describes the experimental data. This method is often referred to as the model fitting method.

This method however is often also criticized, since multiple models might have a similar shape. This can be observed in Figure 3.5 in which the diffusion model, the phase boundary model and the 1D nucleation and growth model show a similar shape. Fitting any of these models to experimental results may result in a satisfying fit, especially when taking measurement errors into account.

Isoconversional methods overcome this issue by deriving a value for the activation energy as function of the reduction degree. Assuming that the controlling mechanism is not dependent of temperature, at a given value of X, $f(X)$ is constant. Therefore, by performing multiple experiments at different temperatures, E_{a} can be derived as function of conversion X. A drawback of this method is that it can only be used
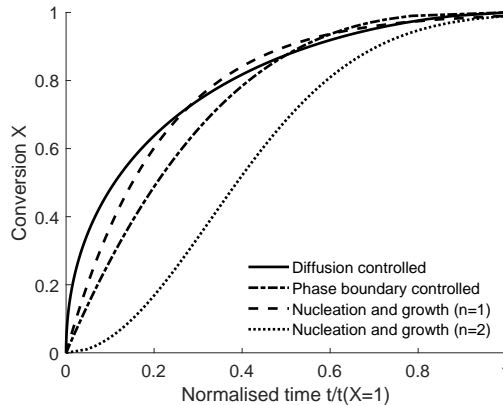

Figure 3.5: Characteristic shapes of mathematical models $g(X)$ of Table 3.2.
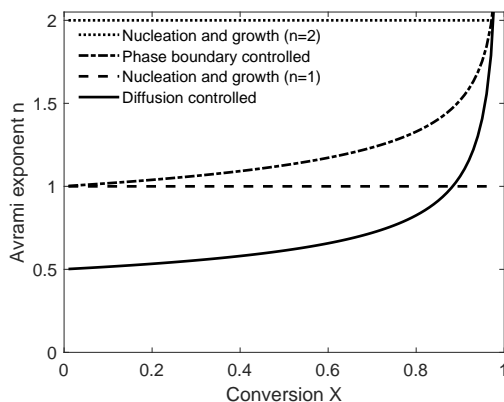
Figure 3.6: Avrami exponent n as function of conversion extent X for the different mathematical models $g(X)$ of Table 3.2.

to derive a value for the activation energy if $f(X)$ does not change as function of the temperature. In the case of mixed controlled reactions (both mass transfer and reaction kinetics are of importance), this assumption usually does not hold (since they scale differently with temperature). The same holds when the reaction consists of multiple reaction steps with intermediate species.

The third method for analyzing gas-solid reaction was developed by Hancock and Sharp [77]. They noticed that, when only taking into account the data between $0.15 < X < 0.5$ all common kinetic models ($f(X)$) could also be described by the nucleation and growth model, if the value of n is used as a fitting parameter (instead of the traditionally used integer values). They suggested to determine the value of n by plotting $\ln\left(-\ln\left(1 - X\right)\right)$ vs $\ln(t)$, since the result would give a straight line with a slope of n:

$$g(X) = -\ln\left(1 - X\right)^{1/n} = k_{\mathrm{app}}(T) \cdot t \tag{3.5}$$
$$\ln\left(-\ln\left(1 - X\right)\right) = n \cdot \ln\left(k_{\mathrm{app}}(T)\right) + n \cdot \ln(t) \tag{3.6}$$
$$\frac{d\ln\left(-\ln\left(1 - X\right)\right)}{d\ln(t)} = n \tag{3.7}$$

Based on the value of n, a suggestion can be made on whether the reaction is reaction or diffusion controlled. A drawback is that one only fits their model to the conversion between 0.15 and 0.5, neglecting data outside that range.

It is well known that the reduction of iron oxides consist of multiple step reactions [72]:

$Fe_2O_3 \rightarrow Fe_3O_4 \rightarrow Fe$ (below 570 °C)
$Fe_2O_3 \rightarrow Fe_3O_4 \rightarrow FeO \rightarrow Fe$ (above 570 °C)
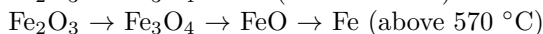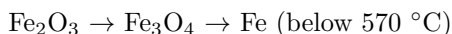
Due to the drawbacks of the first two methods (especially in the case of multi-step reactions), in this study, an extended version of the Hancock and Sharp method is used in combination with the model fitting method to analyze the reduction behavior of the oxides. Instead of plotting $\ln\left(-\ln\left(1 - X\right)\right)$ vs $\ln(t)$, the value of n (often called

the Avrami exponent) is plotted as a function of the conversion X. The resulting curves for the various mathematical models in Table 3.2 are plotted in Figure 3.6.

Comparing Figures 3.5 and 3.10 it is observable that models in Figure 3.5 with a similar shape are now well distinguishable.

3.3 Experimental results

Isothermal TGA tests were performed at different temperatures between 400-900 °C and between 25 and 100 vol% H_2.

3.3.1 Morphological observations

Figure 3.7 shows electron microscope images of the powder after reduction at different temperatures. Different hydrogen concentrations did not lead to differences in the morphology of the sponge iron formed. Therefore, all SEM images presented are from powder reduced at 50 vol% H_2. Compared to the original oxides as seen in Figure 3.2, it can be observed that the powder becomes porous in all reduction experiments. The pore structure, in particular the average pore size, differs between experiments at different temperatures. As the reduction temperature increases, the number of pores decreases, but the pore size increases. This observation matches with the findings of Turkdogan and Vinters [80]. An important effect is that the pore surface area decreases when the pore structure becomes coarser. This suggests that the effective surface area of the produced sponge iron particles reduces with increasing reduction temperature.

It should be noted that, although swelling and shrinkage of particles has been mentioned in literature [81, 82], no clear sign of particle size change can be identified in the SEM images.

Furthermore, at temperatures above 500 °C, agglomeration of the powder was found to occur in the experiments. As temperature increased, this effect gradually became stronger. This agglomeration might have to do with the formation of wüstite as an intermediate species, which is only stable above 570 °C.

3.3.2 Reduction behavior

Figure 3.8 shows the evolution of conversion extent of iron oxide for different temperatures and hydrogen concentrations. Each graph represent experiments performed at a fixed temperature, where each line in the graphs represents an experiment at a specific hydrogen concentrations. The line markers are only used for visualization purposes, since the weight of the samples is recorded at each second during each experiment. In each graph, reference lines are added to show at which points there would be full conversion to magnetite (dashed), wüstite (dotted) and metallic iron (dash-dotted), ideally if the reactions take place step-by-step. If any of the intermediate reactions ($Fe_2O_3 \rightarrow Fe_3O_4$, $Fe_3O_4 \rightarrow FeO$ or $FeO \rightarrow Fe$) would take place at a much faster

(a) 400 °C. **(b)** 500 °C. **(c)** 600 °C.

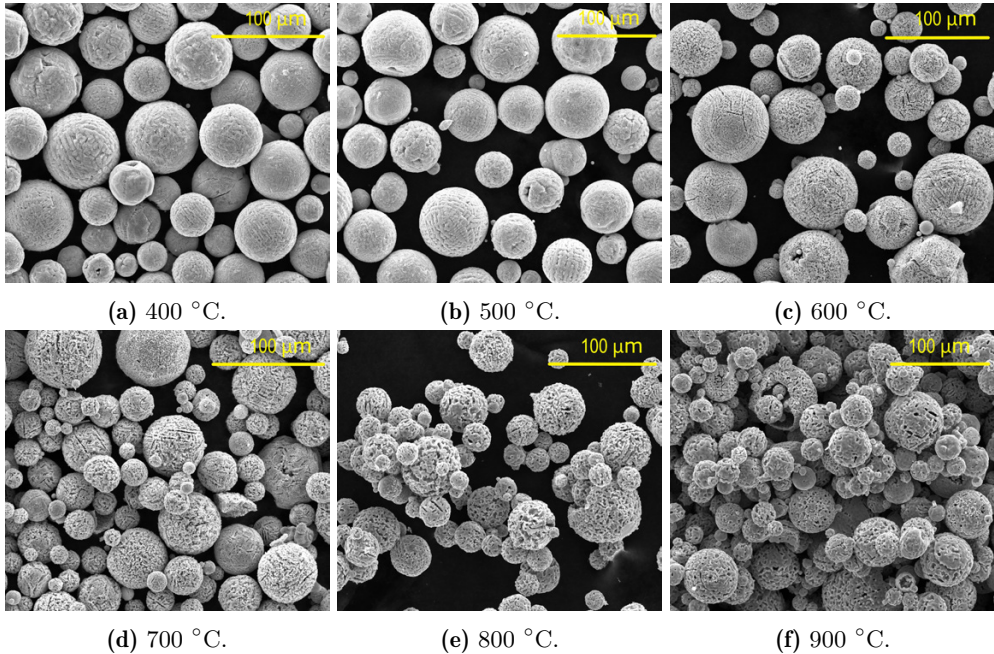**(d)** 700 °C. **(e)** 800 °C. **(f)** 900 °C.

Figure 3.7: Scanning electron microscope images of iron oxide after reduction at various temperatures. Note that there are small differences in the magnification used in the images.

reaction rate compared to the subsequent ones, a clear change in the conversion rate would be observed when the reference lines are crossed. Since no clear transition can be observed, this conclusion cannot be drawn.

It can be observed that at all temperatures a higher hydrogen concentrations leads to a faster conversion rate, as expected. Only for reduction at 800 °C the effect of hydrogen concentrations is different. Initially, a higher hydrogen concentration leads to higher conversion in the same amount of time. However, when the experiment is ran for longer time we observe that the conversion extent at 100 vol% H_2 stagnates, while for 50 vol% H_2 it keeps increasing. After 70 minutes, the powder reduced at 50 vol% H_2 reaches a higher conversion than reduction at 100 vol% H_2. This effect is not observed in the other experiments. A possible explanation for this is that of strong agglomeration occurring, coincidentally leading to this effect.

When comparing reduction curves at different temperatures (with fixed hydrogen concentrations) we can observe that the initial conversion rate increases with temperature. However, while at reduction experiments between 400-600 °C the curves seems to "smoothly" reach to a full conversion, at higher temperatures (700-900 °C) a distinct transition is observable. Initially the conversion rate is fast, but starting from a conversion extent of 0.5-0.6, the conversion rate sharply decreases. In some cases, full conversion is not even reached within the 2 hour time frame of the experiments. Similar observations have been reported in other studies. Piotrowski *et al.* found a similar decrease in conversion rate [70]. They suggested that the sharp decrease was due to

solid state diffusion becoming the limiting factor. Their suggestion agrees with the model of Qu *et al.* [83], in which solid state diffusion of oxygen becomes rate-limiting in the later stage of the reduction.

Another possible explanation for this transition might be agglomeration of the powder. As mentioned before, agglomeration of the powder took place at experiments between 600-900 °C. This agglomeration might hinder mass transfer of hydrogen between particles and thus decrease the conversion rate. Similar agglomeration effects were observed by Morales-Estrella *et al.* [71]. For the case of 900 °C and 100 vol% H_2, the conversion rate goes above 1. This is most likely the result of an error in the weighing of the powder or of the initial composition. A noteworthy effect of this decrease in conversion rate is that full conversion ($X = 1$) is reached faster at low temperatures (400-600 °C), than at higher temperatures (700-900 °C).
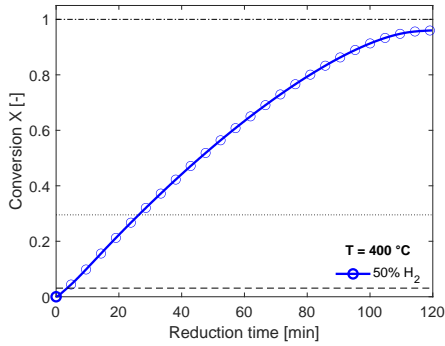
(a) Reduction at a temperature of 400 °C.
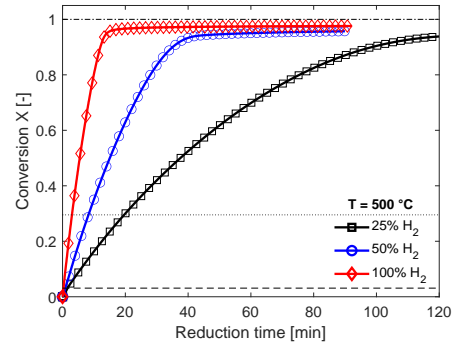
(b) Reduction at a temperature of 500 °C.
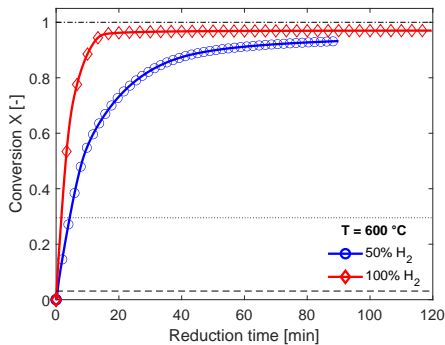
(c) Reduction at a temperature of 600 °C.
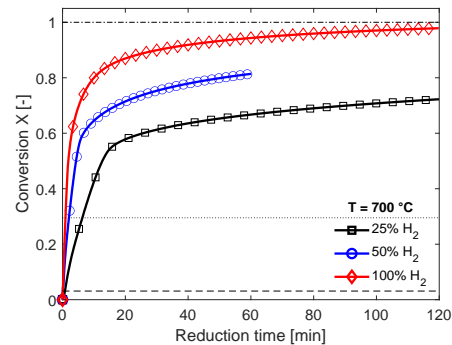
(d) Reduction at a temperature of 700 °C.
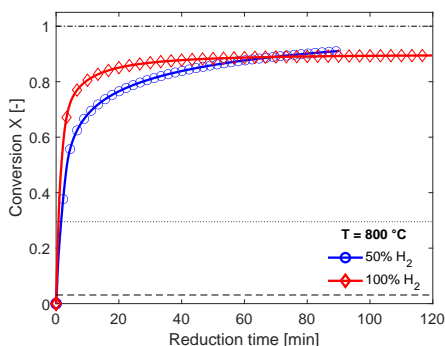
(e) Reduction at a temperature of 800 °C.
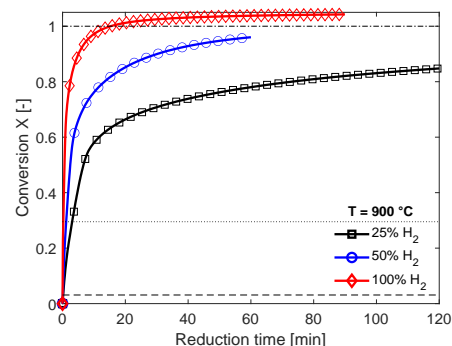
(f) Reduction at a temperature of 900 °C.

Figure 3.8: Influence of hydrogen gas concentration on iron oxide reduction at temperatures of 400-900 °C. The weight of the sample is measured at every second, which means that the markers are only added for visualization purposes. The black dashed, dotted and dash-dotted horizontal lines in the figure represent 100% conversion to magnetite, wüstite and metallic iron, respectively, if the reactions take place step-by-step.

3.4 Kinetic results

3.4.1 Model selection

The result of the standard model fitting method for the cases of 500, 600 and 700 °C can be seen in Figure 3.9. Using these cases as an example, we can observe two issues with using solely this method. In the case of 500 °C both the phase boundary controlled model and the nucleation and growth model ($n \approx 1.09$) seem to fit the experimental result equally well. The selection of the correct kinetic mechanism is therefore up for interpretation. For the cases of 600 and especially 700 °C, none of the models fit the experimental data well, suggesting that a multistep mechanism is required.

To better understand the reaction mechanism, the extended Hancock and Sharp method explained in Section 3.2.4 is used to further analyze the experimental results and to improve the interpretation of the model fitting method. Figure 3.10 shows the Avrami exponent for the cases of 500, 600 and 700 °C. For the 500 °C
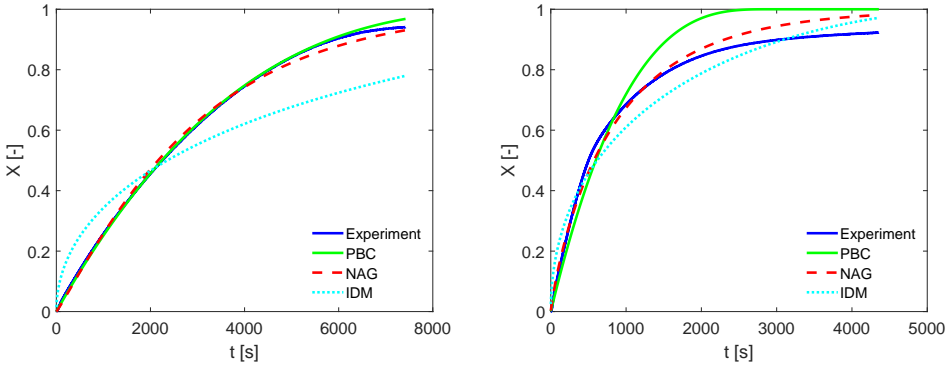
(a) Fitting results at 500 °C and 25 vol% H_2. **(b)** Fitting results at 600 °C and 50 vol% H_2.
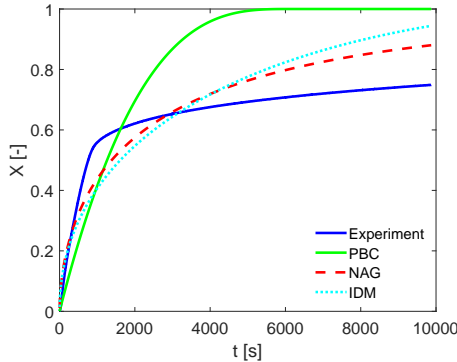
(c) Fitting results at 700 °C and 25 vol% H_2.

Figure 3.9: Fitting results using the model fitting method.

case, it can clearly be observed that the data follows the phase boundary controlled model almost perfectly. The deviation of the experimental results at high conversion ($X > 0.8$) is due to small measurement errors in the sample weight and initial composition. The deviation at low conversion ($X < 0.05$) is most likely due to the conversion of hematite to magnetite. This step is generally known to be significantly faster than the magnetite to iron reaction. However, since this conversion happens early on in the experiment, it is intertwined with stabilization of the hydrogen-nitrogen gas ratio. It is therefore difficult to obtain good kinetic data for this reduction step. The rest of the reaction follows a simple phase boundary reaction, often referred to as a reaction controlled shrinking core model. The low temperature experiments (400 and 500 °C) can therefore be evaluated by fitting a single phase boundary reaction:

$$X = 1 - (1 - k_{\mathrm{app}} \cdot t)^3 \tag{3.8}$$

Evaluating the cases of 600 °C and 700 °C, it can be observed that the experimental data does not solely follow any of the single step analytical models. A clear transition can be observed at $X \sim 0.1$ and $X \sim 0.5$. This suggests a multi-step reaction mechanism is required to describe the reduction behavior at these higher temperatures.

3.4.2 Multi-step mechanism

To analyze the higher temperature reactions, a multi-step mechanism is required, to account for the intermediate species. Defining our initial masses of hematite, magnetite, wüstite and iron as $m_{\mathrm{H},0}$, $m_{\mathrm{M},0}$, $m_{\mathrm{W},0}$ and $m_{\mathrm{F},0}$, respectively, and setting up the conservation of mass, we can define our masses at any time as:

$$m_{\mathrm{H}} = m_{\mathrm{H},0}(1 - X_{\mathrm{H}}) \tag{3.9}$$

$$m_{\mathrm{M}} = \left(m_{\mathrm{M},0} + \frac{2M_{\mathrm{M}}}{3M_{\mathrm{H}}} m_{\mathrm{H},0} X_{\mathrm{H}} \right) (1 - X_{\mathrm{M}}) \tag{3.10}$$

$$m_{\mathrm{W}} = \left(m_{\mathrm{W},0} + \frac{3M_{\mathrm{W}}}{M_{\mathrm{M}}} \left(m_{\mathrm{M},0} + \frac{2M_{\mathrm{M}}}{3M_{\mathrm{H}}} m_{\mathrm{H},0} X_{\mathrm{H}} \right) X_{\mathrm{M}} \right) (1 - X_{\mathrm{W}}) \tag{3.11}$$

$$m_{\mathrm{F}} = m_{\mathrm{F},0} + \frac{M_{\mathrm{F}}}{M_{\mathrm{W}}} \left(m_{\mathrm{W},0} + \frac{3M_{\mathrm{W}}}{M_{\mathrm{M}}} \left(m_{\mathrm{M},0} + \frac{2M_{\mathrm{M}}}{3M_{\mathrm{H}}} m_{\mathrm{H},0} X_{\mathrm{H}} \right) X_{\mathrm{M}} \right) X_{\mathrm{W}} \tag{3.12}$$

in which M_i stands for the molar masses of the different species and X_i is the conversion of intermediate reaction step. For each of these conversions, we can again choose the models listed in Table 3.2. The fractions 2/3 and 3/1 result from the stoichiometry between the different oxides (Fe_2O_3 to Fe_3O_4 and Fe_3O_4 to FeO, respectively). The total conversion (which we measure experimentally) can then be defined as:

$$X_{\mathrm{tot}} = \frac{m_{\mathrm{tot},0} - m_{\mathrm{tot}}}{m_{\mathrm{tot},0} - m_{\mathrm{tot,inf}}} \tag{3.13}$$

in which m_{tot} is the summation of the masses of hematite, magnetite, wüstite and iron and the subscripts $_0$ and $_{\mathrm{inf}}$ stand for initial mass and mass after full conversion (all X_i are 1).
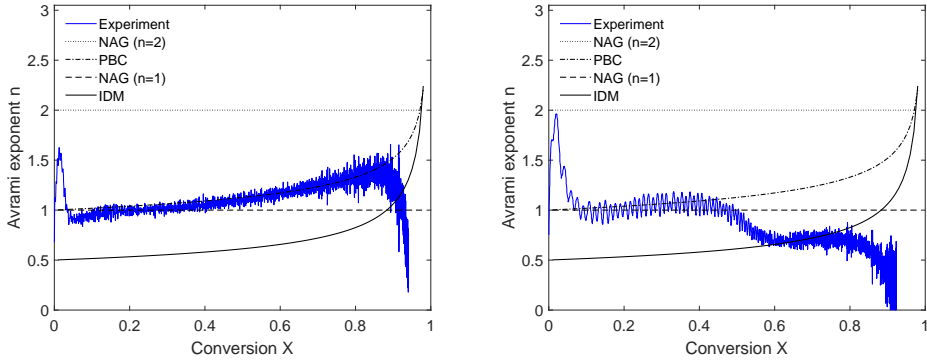
(a) 500 °C and 25 vol% H_2. The phase boundary controlled model (PBC) matches best with the data.

(b) 600 °C and 50 vol% H_2. Between $0.1 < X < 0.4$ data matches with the phase boundary reaction. Between $0.6 < X < 0.8$, n decreases sharply. None of the models will therefore be able to correctly describe the entire reaction.
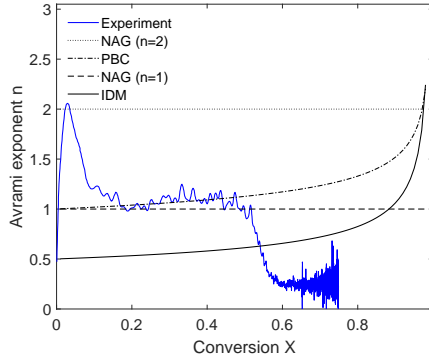
(c) 700 °C and 25 vol% H_2. Between $(0.15 < X < 0.5)$ the data matches with the phase boundary reaction. Afterwards, the value of n drops significantly and does not match any of the models.

Figure 3.10: Exponent n as a function of conversion X for various temperatures.

To select the correct combination of models, the following assumptions are made:

- The reactions occur via a shrinking core principle, where the reaction leaves a shell of "lower" oxide and the reaction fronts travel inwards.

- In the case of an internal diffusion model, the diffusion of hydrogen towards the reaction front is limiting and the concentration of hydrogen goes to the equilibrium concentration when approaching the reaction front. This means that only the first reaction step (hematite to magnetite) can be diffusion limited, with subsequent reactions (with reaction fronts closer to the surface of the particle), being only nucleation and growth or phase boundary controlled.
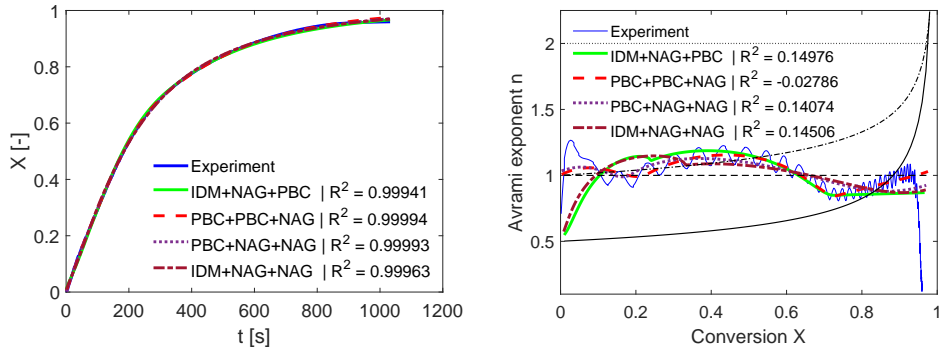
(a) Model fitting results of 4 different combinations of models, using a multistep mechanism.

(b) Avrami exponent as a function of reduction degree.

Figure 3.11: Fitting results at 600 °C and 100 vol% H_2 using multistep kinetics. The legend describe the model combinations used for X_H, X_M and X_W.

- Each reaction (X_i) can be described by one of the models from Table 3.2.

Different combinations of models are tested and the resulting fits are compared in both the conversion versus time as well as the "Avrami exponent" versus conversion graph. The results for higher temperature cases (600-900 °C) and 100 vol% H_2 are presented in Figures 3.11-3.14. The coefficients of determination (R^2) are mentioned in the legend of the figures. It should be noted that the fitting occurs in the X, t-domain, while the Avrami exponent graph aids in selecting the correct model. Comparing the results, the conversion versus time graphs show all models fitting roughly equally well, as illustrated earlier. However, when looking at the Avrami exponent over conversion graphs, the models show more differences. The model that seems to fit all cases best, is the "PBC+NAG+NAG" model, meaning that the hematite to magnetite reaction is controlled by a phase boundary reaction, while the magnetite to wüstite and the wüstite to iron reaction are dominated by nucleation and growth.

3.4.3 Kinetic parameters

Using the models selection, the apparent reaction rates and nucleation and growth exponent can be determined. The apparent reaction rate can however be separated in the influence of the hydrogen and water vapor concentration and the influence of the temperature on the conversion rate:

$$k_{app}(T, C_{H_2}, C_{H_2O}) = k_{app}(T) \cdot (C_{H_2} - C_{H_2O}/K)^m, \qquad (3.14)$$

in which $k_{app}(T, C_{H_2}, C_{H_2O})$ is the apparent reaction rate from Equation 3.8 in s^{-1}, K is the equilibrium constant of the reaction and C_{H_2} and C_{H_2O} are the hydrogen and water vapor concentration in the gas phase in mol/m^3, respectively. Due to the relatively high hydrogen flow rates used in these experiments compared to the little amount of powder, the influence of water vapor can be neglected ($C_{H_2O} \approx 0$).
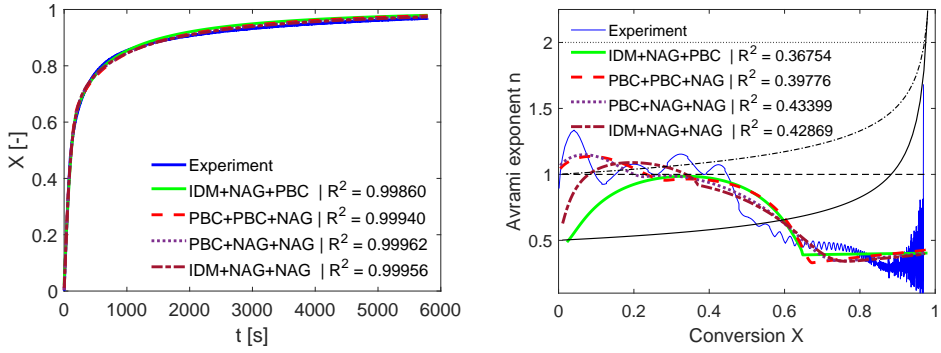
(a) Model fitting results of 4 different combinations of models, using a multistep mechanism.

(b) Avrami exponent as a function of reduction degree.

Figure 3.12: Fitting results at 700 °C and 100 vol% H_2 using multistep kinetics. The legend describe the model combinations used for X_H, X_M and X_W.
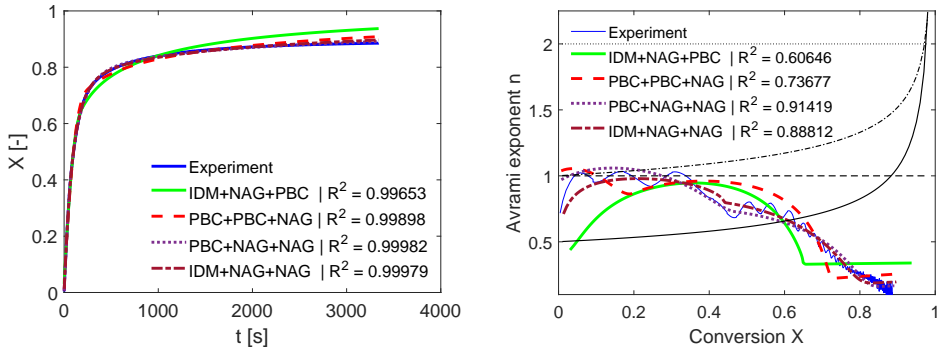
(a) Model fitting results of 4 different combinations of results, using a multistep mechanism.

(b) Avrami exponent as a function of reduction degree.

Figure 3.13: Fitting results at 800 °C and 100 vol% H_2 using multistep kinetics. The legend describe the model combinations used for X_H, X_M and X_W.

It should be noted that the apparent reaction rate can also be dependent on the particle size d_p. However, since all measurements are performed with the same particle size distribution, this influence can not be extracted from the data presented here.

In the case of 500 °C (single phase boundary reaction) the dependency of the reaction on the hydrogen concentration appeared to have an order of 1.4 (exponent m in Equation 3.14), as can be observed from the slope in Figure 3.15.

For higher temperatures, the resulting gas dependency of each reaction step is shown in Figure 3.16. It should be noted that for the experiments of 600 and 800 °C, only two data points are available and as such care should be taken in interpreting the results.
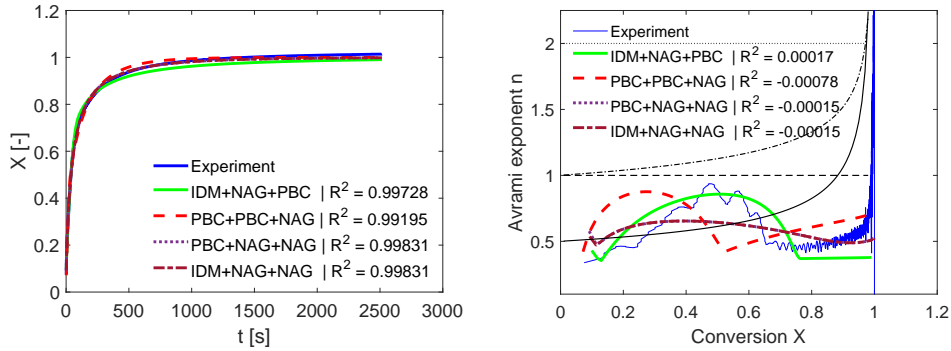
(a) Model fitting results of 4 different combinations of results, using a multistep mechanism.

(b) Avrami exponent as a function of reduction degree.

Figure 3.14: Fitting results at 900 °C and 100 vol% H_2 using multistep kinetics. The legend describe the model combinations used for X_H, X_M and X_W.
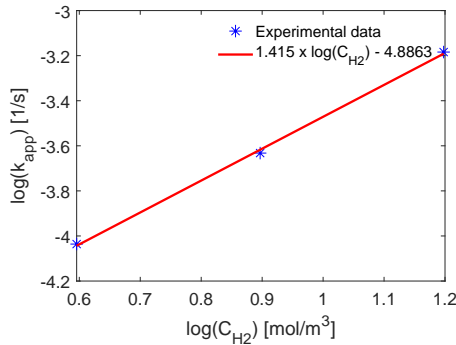
Figure 3.15: Logarithmic graph of apparent reaction rate versus hydrogen concentration at 500 °C. Linear regression is used to determine the reaction dependency on hydrogen concentration.

However, the gas dependency of apparent reaction rate seems to be in the order of 1-2.5 for most cases, except for the experiment at 800 °C. Looking back at Figure 3.8e, we can see that the conversion at 800 °C and a 100 vol% hydrogen environment completely stagnates after 40 minutes and does not further increase. This is most likely due to severe sintering occurring. Therefore this experiment was assumed to be faulty and the accompanied kinetic data is neglected. For the gas dependency for 400 and 800 °C, the results of 500 °C and the mean of 700 and 900 °C are assumed, respectively. A summary of the kinetic parameters obtained are presented in Table 3.3.

Since the exponent of the nucleation and growth model for both the magnetite to wüstite and the wüstite to iron reaction change as function of temperature, as can be seen in Table 3.3, it is impossible to derive a meaningful activation energy for these reactions. As mentioned before, since the hematite to magnetite reaction occurs early

Table 3.3: Apparent reaction rate, nucleation and growth exponent n and gas order m resulting from the single step (400-500 °C) and multistep (600-900 °C) analysis.

T [°C]	X_{tot} (PBC)							
	$k_{app}(T)$	m						
400	3.41E-06	1.42[1]						
500	1.30E-05	1.42						
	X_H (PBC)		X_M (NAG)			X_W (NAG)		
	$k_{app}(T)$	m	$k_{app}(T)$	n	m	$k_{app}(T)$	n	m
600	1.54E-04	1.55	1.65E-04	1.15	1.52	0.89E-04	0.86	1.79
700	3.61E-04	1.49	5.12E-04	1.2	1.32	0.93E-04	0.36	2.23
800[2]	2.62E-04	2[3]	2.62E-04	1.09	1.5[3]	2.62E-04	0.42	2.33[3]
900	2.45E-04	2.48	8.25E-04	0.97	1.68	2.65E-04	0.45	2.43

[1] The gas dependency at 400 °C is assumed equal to that at 500 °C.

[2] The kinetic parameters are based solely on the 50 vol% H_2 experiment.

[3] The gas dependency at 800 °C is based on the mean gas dependency of 700 and 900 °C.

on in the experiment, it is intertwined with the stabilization of the hydrogen-nitrogen gas ratio and therefore no activation energy is determined.

These results described in this work provide an initial understanding in the reduction of combusted iron particles. More research is required to investigate the influence of, among others, particle size and water vapor concentration.

To investigate the reduction behavior of combusted iron powder with hydrogen at higher temperatures, trial experiments (900-1100 °C) in a high temperature drop tube furnace are performed. The results are presented in Appendix A.2. The results indicate that reduction at these higher temperatures is possible, but the residence times in the drop tube furnace (< 1 s) were to short to reach full conversion.
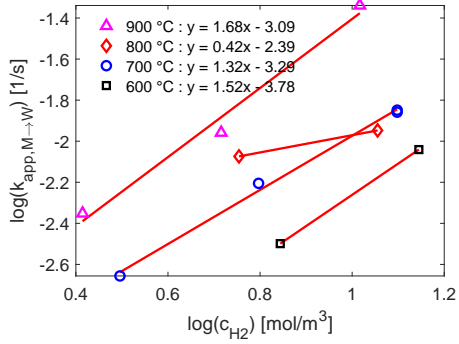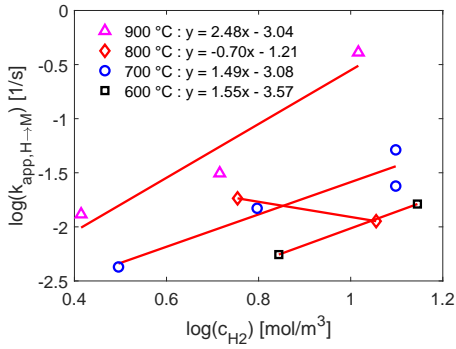
(a) Logarithmic graph of apparent reaction rate versus hydrogen concentration at various temperatures for the hematite to magnetite reaction step.

(b) Logarithmic graph of apparent reaction rate versus hydrogen concentration at various temperatures for the magnetite to wüstite reaction step.
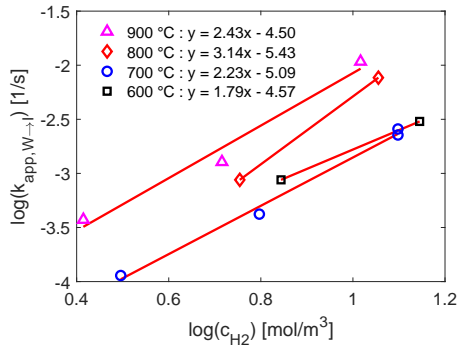
(c) Logarithmic graph of apparent reaction rate versus hydrogen concentration at various temperatures for the wüstite to iron reaction step.

Figure 3.16: Dependency off the apparent reaction rates on the gas concentration for the elementary reaction steps of the high temperature multistep model.

3.5 Conclusions

The reduction kinetics of iron oxides fines by hydrogen was investigated using thermo-gravimetric analysis in the temperature range of 400-900 °C. The powder, consisting of a mixture of hematite and magnetite, was produced by combustion of iron in air. During reduction, the removal of oxygen leads to formation of pores in the particles, and the morphology (pore size, amount of pores) of the products strongly depends on the reduction temperature. Fewer, but larger pores were observed for reduction at higher temperature. The pore morphology was found to be independent of hydrogen concentration. Mathematical modeling of the experimental data of conversion, using an extended version of the Hancock and Sharp method in combination with the model fitting method, showed that the reaction is entirely controlled by a single phase bound-ary reaction at 400 and 500 °C, while it must be described by a multistep mechanism at higher temperatures. The method showed that, at temperatures between 600 and 900 °C, the hematite to magnetite reaction was controlled by a phase boundary reac-tion, while the magnetite to wüstite and the wüstite to iron reactions were limited by nucleation and growth. The total reaction seems to be dependent on the gas concen-tration of hydrogen with a power of 1.4 at low temperatures. Noteworthy is that full conversion to metallic iron was reached faster at 500 °C then at higher temperatures. This investigation provides further understanding in iron oxide reduction with hydro-gen, especially in the field of metal fuels, and provides a valuable new technique for analyzing kinetic data.

4 Sintering

The setup and some of the results presented in this chapter are the result of the bachelor theses of Hannes Kempe and Anke Smeets. Parts of this chapter are published in: C.J.M. Hessels et al. Particuology, 83 (2023) 8-17.
Background image: scanning electron microscope image of iron powder cyclically oxidized and reduced in a thermogravimetric analyzer. See Appendix A.1 for more details.

Abstract

Sintering behavior of micron-sized combusted iron powder is studied in a packed bed reactor, at various temperatures under inert (nitrogen) and reducing (hydrogen) conditions. Compression tests are subsequently used to quantify the degree of sintering. The experimental results are consistent with a sintering model that describes the formation of a solid bridge force through solid state surface diffusion of iron atoms. Sintering of combusted iron occurs at temperatures $\geq 575\,°C$ in both nitrogen and hydrogen atmospheres and increases exponentially with temperature. The observed decrease in reduction rate at high temperatures is not caused by the sintering process but by the formation of wüstite as an intermediate species leading to the formation of a dense iron layer. Iron whiskers form at high temperatures ($\geq 700\,°C$) in combination with low reduction rates ($\leq 25\,vol\%\,H_2$), leading to the formation of sub-micron fines.

4.1 Introduction

In DRI research employing hydrogen, sintering and sticking are common problems, hindering granular solid flow in shaft furnaces and causing defluidization in fluidized beds [17, 18, 69, 84–88]. In Chapter 3, sintering occurred at high temperature, which possibly limited the reaction rate. Similar observations where made by Kuhn *et al.* [89]. Incompletely reduced iron powder has a lower energy density, thereby negatively affecting the efficiency of the metal energy carrier cycle. Besides a possible decrease in reaction rate, sintering also results in a growth of mean particle size. Using a reduced powder with a larger mean particle size possibly requires milling/grinding steps before the subsequent combustion stage (thereby lowering the cycle's efficiency). Kuhn *et al.* [89] recently developed a model to determine the overall efficiency of the iron energy carrier cycle. They pointed out that more information on the sintering behavior of the powder is vital for accurate predictions of the cycles efficiency.

Sintering of particles has been studied for many years [90, 91]. Kuczynski [92] derived a sintering model for metallic particles, based on solid state diffusion of material towards the contact point between two particles. A neck connecting the two particles forms and subsequently grows in time. The driving force in this case is the decrease in surface free energy of the two particles. Mikami *et al.* [93] showed that compression tests can be applied to determine the force required to break this metallic neck. They also were able to derive a correlation between the sintering force and the defluidization behavior. This theory for defluidization has subsequently been used in various experimental and numerical works [94–100]. However, all these works study the defluidization of either pre-reduced (atomized) iron powders or iron ore/oxide powders in an inert (N_2) environment. Sintering cannot be studied without considering the changes of morphology and composition of the powder during the reduction process. Many studies have investigated the morphological/microstructure evolution of iron oxide particles undergoing reduction [67, 83, 101–103]. Reduction of combusted iron using hydrogen creates porous (sponge) iron, where the pore morphology mostly depends on the temperature (see Chapter 3). This results in a change in material properties (strength
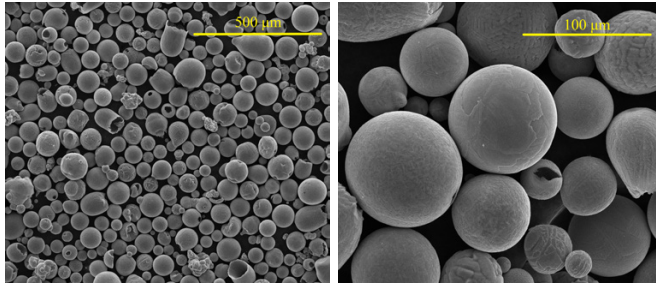
Figure 4.1: Scanning electron microscope images of the combusted powder used for the reduction/sintering experiments.

and solid state diffusion), which influence the sintering process. Therefore the existing theoretical models which correlate the sintering to the (de)fluidization cannot directly be applied for combusted iron powder during reduction.

In this work, the initial stage of the sintering of combusted iron powder undergoing reduction is investigated. Sintering experiments are performed in a packed bed reactor in nitrogen (as validation) and in various hydrogen molar fraction atmospheres. Compression experiments are used to measure the sintering force. In Section 4.2, the material used, and the two setups (packed bed and compression) are described. Successively, in Section 4.3, the sintering results in nitrogen and undergoing reduction in various hydrogen concentrations are presented. Finally, the main conclusions are presented in Section 4.4.

4.2 Materials and methods

4.2.1 Material

The powder in this study is the product of iron powder (Rio Tinto ATOMET95) combusted in a pilot scale industrial burner and recovered from the cooling section. The microstructure of powder from the same burner was studied in detail by Choisez *et al.* [21]. Figure 4.1 shows scanning electron microscopy images (SEM) of the powder for two magnifications. The particles are mostly spherical. The holes found in some of the particles as well as the tulip shaped capsules are the results of micro-explosions occurring during the combustion process [21, 31–33, 52]. The surface morphology differs slightly between particles, most likely resulting from different local conditions inside the combustion chamber. The lines on the surface of the particles correspond to grain boundaries between hematite and magnetite as well as between individual magnetite crystals with different crystal orientations [21]. The measured material properties of the powder are given in Table 4.1. The (volume-based) particle size distribution is given in Figure 4.2. It can be observed that nearly all particles are between 10 and 110 µm. The Sauter mean diameter d_{32} is 53.5 µm.

Table 4.1: Properties of the combusted iron powder.

Property	Value
Density	*measuring cylinder*
Bulk density, ρ_b	2912 kg/m^3
Particle density, ρ_p	4601 kg/m^3
Size	*laser diffraction*
Sauter mean diameter, d_{32}	53.5 μm
Composition	*X-ray diffraction*
Iron, Fe	2 wt%
Magnetite, Fe$_3$O$_4$	58 wt%
Hematite, Fe$_2$O$_3$	40 wt%
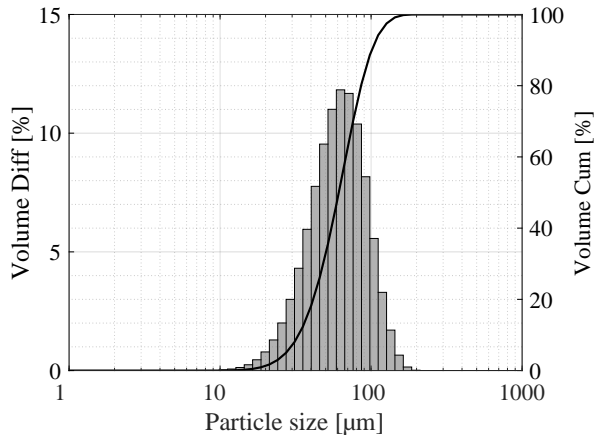
Figure 4.2: Particle size distribution of the combusted powder, determined via laser diffraction. The bars correspond to the left axis, while the solid line corresponds to the right axis.

4.2.2 Packed bed reactor

A schematic and a photograph of the reactor are shown in Figure 4.3. The stainless-steel reactor (type 316) has an inner diameter of 100 mm and a height of 160 mm. H$_2$ and N$_2$ flows (N5.0 purity) are provided using mass flow controllers (Bronkhorst EL-Flow). The gas passes through a vertical tube running alongside the reactor, in order to preheat the gas before it enters the reaction chamber. The powder samples are placed in porous aluminum oxide crucibles (5 mm inner diameter), which are placed on top of a perforated plate located 25 mm above the bottom of the reactor. The supplied flow can thus flow around the crucibles. A thermocouple (Tempcontrol MTK-6) is inserted from the top to measure the (gas) temperature close to the location of the sample. Two semi-cylindrical heating elements (Thermcraft VF-180-6-6) are placed around the reactor and controlled using the thermocouple in order to reach the desired temperature inside the reactor. The top and bottom of the reactor are insulated using ceramic plates containing cutouts for the thermocouple and the gas lines.
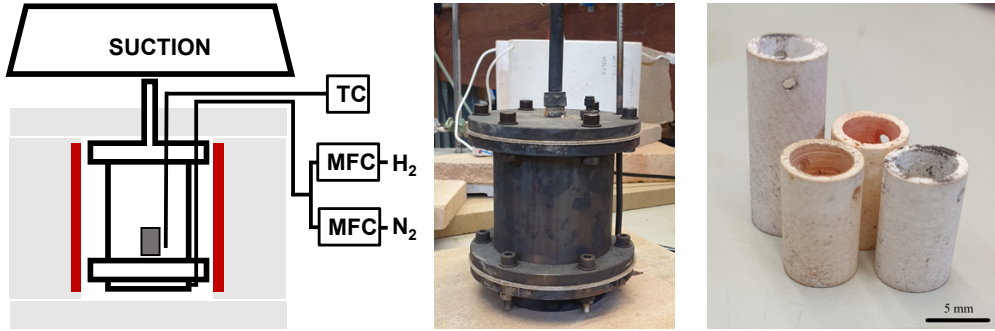
Figure 4.3: Schematic (left) and photograph (centre) of the packed bed reactor. The heating elements indicated in red in the schematic, are visible (white) behind the reactor in the photograph. The right image shows the aluminum oxide crucibles (marked gray in the schematic), which are used inside the reactor. TC = thermocouple, MFC = mass flow controller.

Before each sintering experiment, around 1 gram of powder (total) is poured into the crucibles, without further shaking, vibrating or tamping down. The crucibles are subsequently positioned on the perforated plate inside the cold reactor. The reactor is heated up while nitrogen (0.5 NLPM) is supplied to the reactor. When the desired temperature is reached, the gas is switched to the desired H_2:N_2 ratio (total flowrate of 2 NLPM) and a timer is set. After a "sintering time" of either 30 or 60 minutes, the inflow is switched back to 100 vol% nitrogen (0.5 NLPM) and the reactor is allowed to cool down. Experiments are performed between 400-800 °C with nitrogen and 450-800 °C with hydrogen using 10, 25 and 50 vol% H_2. The crucibles together with the powder are weighed beforehand and afterwards, to obtain the mass change. The reduction degree (X) is calculated by dividing the mass change obtained during an experiment ($\Delta m_{\text{experiment}}$) by the maximum theoretical mass change (Δm_{theory}), based on the initial powder weight and composition, and complete conversion to Fe:

$$X = \frac{\Delta m_{\text{experiment}}}{\Delta m_{\text{theory}}} \tag{4.1}$$

4.2.3 Compression tests

Examples of the produced pellets, which retain the cylindrical shape of the crucible after sintering, are displayed in Figure 4.4. Uni-axial compression test are carried out on these samples at room temperature. An electric motor is used to compress the cylindrical sample uniformly (at 10 μm/s) between two flat surfaces. A load cell ($\leq$100 N) is used to directly measure the force applied in time. The force is recorded every 16 ms. Uni-axial compression is chosen instead of diametral compression to more closely align the results with a typical milling process. During milling/crushing the forces acting on the powders/agglomerates are typically due to compression, while a diametrical compression test is used to measure the tensile properties of the material.

For the analysis, a similar approach to Mikami *et al.* [93] is followed. The measured force during the compression test relates to the stress in the pellet sample (σ_{pellet})
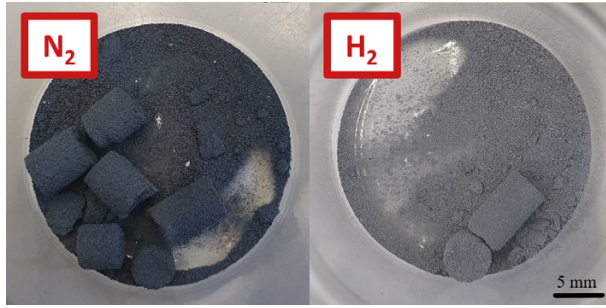
Figure 4.4: Examples of created pellets by sintering in nitrogen and hydrogen.

by:

$$\sigma_{\text{pellet}} = \frac{4F}{\pi W^2} \tag{4.2}$$

in which F is the measured force and W is the diameter of the pellet.

Secondly, Rumpf derived an equation correlating the stress in the pellet with that of the force between two particles [104]:

$$\sigma_{\text{pellet}} = \frac{1 - \varepsilon}{\varepsilon} \frac{F_{\text{c}}}{d_{\text{p}}^2} \tag{4.3}$$

in which ε is the void fraction of the pellet and d_p is the particle size (in this case the Sauter mean diameter d_{32} is used). The void fraction is assumed to be 0.4, based on poured random packing of mono-dispersed spheres. The void fraction is also assumed to be independent of the degree of sintering, since this study focuses on the initial phase of the sintering (neck formation) where the formed neck radius is only a few micrometer large ($< 10\%$ of particle radius). Therefore, the decrease void fraction is expected to be very small and is neglected in this study.

The cohesive force between two particles (F_{c}) can be calculated by:

$$F_{\text{c}} = \pi x^2 \sigma_{\text{sb}} \tag{4.4}$$

with x the neck radius between two particles and σ_{sb} the strength of the neck. Kuczynski[92] derived two models for the neck formation between metallic particles, based on either surface or volume diffusion of atoms towards the neck. See Figure 4.5 for a schematic of the sintering process of two particles. Matsumura [105] and Fischmeister and Zahn [106] found that for ferrous particles at temperatures below 1000 °C, the neck formation based on surface diffusion agrees best with experimental results. The growth of the neck in time can then be calculated by:

$$\frac{\mathrm{d}x^7}{\mathrm{d}t} = \frac{56\gamma\delta^4}{kT} D_s a^3 \tag{4.5}$$

with γ the surface free energy, δ the lattice spacing, k the Boltzmann constant and T the temperature. a is the local curvature radius of the particle, which can be assumed
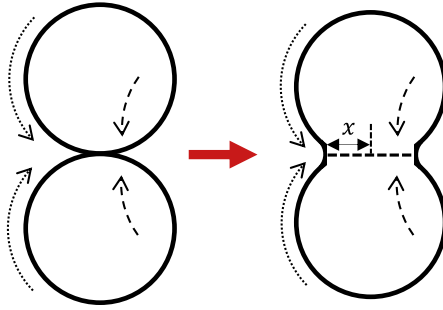
Figure 4.5: Schematic of sintering of two particles, with formed neck of radius x. The dotted external arrows represent sintering by surface diffusion of atoms, while the dashed internal arrows represent sintering by volume diffusion.

to be $\frac{1}{2}d_{32}$ for smooth particles [94]. D_s is the solid state surface self-diffusion coefficient of the material, which can often be described using an Arrhenius expression:

$$D_s \quad = \quad D_{0,s} \exp\left(-\frac{E_a}{RT}\right) \tag{4.6}$$

in which $D_{0,s}$ is the frequency factor, E_a the activation energy and R the universal gas constant.

For the sintering experiments in nitrogen, material properties of magnetite are used, since: (1) The solid-state diffusivity of iron is typically much higher in magnetite than in hematite [61], and (2) the initial material predominantly exists of magnetite. It is therefore reasonable to assume that the magnetite phase is the main cause of sintering. For the sintering experiments with hydrogen, properties of iron are used, since the outer layer quickly reduces to iron during the reduction process [61].

The correlations from Gorton *et al.* [107] are used to determine the lattice spacing δ of magnetite and iron at elevated temperature:

$$\delta_{\text{magnetite}} \quad = \quad 8.3939 + 8.46 \cdot 10^{-5}T + 5.52 \cdot 10^{-8}T^2 \text{ Å} \tag{4.7}$$
$$\delta_{\text{iron}} \quad = \quad 2.8658 + 3.747 \cdot 10^{-5}T + 8.59 \cdot 10^{-9}T^2 \text{ Å} \tag{4.8}$$

The strength of the neck σ_{sb} is known to be different from the bulk material and can even change depending on the neck size, due to the high vacancy concentration present in the neck [93]. This parameter is therefore used to match the model with experimental observations. The other material properties used to analyze the experiments are listed in Table 4.2.

It should be noted that the neck size is determined by solving Equation 4.5 for the entire temperature profile during an experiment, including the heat-up and cool-down periods. Figure 4.6 shows a typical temperature profile and neck size evolution during a sintering experiment. The heat-up temperature profile is calculated based on a polynomial fit of experimental results, while the cooling-down profile is approximated by an exponential decay. The majority of the neck already forms during the heat-up period before the (defined) isothermal sintering time. The effect of this neck growth during heat-up increases with temperature.

Table 4.2: Material properties used in sintering model.

Parameter	Value		Unit
	Magnetite	*Iron*	
Surface tension, γ	1.44[1]	2.1[2]	N/m
Frequency factor, $D_{0,\mathrm{s}}$	5.2[3]	2[4]	$\mathrm{cm^2/s}$
Activation energy, E_a	230[3]	239[4]	kJ/mol
Void fraction, ε	0.4		-
Particle size, d_{32}	53.5		μm
Curvature radius, a	$\frac{1}{2}d_{32}$		m
Pellet diameter, W	5		mm
Boltzmann constant, k	$1.381 \cdot 10^{-23}$		J/K
Gas constant, R	8.314		J/(mol·K)

[1]Navrotsky *et al.* [108]; [2]Schönecker *et al.* [109]; [3]Himmel *et al.* [110]; [4]Buffington *et al.* [111]
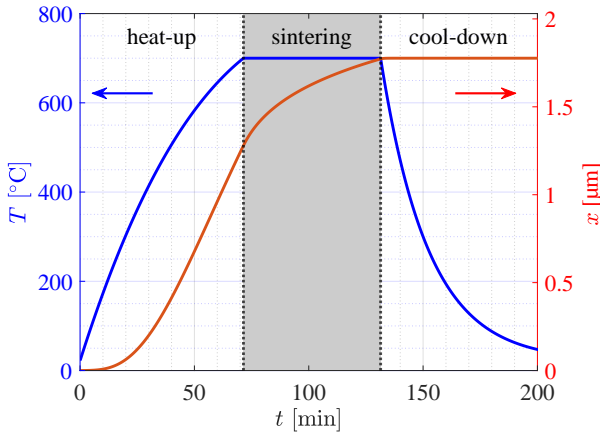
Figure 4.6: Temperature (T) profile in blue and neck size (x) in red during an entire sintering experiment (heat-up, isothermal sintering and cool-down). Neck size is calculated using Equation 4.5. This example is for a sintering experiment of combusted iron in N_2 at 700 °C for 60 minutes.

(a) 500 °C   (b) 600 °C   (c) 700 °C   (d) 800 °C
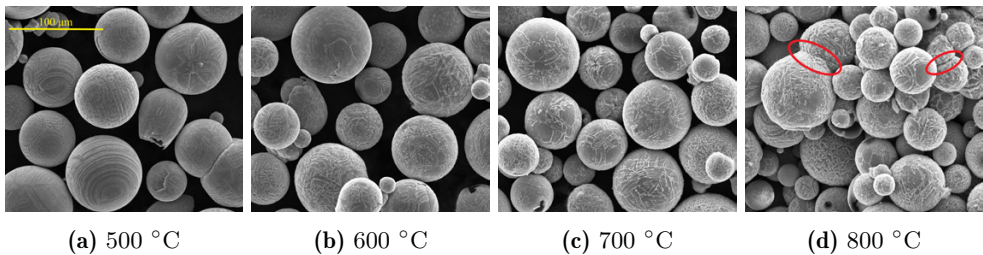
Figure 4.7: Scanning electron microscopy images of the powder after 60 minutes of sintering in nitrogen at various temperatures. The formed necks are marked with red ovals in the most right image.

4.3 Results

4.3.1 Experiments under non-reactive condition in nitrogen

Morphology

Figure 4.7 shows the morphology of the powder after isothermal sintering in nitrogen for 60 minutes at 500 up to 800 °C. The grain boundaries (surface lines) become more visible after sintering at higher temperature. This is due to the increase of iron diffusivity with temperature in combination with the large amount of lattice vacancies at these grain boundaries. Iron will therefore diffuse towards and along the grain boundaries, especially at the surface, in order to reduce the local vacancy concentration [61]. This is in line with earlier observations that the sintering process is mainly caused by surface diffusion [105, 106].

Sintering force

Figure 4.8 shows the force required to break the neck between two particles, determined experimentally by the compression test and numerically using Equations 4.4 and 4.5. A neck strength (σ_{sb}) of 150 MPa is used in the model. The maximum force recorded during the compression tests is used for the analysis and then converted into the force between two particles using Equations 4.2 and 4.3. Note that the temperature on the x-axis matches with the isothermal region of Figure 4.6. Although part of the sintering occurs during the heat-up period, the maximum temperature is still the main cause of neck growth due to the exponential effect in Equation 4.5, in comparison to the effect of contact time. Below 575 °C, no observable sintering takes place. Thus, no pellets are formed and no compression tests are carried out on these samples. The significantly lower measured force after sintering at 800 °C and 30 minutes is considered to be an outlier, since (1) the results at the same temperature, but after 60 minutes shows the same trend as the results at lower temperature and (2) no change in mechanism is expected based on the Fe-O phase diagram or literature on solid-state diffusion [61, 112].

The results show that the force required to break the solid bridge between two particles increases significantly with temperature but is nearly independent of sintering time within the measured range. This can more easily be understood with the use of Figure 4.9, displaying lines of equal solid bridge force (Equation 4.4) as a function of temperature and time of sintering. Note that sintering time is plotted on a logarithmic scale. It can be observed that the contour lines are relatively flat with respect to time, meaning that the solid bridge force does not change significantly with time. Taking the force after 3 minutes at 600 °C as an example (starting point of the blue arrows in Figure 4.9), it would take roughly 30 more minutes to double the force and almost 7 hours to quadruple it. However, comparable forces can be obtained after the same 3 minutes of sintering at 675 and 765 °C, respectively. This means that temperature is the dominant parameter in determining the sintering force and the related defluidization behavior of a particle bed. Contact time has a much smaller influence. This is also be reflected by the force equations 4.5 and 4.6. This is in agreement with defluiza-
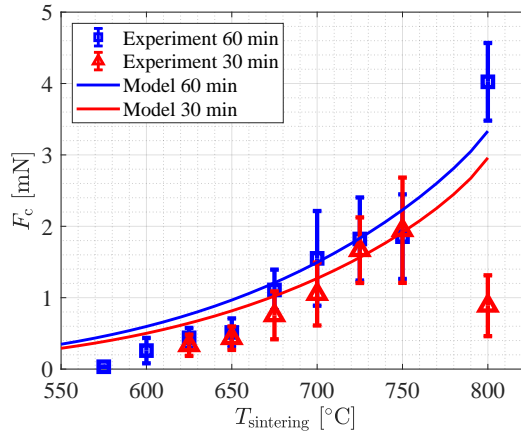
Figure 4.8: Solid bridge force between two particles sintered in nitrogen. Markers represent experimental results, while solid lines are predictions using Equations 4.4 and 4.5. Error bars correspond to the standard deviation resulting from the pellets produced by the 4 crucibles used within 1 experiment (See Figure 4.3).

tion results of combusted iron powder obtained by Liu *et al.* [99], whose experiments showed that defluidization, which is typically caused by sintering, is mainly dependent on operating temperature and could not be avoided by increasing the superficial gas velocity (and thereby lowering the contact time).

Figure 4.9 can aid in the design of exhaust systems of iron combustion reactors, where the oxygen concentration is typically low and the gas thus mainly consists of nitrogen. In parts of the exhaust system where particle-particle and particle-wall contact is extensive (such as cyclones), temperatures at which sintering can take place should be avoided.

4.3.2 Experiments under reactive conditions in hydrogen

The same experimental procedure with N_2 is used to carry out sintering experiments under reacting conditions in 10, 25 and 50 vol% H_2 atmospheres. With these experiments, we determine the effect of the reduction process on the force required to break the solid bridge between particles.

Reduction behavior

Figure 4.10 shows the reduction degree obtained during the sintering experiments with hydrogen as a function of reduction time and temperature. When using a hydrogen concentration of 10 vol%, the reduction progresses linearly with respect to time for all temperatures measured, reaching a maximum reduction degree of 53% after 60 minutes at 800 °C. This linear response in time suggests that the process is limited by
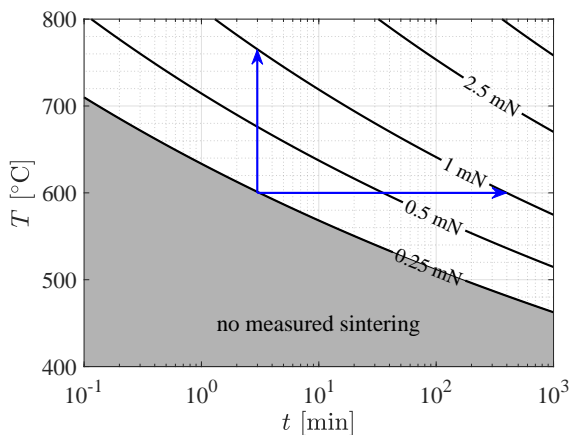
Figure 4.9: Semi-log contour plot showing the solid bridge force obtained as function of temperature and time for combusted iron powder in nitrogen. The blue arrows at 3 minutes (vertical) and 600 °C (horizontal) are used for the discussion in the text.

either external mass transport of hydrogen to the crucible or interparticle gas diffusion inside the particle bed [113].

For reduction at 25 vol% of H_2 instead, the reduction degree after 30 minutes more than doubles in comparison to the 10 vol% H_2 results over the entire temperature range (450-800 °C). This indicates that the reduction is also limited by external mass transfer or interparticle gas diffusion in this case.

However, for the two highest temperatures (700 and 800 °C), the reduction degree has no linear dependency with sintering time. From 30 to 60 minutes the reaction rate slows down significantly. Similar results were obtained with slightly smaller sized combusted powder ($d_{32} = 18.2$ vs. 53.5 μm) and occurs consistently at a reduction degree of roughly 60% (See also Chapter 3). Since the decrease of the reduction rate does not occur in the 10 vol% H_2 case, even though (1) the temperature and time are the same, and (2) the particle surfaces in both cases consist of iron, sintering can be excluded as the main cause for the decrease in reduction rate. This decrease is therefore most likely caused by the formation of intermediate species wüstite, which becomes stable above 570 °C, resulting in the reaction being controlled by nucleation and growth, confirming our earlier findings in Chapter 3.

When considering the reduction degree at 25 vol% and 50 vol% H_2, we observe that, for the high temperature cases (700 and 800 °C), the reduction degree is not dependent on the hydrogen concentration. Indeed, the reaction is limited by phase transformations (nucleation and growth) instead of mass transfer or kinetics which would scale with hydrogen concentration. Below 700 °C, the reduction degree nearly doubles by doubling the hydrogen concentration. It can therefore be concluded that reduction up to 600 °C, takes place most effectively.
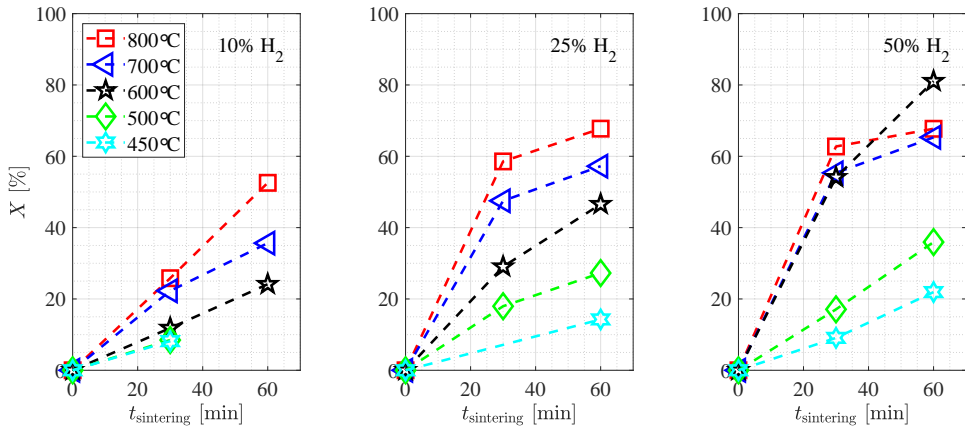
Figure 4.10: Reduction degree as a function of sintering time for three different hydrogen gas fractions: 10 vol% (left), 25 vol% (centre) and 50 vol% (right). The different colours represent different reduction temperatures.
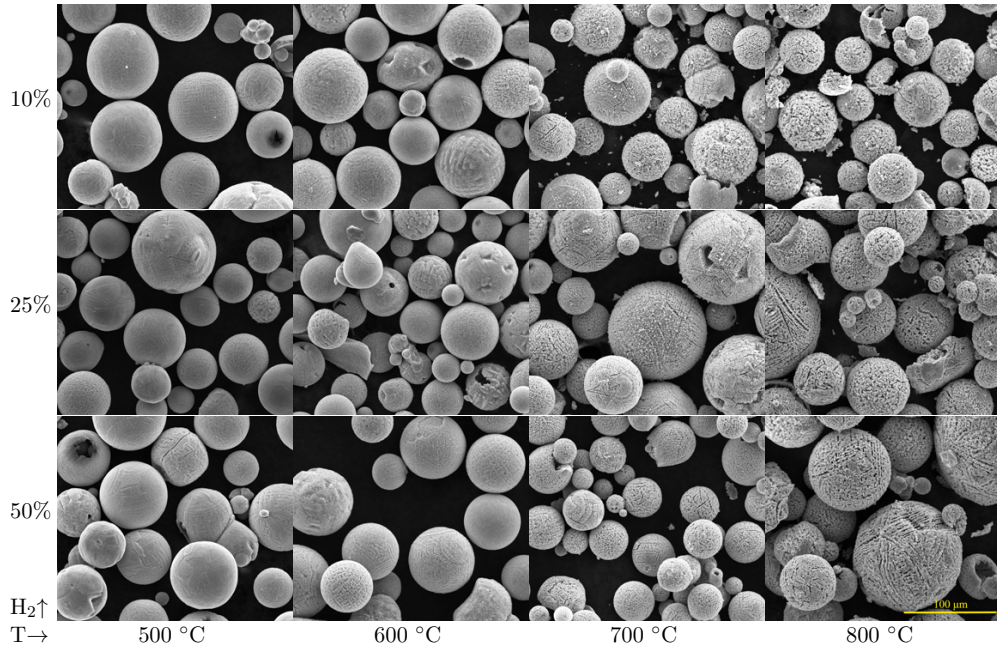
Figure 4.11: Scanning electron microscopy images of the powders after 60 minutes of isothermal reduction experiments at various temperatures and volumetric hydrogen concentrations.

(a) 700 °C   **(b)** 800 °C
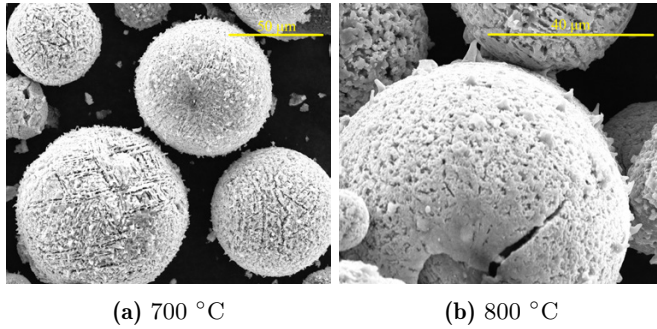
Figure 4.12: Scanning electron microscope images of the whiskers forming in 10 vol% H_2 atmospheres.

Morphology of reduced particles

Figure 10 shows images of the powder after 60 minutes of reduction at different temperatures and H_2 concentrations. The pore size increases significantly with reduction temperature. Interestingly, the powders reduced with different hydrogen concentrations but at equal temperature show the same surface morphology, even though their reduction degree is considerably different (see Figure 5.9a). This confirms that the surface of the particles quickly reduces to iron and thus the sintering mainly occurs via solid-state diffusion in iron (ferrite).

Reduction with 10 vol% hydrogen (and to a lesser extend at 25 vol%) at 700 and 800 °C, resulted in the formation of "whiskers" on the particles surfaces. Close-ups of these whiskers are provided in Figure 4.12. The presence of whiskers has been mentioned in previous works on iron ore/oxide reduction [14, 18, 96, 114, 115]. Spreitzer *et al.* [15] mention that the formation of whiskers is most dominant in cases where the nucleation/formation of iron is low, but the diffusivity is high. Indeed, in this study whiskers form mainly at low hydrogen concentrations (and thus low reduction rates) in combination with high temperature (high diffusivity). Similarly, Zhang *et al.* [103] observed that the combination of high temperature and low hydrogen flow rates in their conical fluidized bed lead to the formation of whiskers and consequently to defluidization. As can be seen in the case of 700 °C, 10 vol% H_2 in Figure 4.11, these whiskers are fragile and break off from the particle surface during handling of the powder, producing (sub-)micron-sized fines. In view of using iron powder as a transportable dense energy carrier, a significant production of these fines will lead to loss of usable material and might require additional melting and atomization processes steps to re-integrate these fines. Furthermore, the fines lead to health and safety risks if small enough to be suspended in air and/or captured by typically used cyclones. Fortunately, the formation of whiskers and thus fines, is limited to reduction at high temperature in combination with low hydrogen molar fractions and do not occur in other conditions. These conditions should therefore be avoided in reduction systems.

Close-ups of the particle surfaces reduced in 10 vol% H_2 are provided in Figure 4.13. The amount of powder used in the individual experiments ($\sim$ 1 gram) is too small for accurate measurements of properties such as specific surface area, pore size distribu-

(a) 500 °C	**(b)** 600 °C	**(c)** 700 °C	**(d)** 800 °C
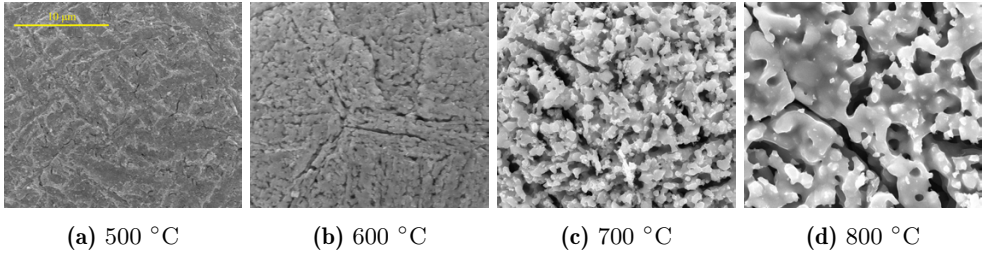
Figure 4.13: Scanning electron microscopy images of the produced surface morphology at various reduction temperatures (all at 10 vol% H_2).

tion, particle size and density. However, from the close-ups of the SEM images the pore size can be estimated to be in the nanometer range at 500 °C and in the micrometer range at 800 °C. This indicates that the specific surface area decreases with an increase of temperature. The reduction temperature therefore provides a possible mechanism to influence the ignitability of the powder, since the specific surface area is an important parameter influencing the ignition behavior of iron powder [50].

Sintering force of reduced particles

Compression tests are performed on all pellets resulting from reduction at 600 °C or higher. At 450 and 500 °C there was insignificant sintering, so no pellets are produced and thus no compression tests are carried out. From the SEM analysis we did not observe obvious differences between the powders reduced in different hydrogen concentrations. This supports the concept that surface diffusion is the main cause of sintering. When using hydrogen, the surfaces of the particles are quickly reduced to iron and their morphology is only dependent on temperature. No statistical differences were found between samples reduced at fixed temperature and time but different hydrogen concentrations. Therefore, the compression test results of samples reduced at the same combination of temperature and time, but different hydrogen concentrations, are combined to determine the solid bridge force.

Figure 4.14 displays the force required to break the neck between two particles, after reduction. The markers represent measurements from the compression tests, while the solid lines are the results of Equations 4.4 and 4.5 using the properties of iron. A neck strength σ_{sb} of 300 MPa is used in the model. This is slightly higher that the 100 MPa reported by Mikami *et al.* [93], but matches well with values for the tensile strength of commercially available pure iron (250-300 MPa) [116]. The solid bridge forces for samples reduced with hydrogen are smaller than those sintered in nitrogen, even though the strength of the neck (σ_{sb}) is higher. This is due to the lower solid state diffusivity of iron atoms in ferrite/iron compared to magnetite (see Table 4.2). Therefore the neck growth is slower when reduction occurs, which leads to a smaller contact area between particles over which the applied force is distributed.

Figure 4.15 shows the contour graph of the solid bridge force for reduced powder, using the sintering model in combination with the neck strength mentioned above. The graph can be used in future research to estimate the defluidization behavior of combusted
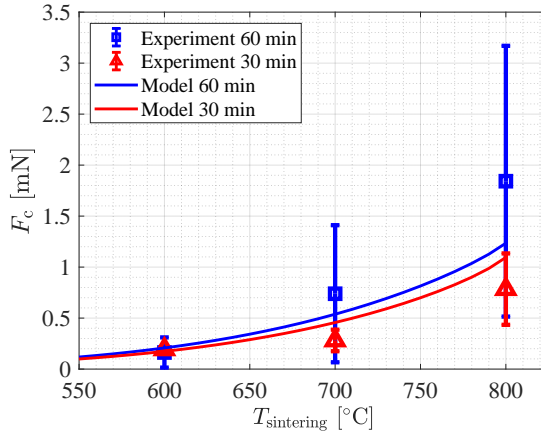
Figure 4.14: Solid bridge force between two particles for sintering with hydrogen. Markers represent experimental results, while solid lines are from the model (Equation 4.4). Error bars represent the standard deviation determined from the pellets produced at different hydrogen concentrations.
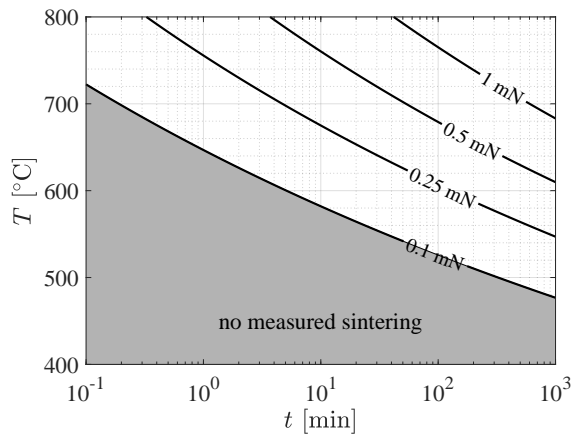
Figure 4.15: Contour plot showing the solid bridge force obtained as function of temperature and time for reduced iron powder sintering in hydrogen.

iron powder undergoing reduction based on the contact forces in combination with the contact time between particles in the bed. More research using larger amount of powders is recommended to provide quantitative information on the pore morphology, iron content, and densification in the later stages of sintering.

4.4 Conclusions

The sintering behavior of combusted iron powder is studied in a packed bed reactor in various N_2 and H_2 atmospheres and at temperatures between 400 and 800 °C. The solid bridge force is measured through compression tests of the sintered pellets.

Sintering occurs in nitrogen at temperatures starting from 575 °C and increases exponentially with temperature. The influence of the contact time is much smaller than that of temperature, indicating that shorter contact times are not that effective in the prevention of sticking.

In the case of hydrogen, sintering occurs from 600 °C onwards. The sintering forces in the produced pellets are smaller than in the case of nitrogen, mainly due to the lower solid-state diffusion giving a slower neck growth. Sintering is found not to be the main cause for the decrease in reduction rate at high temperature. The decrease is rather caused by the formation of wüstite as an intermediate species in the reduction process.

Iron whiskers form during the reduction process of the powders at low H_2 concentrations ($\leq$ 25 vol%) in combination with a high mobility/diffusivity of iron ($\geq$ 700 °C), producing (sub-)micron sized fines.

The obtained results can be used to predict the sintering behavior of combusted iron powder at elevated temperature and aid in the design of components for the metal energy carrier cycle as well as for direct reduction of iron ores (green steelmaking).

5 Fluidization

The setup and some of the results presented in this chapter are the result of the master theses of Nicole Stevens and Daniël Lelivelt [117, 118]. Parts of this chapter are published in: C.J.M. Hessels et al. Fuel, 342 (2023) 127710. Background image: photograph of combusted iron powder fluidized using nitrogen. Image courtesy of B. van Overbeeke.

Abstract

The fluidization and reduction behavior of micron-sized iron oxide powder, produced by iron combustion, is studied in a lab-scale cylindrical fluidized bed. The minimum fluidization velocity u_{mf} is found to stabilize above normalized static bed heights of 0.5 H/D (static bed height divided by the bed diameter). u_{mf} is measured as a function of temperature between 280 and 860 K for both H_2 and N_2 as fluidizing gas. The results start to deviate from the Ergun correlation at temperatures above 560 K, both for N_2 and H_2. A new correlation, taking the cohesive inter-particle solid bridge force into account, is proposed in this work to predict the minimum fluidization velocity at high temperatures. Reduction experiments are carried out for a total time of 5 hours at constant excess velocity with 50, 75 and 100 vol% of H_2 and temperatures between 623 and 823 K. Gradual defluidization occurs when the operating temperature exceeds 800 K. A maximum reduction degree of 61% is obtained at 807 K and 100 vol% H_2.

5

5.1 Introduction

In Chapters 3 and 4, the intrinsic chemical kinetics and sintering behavior of combusted iron powder with hydrogen is investigated using thermogravimetric analysis and a packed bed reactor, respectively. However, for larger quantities of powder, a fluidized bed is preferred over a packed bed reactor due to greater heat and mass transfer rates.

Fluidization of micron-sized iron(-oxide) powder at high temperature has, however, proven to be difficult due to the cohesiveness of this material [17, 18, 85, 88, 97, 119, 120]. Zhong *et al.* [121–123] studied the fluidization behavior of iron and iron-oxide powders with different fluidizing gases. They observed sticking in beds with pure iron as well as in beds of iron oxide with both nitrogen and hydrogen as fluidizing gas. This sticking resulted in an increase in the minimum fluidization velocity at elevated temperatures. Secondly, they were able to determine a defluidization temperature of the bed. For nitrogen this temperature was around 923 K, while for hydrogen defluidization already occurred around 673 K. However, most of their experiments were performed using a non-isothermal method (fixed heating rate), which is different from typical industrial reactors (fixed temperature). They also used a relatively small fluidized bed reactor made of silica, and the possible effect of electrostatic forces was not considered. Mikami *et al.* [93] studied the mechanism of defluidization, concluding that it was due to particle-to-particle neck growth. They observed that the sticking started to affect the fluidization behavior from 773 K. However, they performed minimum fluidization experiments at room temperature after 1 hour of fixed bed heat treatment (sintering) which might overpredict the influence of sintering in a real fluidized bed (where particles are in constant motion). They also used pre-reduced solid steel shot particles, which are different from combusted iron. Spreitzer and Schenk [69, 124] investigated the fluidization and reduction behavior of different iron ores in the temperature range of 873-1073 K. They observed that fluidization was possible up to 1073 K, depending on the specific ore composition. They limited their particle

size range to 250-500 µm, significantly larger than those used in the metal fuel cycle (10-100 µm). Thus, the cohesiveness of iron/iron-oxide powder with increasing temperature poses a significant challenge in the design of the fluidization process for iron fuel regeneration.

The minimum fluidization velocity u_{mf} is one of the most important fundamental parameters in the analysis, characterization and design of fluidized beds [125]. It determines the gas velocity above which fluidization starts to occur, and in combination with the excess velocity ($u_{\mathrm{e}} = u_0 - u_{\mathrm{mf}}$, with u_0 the superficial gas velocity), appears in most correlations describing the fluidization state. Many expressions exist for predicting u_{mf}, mainly based on the equation derived by Ergun [126]. However, it is also known that these correlations do not match experimental results both at high temperature as well as for small (Geldart C) particles [121, 127, 128]. The cause of this is often attributed to cohesive forces, which are not taken into account in the Ergun equation. Since the minimum fluidization velocity and the related excess velocity determine properties such as solid mixing, bubble size and voidage, they also (in combination with the intrinsic chemical kinetics) determine the conversion that can be obtained in fluidized bed reactors. This also means that experiments trying to understand chemical reactions by varying gas composition and temperature, should optimally try to keep the excess velocity the same at different operating conditions. This can only be done with an accurate prediction of u_{mf}.

Therefore, in this work, u_{mf} of combusted iron powder is measured experimentally in a lab-scale cylindrical fluidized bed. In Section 5.2, the experimental setup and procedure are explained. The derivation of a new correlation for u_{mf} at high temperature is also given, which incorporates the cohesive solid bridge force into the Ergun equation. In Section 5.3, the effect of static bed height, temperature and fluidizing gas composition on the minimum fluidization velocity is studied and results are compared with the Ergun equation and the correlation derived in Section 5.2. Section 5.4 presents the results of the reduction experiments conducted at constant excess velocity. Finally, in Section 5.5, conclusions are summarized.

5.2 Materials and methods

5.2.1 Materials

The powder used for this research is the product of high-purity iron powder (Rio Tinto ATOMET95), combusted with air in a pilot scale industrial burner. In this combustion process the particles are dispersed in air and injected into the burner. A non-premixed propane pilot flame is used to stabilize the flame. The combusted particles are captured in a long horizontal cooling section, followed by a cyclone. Powder (Pometon MT63) combusted using the same burner has been studied in great detail by Choisez *et al.* [21], who analyzed the microstructure of the combusted powder in order to better understand the combustion process. They found their powder to be mostly spherical, consisting of a mixture of magnetite and hematite. The powder used in this study is recovered from the cooling section of the burner. It is characterized using scanning electron microscopy (SEM), particle size analysis (PSA) and X-ray diffrac-
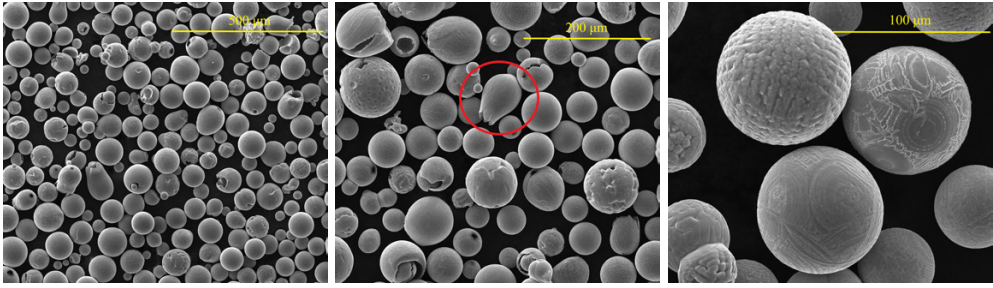
Figure 5.1: Scanning electron microscope (SEM) images of the iron oxide powder. The red circle in the center image marks an example of a tulip shaped particle.

tion (XRD). To remove ultra-fine particles and large agglomerates for the fluidization experiments, the powder is first sieved between 32 and 100 μm, using a RETSCH AS 200 vibratory sieve shaker and LINKER woven wire mesh sieves. The sieving resulted in 15 wt% of the initial combusted powder to be removed. Figure 5.1 shows SEM images (FEI ESEM Quanta 600 FEG, 30kV, 3.0 spot size) of the sieved powder. The combusted particles are mainly spherical, but some of them are tulip shaped hollow shells, resulting from micro-explosions (see center image in Figure 5.1 for an example), as already observed in previous studies [21, 31–33, 52]. The particles show different surface roughnesses, most likely resulting from different combustion profiles. The bulk density of the powder is determined using a measuring cylinder to be 2912 kg/m^3, resulting in a particle density of 4601 ± 58 kg/m^3, assuming close random packing. The solid density, measured using a pycnometer (AccuPyc II 1340 V3.00), is 5267.4 kg/m^3. XRD analysis (Brukes D8 Advance A25-X1, Co target, 35 kV) suggests a composition of 60 wt% magnetite (Fe_3O_4) and 33 wt% hematite (Fe_2O_3) and 7 wt% iron. Figure 5.2 shows the (volume-based) particle size distribution and circularity data measured by dynamic image analysis (Bettersizer S3 Plus). The particles have a Sauter mean diameter d_{32} of 56.63 μm and are highly spherical. The Sauter mean diameter is used as the effective particle size in the minimum fluidization velocity correlations as it gives the same surface area for the same total bed volume [125].

The hydrogen and nitrogen gases used are provided by Linde Gas Benelux and have a purity of N5.0.

5.2.2 Fluidized bed reactor

The experiments are conducted in a 3D fluidized bed designed during the graduation project of Nicole Stevens [117]. The reactor is made of stainless steel (type 316) with an inner diameter of 80.9 mm and a height (above distributor) of 750 mm. Figure 5.3 shows a schematic and photograph of the setup. A three-zone tubular furnace (Carbolite GZF 12/-/546) is used to heat up the fluidized bed and preheat the inlet gas. Three thermocouples are used to control each zone and one central thermocouple is inserted into the bed from above (TC Direct, type N). The central thermocouple is placed 45 mm above the distributor plate. The pressure drop over the bed (including the distributor plate) is measured using a differential pressure transmitter (Nöding PD40,
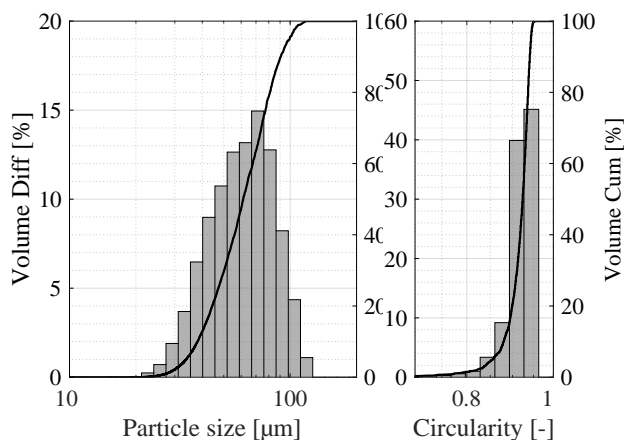
Figure 5.2: Particle size (left) and circularity (right) of combusted iron powder, measured using dynamic image analysis (DIA). The bars correspond to the left axes, while the solid lines corresponds to the right axes.
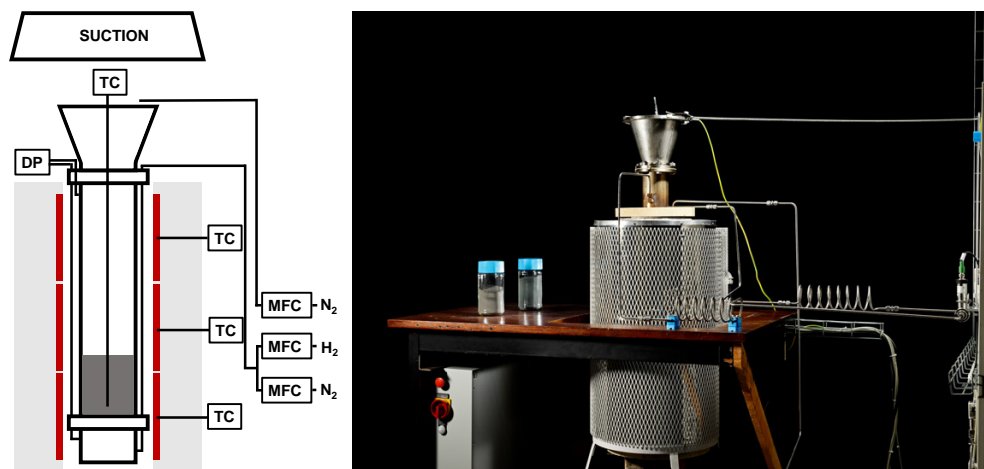
Figure 5.3: Schematic and photograph of the lab-scale high temperature fluidized bed reactor setup. DP = differential pressure transmitter, TC = thermocouple, MFC = mass flow controller. Photograph courtesy of B. van Overbeeke.

0-400 mbar). The gas flows are set using mass flow controllers (Bronkhorst EL-Flow F201-CV/AV), where a mixture of hydrogen and nitrogen can be used as fluidizing gas. A second independent nitrogen supply is used to dilute the effluent gas to below the lower explosion limit of hydrogen. The distributor plate consists of a quartz fiber membrane filter (Merck Millipore AQFA09050) sandwiched between two perforated stainless steel plates (807 orifices, 1.5 mm orifice diameter with triangular pitch). The acquisition frequency of the system is 1 Hz.

5.2.3 Experimental procedure

Before each experiment the sieved powder is inserted in the cold reactor. The filled bed is then fluidized to break down any internal structure, such as residual clusters and stratification. u_{mf} is determined at room temperature using nitrogen by incrementally increasing the superficial gas velocity until the pressure drop stays constant, and subsequently decreased back to zero. The reactor is then heated up (6 K/min) to the desired bed temperature while the powder is fluidized using nitrogen. After the desired temperature is reached, a similar u_{mf} experiment (as explained above for room temperature) is carried out using the desired fluidizing gas composition (H_2:N_2). After the experiments are performed the reactor is allowed to cool down naturally. Nitrogen is again provided as fluidizing gas. The quartz fiber membrane filter is replaced after each experiment.

For the reduction experiments, the powder is inserted in the cold reactor and is subsequently heated under fluidizing conditions. When the desired temperature is reached, the hydrogen and nitrogen gas flow rates are set in order to reach the desired excess gas velocity and composition. After 5 hours the gas flow is switched back to nitrogen and the reactor is allowed to cool down naturally under fluidizing conditions. The powder is weighed before and afterwards using a digital scale (Mettler Toledo PG5002-S).

5.2.4 Data analysis method

The minimum fluidization velocity is determined in the standard fashion by the crossing point of straight lines fitted to the static regime and the fluidized regime using a decreasing gas velocity method. The static regime is fitted with a linear line with a free origin ($\Delta p = a \cdot u_0 + b$) to account for sensor hysteresis/offset, while a horizontal line ($\Delta p = c$) is used to fit the fluidized regime. A typical graph of the pressure drop versus the superficial gas velocity and the determination of u_{mf} is shown in Figure 5.4. The pressure drop Δp is normalized using the hydrostatic bed pressure:

$$\Delta p_{\mathrm{n}} = \frac{\Delta p A}{mg} \tag{5.1}$$

with A the cross sectional area of the reactor, m the powder bed mass and g the gravitational constant. The reason that the bed in fluidized state does not reach the hydrostatic pressure is most likely caused by the dead zone above the distributor plate (between the holes and in the wall-distributor plate edge).

The static bed height H is calculated using the particle density mentioned in Section 5.2.1 and a void fraction $\varepsilon_{\mathrm{mf}}$ of 0.4. This static bed height is subsequently normalized to the bed diameter D. The pressure drop over the distributor plate, measured using an empty bed, is subtracted from the measurement data.

The reduction degree X is calculated by dividing the mass loss obtained during a reduction experiment by the theoretical mass loss, based on a full conversion of the initial powder to 100 wt% iron:

$$X = \frac{\Delta m_{\mathrm{experiment}}}{\Delta m_{\mathrm{theory}}} \tag{5.2}$$
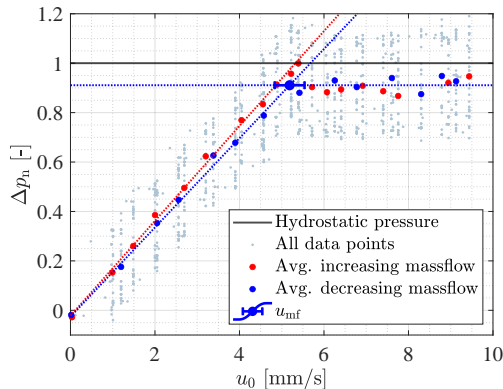
Figure 5.4: Typical graph showing normalized pressure drop over superficial gas velocity. Error bars on the u_{mf} display a 95% confidence interval.

5.2.5 High temperature fluidization model

Traditionally, u_{mf} can be determined from empirical correlations, e.g., the Ergun equation [126], by matching the pressure drop of a gas through a packed bed (of height H) with the buoyant weight of the particle bed:

$$\left(\frac{\Delta p}{H}\right)_{\mathrm{drag}} = \left(\frac{mg}{AH}\right)_{\mathrm{weight}} \tag{5.3}$$

$$\left(\frac{\Delta p}{H}\right)_{\mathrm{drag}} = \frac{150\left(1-\varepsilon_{\mathrm{mf}}\right)^2}{\varepsilon_{\mathrm{mf}}^3}\frac{\eta_{\mathrm{g}}u_{\mathrm{mf}}}{d_{32}^2} + \frac{1.75(1-\varepsilon_{\mathrm{mf}})}{\varepsilon_{\mathrm{mf}}^3}\frac{\rho_{\mathrm{g}}u_{\mathrm{mf}}^2}{d_{32}} \tag{5.4}$$

$$\left(\frac{mg}{AH}\right)_{\mathrm{weight}} = (1-\varepsilon_{\mathrm{mf}})\cdot(\rho_{\mathrm{s}}-\rho_{\mathrm{g}})\cdot g \tag{5.5}$$

in which $\varepsilon_{\mathrm{mf}}$ is the bed void fraction at minimum fluidization, η_{g} is the dynamic viscosity of the gas mixture, d_{32} the Sauter mean diameter of the powder, ρ_{g} the density of the gas mixture, ρ_{s} the density of the solid and g the gravitational acceleration.

Xu and Zhu [127] suggested an improved balance for cohesive particles by incorporating inter-particle forces in the packed bed force balance:

$$\left(\frac{\Delta p}{H}\right)_{\mathrm{drag}} = \left(\frac{mg}{AH}\right)_{\mathrm{weight}} + \left(\frac{\sigma}{H}\right)_{\mathrm{cohesion}} \tag{5.6}$$

in which the third term is due to the tensile stress of the particle bed, following the expression by Rumpf [104]:

$$\left(\frac{\sigma}{H}\right)_{\mathrm{cohesion}} = \frac{1-\varepsilon_{\mathrm{mf}}}{\varepsilon_{\mathrm{mf}}}\frac{F_{\mathrm{c}}}{d_{32}^2}\frac{1}{H} \tag{5.7}$$

where F_{c} is the sum of all inter-particle cohesive forces acting between two particles in a bed. Multiple different interparticle forces can exist during fluidization [129]. In the case of metallic particles at high temperature, the dominant cohesive force is the

formation of a solid bridge via the surface diffusion mechanism [95, 105]. We can use the equation derived by Kuczynski [92] to calculate the solid bridge force between two particles:

$$F_c = \pi x^2 \sigma_{sb} \tag{5.8}$$

$$x = \left(\frac{56\gamma\delta^4}{kT} D_s a^3 t_c \right)^{\frac{1}{7}} \tag{5.9}$$

in which σ_{sb} is the tensile strength of the neck (with radius x), γ is the surface free energy, δ is the lattice spacing, k is the Boltzmann constant, T the temperature, a is the curvature radius of the particle (which is $\frac{1}{2}d_{32}$ for smooth particles) and t_c is the contact time. D_s is the solid state surface self-diffusion coefficient of the material, which can often be described using an Arrhenius expression:

$$D_s = D_{0,s} \exp\left(-\frac{E_a}{RT}\right) \tag{5.10}$$

in which $D_{0,s}$ is the frequency factor, E_a the activation energy and R the universal gas constant.

The contact time during fluidization is related to the particle size and the characteristic velocity ($\approx u_{mf}$) [97]:

$$t_c = \frac{d_{32}}{v} = \frac{d_{32}}{\xi\sqrt{u_0 u_{mf}}} = \frac{d_{32}}{\xi\sqrt{u_{mf}^2}} = \frac{d_{32}}{\xi u_{mf}} \tag{5.11}$$

in which ξ is a factor, between 0 and 1. Values of 0.1 and 0.15 have been used by other researchers [97, 130].

The gas viscosity η_g of a mixture of hydrogen and nitrogen is determined using the equation derived by Wilke [131]:

$$\eta_g = \Sigma_{i=1}^N \frac{\eta_{g,i}}{1 + \frac{1}{\chi_i}\Sigma_{j=1, j\neq i}^N \chi_j \psi_{ij}} \tag{5.12}$$

with

$$\psi_{ij} = \frac{\left(1 + \left(\frac{\eta_{g,i}}{\eta_{g,j}}\right)^{\frac{1}{2}} \left(\frac{M_j}{M_i}\right)^{\frac{1}{4}}\right)^2}{2^{\frac{3}{2}} \left(1 + \frac{M_i}{M_j}\right)^{\frac{1}{2}}} \tag{5.13}$$

with χ_i is the molar fraction, M_i the molar mass, $\eta_{g,i}$ the dynamic viscosity of a pure component.

The density of a gas mixture is:

$$\rho_g = \Sigma_{i=1}^N x_i \rho_{g,i} \tag{5.14}$$

The density and viscosity of pure hydrogen and nitrogen gas at different temperatures are determined using NIST polynomials [132]:

Table 5.1: Properties used in minimum fluidization model.

Parameter	Value	Source
Surface free energy, γ	1.44 N/m	[108]
Curvature radius, a	$\frac{1}{2}d_{32}$	[94]
Frequency factor, $D_{0,\mathrm{s}}$	$5.2 \cdot 10^{-4}$ m^2/s	[110]
Activation energy, E_a	230 kJ/mol	[110]
Empirical factor, ξ	0.1 - 1	
Void fraction, ε_mf	0.4	
Particle density, ρ_s	4601 kg/m^3	
Sauter mean diameter, d_{32}	56.63 μm	
Gravitational constant, g	9.81 m/s^2	
Boltzmann constant, k	$1.381 \cdot 10^{-23}$ J/K	
Universal gas constant, R	8.314 J/(mol K)	

$$\rho_{\mathrm{g,H_2}} = 24.53724 \cdot T^{-1} \text{ kg/m}^3 \tag{5.15}$$

$$
\begin{aligned}
\eta_{\mathrm{g,H_2}} = {} & 1.678903 \cdot 10^{-6} + 2.78703 \cdot 10^{-8} \cdot T \\
& -1.617117 \cdot 10^{-11} \cdot T^2 + 9.132361 \cdot 10^{-15} \cdot T^3 \\
& -2.172766 \cdot 10^{-18} \cdot T^4 \text{ Pa} \cdot \text{s}
\end{aligned}
\tag{5.16}
$$

$$\rho_{\mathrm{g,N_2}} = 341.3592 \cdot T^{-1} \text{ kg/m}^3 \tag{5.17}$$

$$
\begin{aligned}
\eta_{\mathrm{g,N_2}} = {} & 2.219433 \cdot 10^{-6} + 6.073737 \cdot 10^{-8} \cdot T \\
& -3.194531 \cdot 10^{-11} \cdot T^2 + 1.229863 \cdot 10^{-14} \cdot T^3 \\
& -1.799528 \cdot 10^{-18} \cdot T^4 \text{ Pa} \cdot \text{s}
\end{aligned}
\tag{5.18}
$$

Although the density change has a negligible effect on the calculation of u_mf compared to the viscosity change for the powder size used, both are included in the analysis for completeness.

For material properties, values for magnetite Fe_3O_4 are used, since (1) the particles mainly consist of magnetite, and (2) the solid state diffusivity of iron in hematite is known to be much lower than in magnetite [61]. Therefore it can reasonably be assumed that the magnetite phase is the main cause of sintering.

For the lattice spacing δ of magnetite, we can use the correlation from Gorton *et al.* [107]:

$$\delta = 8.3939 + 8.46 \cdot 10^{-5}T + 5.52 \cdot 10^{-8}T^2 \text{ Å} \tag{5.19}$$

Literature on the tensile strength of magnetite is limited, especially at elevated temperature. Therefore, an estimate is made based on the results obtained by Hidaka *et al.* [133], by fitting a line through their data:

$$\sigma_\mathrm{sb} = -0.0628T + 73.425 \text{ MPa} \tag{5.20}$$

For the bed voidage at minimum fluidization ε_mf a constant value of 0.4 is assumed, which is estimated based on the minimum fluidization velocity at room temperature. It also matches the voidage for dense packing of spherical particles. Although some

correlations exist for the change of bed voidage with temperature, the results are inconclusive and material dependent [125]. Furthermore, although $\varepsilon_{\mathrm{mf}}$ is present in the cohesive term (via Equation 5.11), the influence of the voidage on u_{mf} still decreases with temperature (when the cohesive term becomes important).

A summary of all other properties used can be found in Table 5.1.

Due to the fact that u_{mf} is present in the cohesive term (Equation 5.11), no trivial explicit form for u_{mf} exists and Equation 5.6 is therefore solved numerically.

5.3 Minimum fluidization velocity

5.3.1 Influence of bed height

Figure 5.5 shows u_{mf} as a function of static bed height, determined at room temperature using nitrogen. It can be observed that u_{mf} is mostly independent of bed height, which is in agreement with Equation 5.3. However, at low static bed height, u_{mf} seems to be slightly underestimated. The reason for this might be that shallow bed effects, such as channeling, occur. There also seems to be more variation between experiments at low static bed heights, which might indicate slight variations in the mean particle size between batches. The larger error bars at low H/D are due to the higher uncertainty on the linear slope for the static regime. Due to the availability of combusted powder and the hydrogen usage, lower bed heights are preferred, while still avoiding shallow bed effects. Therefore, for the u_{mf} measurements at high temperature as well as the reduction experiments reported later in this chapter, a bed height of $H/D \approx$ 0.65 (750 gram, $\varepsilon_{\mathrm{mf}} = 0.4$) is used.
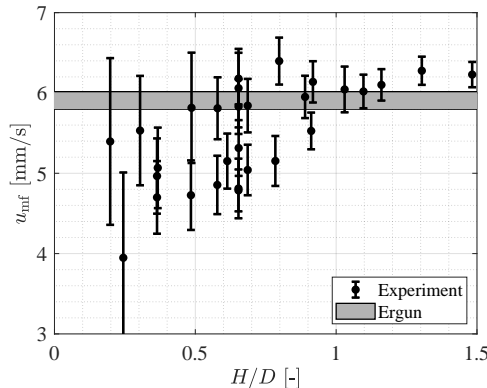
Figure 5.5: Minimum fluidization velocity u_{mf} for different normalized static bed heights, determined at room temperature using nitrogen. The error bars on the experiment are 95% confidence interval. The grey area defines the range of u_{mf}, according to Ergun (Equation 5.3), due to variation in ambient temperature between the experiments.
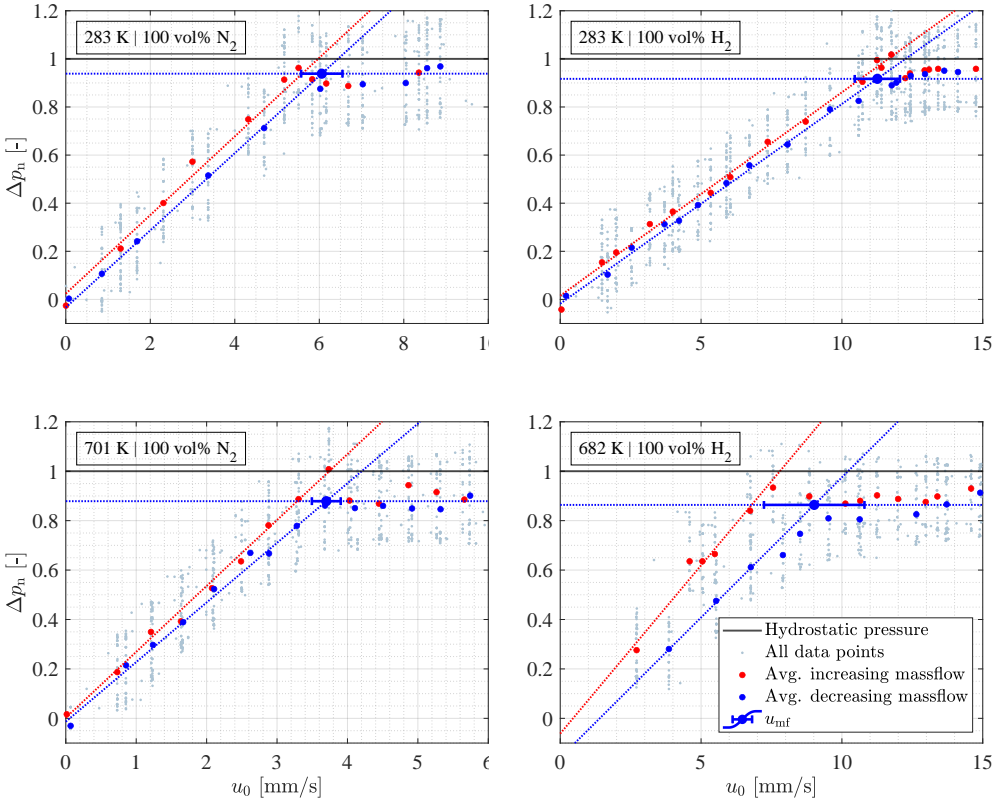
Figure 5.6: Normalized pressure drop over superficial gas velocity for N_2 and H_2 at low and high temperature.

5.3.2 Influence of temperature and gas composition

Figure 5.6 shows examples of Δp_n vs. u_0 graphs of nitrogen and hydrogen around 300 and 700 K. It can be observed that a higher temperature leads to a steeper slope of the pressure drop, when increasing the gas flow from zero to above the minimum fluidization velocity ($u_{mf,increasing}$). This is attributed to the increasing cohesiveness of the powder with increasing temperature. Similar effects are observable for small, cohesive particles (Geldart C) [134].

Figure 5.7 compares the experimental results of u_{mf} with the predictions using the Ergun correlation (Equation 5.3) and the new correlation (Equation 5.6) which considers the solid bridge force (Equation 5.8).

From the experimental results we can observe that with increasing temperature, the minimum fluidization velocity initially decreases, due to the changes in viscosity of the gas. However, from a temperature of 560 K onward (marked by the dotted black line in Figure 5.7), the minimum fluidization velocity actually increases with temperature. Similar observations were also reported by Zhong *et al.* [121] from experiments using slightly larger iron powder (74-149 µm). We can see that the Ergun correlation,
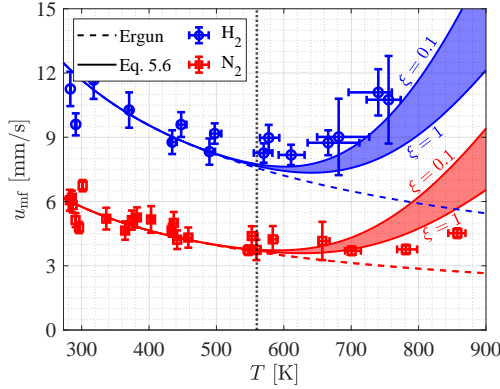
Figure 5.7: Minimum fluidization velocity as function of temperature for N_2 and H_2. Vertical error bars show 95% confidence intervals, while horizontal error bars represent the temperature span that occurred during each experiment. The colored areas are the results of using different values for ξ in Equation 5.11.

using a void fraction of 0.4, accurately predicts the minimum fluidization velocity of both pure nitrogen and pure hydrogen at temperatures up to 560 K. However, above this value, the Ergun correlation fails to predict the experiments. However, the new correlation, which takes into account the cohesive solid bridge force, does match the experimental results quite well. It should be noted that, due to the relatively large bed mass (750 grams of iron oxide powder) and the relatively low H_2 gas flow rate, far less than 1% conversion is expected to occur within one minimum fluidization experiment. Therefore, the prediction using magnetite instead of iron as material in Equation 5.9, is still valid.

Using this new predictive model for the minimum fluidization velocity (Equation 5.6), it is possible to perform experiments at equal excess velocities, and therefore at equal fluidization behavior, by using:

$$u_e(T) = u_0(T) - u_{mf}(T) \tag{5.21}$$

In the following section, results of reduction experiments at equal excess velocity are presented.

5.4 Reduction behavior

Isothermal reduction experiments are carried out between 623 and 823 K, with hydrogen concentrations of 50, 75 and 100 vol% H_2. All reduction experiments are performed at an excess velocity u_e of 26 mm/s, equaling superficial gas velocities in the range of $u_{0,N_2}(T) = $ 5-9 $u_{mf,N_2}(T)$ and $u_{0,H_2}(T) = $ 3-5 $u_{mf,H_2}(T)$. The total reduction time of each experiment was set to 5 hours.
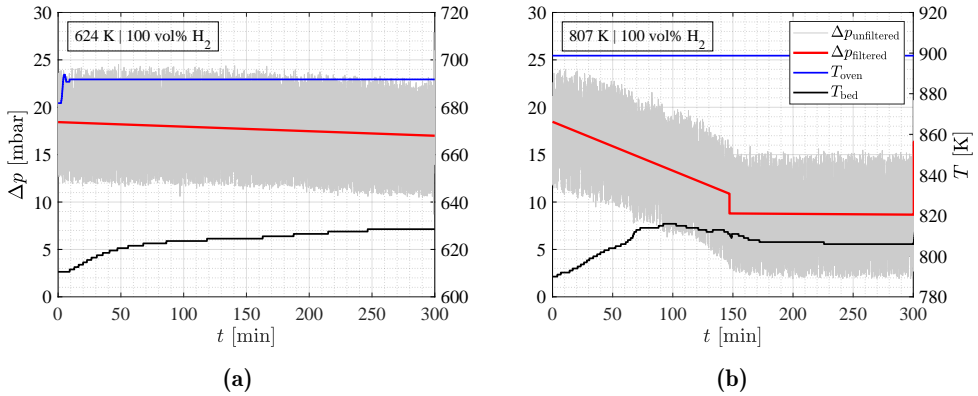
Figure 5.8: Examples of the two types of pressure drop and temperature profiles occurring during the reduction experiments.

5.4.1 Fluidization behavior

Two different types of fluidization behavior occured during the experiments. Examples of the pressure drop and temperature profiles of the two types are displayed in Figure 5.8. The filtered signal (red line) is produced using the 'ischange'-algorithm in MATLAB and is meant as a visual aid only. At temperatures below 800 K (Figure 5.8a), the bed stays fluidized during the entire 5 hours, with only a minor decrease of the pressure drop due to the reduction process (decrease in particle density). At the experiments performed above 800 K, independently of the hydrogen concentration, defluidization occurs. Figure 5.8b shows that the pressure drop steadily decreases until the bed is completely defluidized at t ≈ 150 min. The remaining pressure drop is due to the resistance of the agglomerated bed. This type of defluidization matches with the classification of "gradual defluidization" described by Lei *et al.* [97]. They visually observed an agglomerate forming at the distributor plate which subsequently grew upwards. In their case the gradual defluidization occurred at relatively low superficial gas velocities and bed temperatures between 923 and 1023 K. The higher temperature at which gradual agglomeration occurred, compared to the one found in this work (823 K), might be caused by the larger particles they used (106-150 μm versus 32-100 μm in this work).

The reason that defluidization occurs, even though the superficial gas velocity was above the predicted minimum fluidization velocity, is due to particles sintering to the wall of the reactor and in the dead zone just above the distributor plate, where the local gas velocity is known to be much lower than the minimum fluidization velocity [93, 97]. In these locations the contact times between particles are significantly longer than calculated by Equation 5.11, leading to sintering.
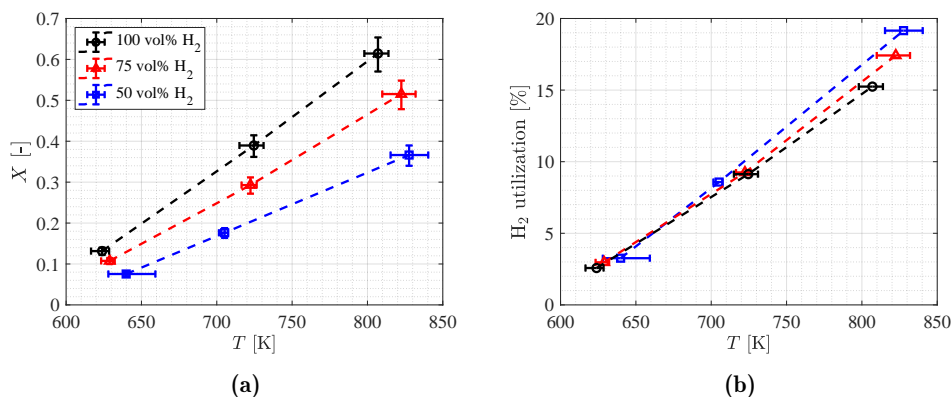
Figure 5.9: (a) reduction degree and (b) H_2 utilization as a function of temperature, obtained after 5 hour reduction experiments. Horizontal error bars represent the temperature span, while vertical error bars are due to the error on the initial composition.

5.4.2 Reduction degree

Figure 5.9a illustrates the reduction degree obtained after 5 hours at various temperatures and hydrogen concentrations, calculated using Equation 5.2. It can be observed that the reduction degree increases both linearly with temperature. Interestingly, the highest reduction for all three hydrogen concentrations is obtained at the experiments above 800 K, even though defluidization of the bed occurs. The highest reduction degree of 61% is reached at a temperature of 807 K and a hydrogen concentration of 100 vol%. Qualitative X-ray diffraction indicated that all reduced powders consisted of a ratio of magnetite and iron. Figure 5.9b displays the H_2 utilization, defined as the amount of H_2 used for the reduction divided by the total amount of H_2 supplied. The utilization degree increases linearly with reduction temperature and is nearly independent of hydrogen concentration, indicating that reduction degree is linearly dependent on the hydrogen concentration. The small difference above 800 K is most likely caused by differences in defluidization time, which are slightly shorter at higher hydrogen concentrations.

5.4.3 Morphological observations

Figures 5.10 and 5.11 show SEM images of the powder after reduction. Figure 5.10 shows the effect of gradual defluidization on the powder. Only images for reduction at 75 vol% H_2 are shown, since the effect of hydrogen concentration on the agglomeration was negligible. Images for the other cases can be found in Figure 5.12. We can clearly see that at 823 K the powder consists mainly of agglomerates, while at 722 K hardly any agglomerates are formed. This difference in powder morphology matches the pressure drop profiles in Figure 5.8. Above 800 K gradual defluidization occurs, caused by this agglomeration. Below 800 K the decrease in pressure drop was solely caused by the reduction process.

Figure 5.11 shows a close-up of a particle after reduction. A dendritic iron structure can be observed, leading to a particle surface which is highly porous. This agrees with with results obtained in previous studies on iron oxide reduction [76, 83, 135]. Only the results at 807 K and 100 vol% H_2 are shown here, while the images of the other cases are provided in Figure 5.13. Interestingly, the difference in surface morphology between the particles reduced above 700 K was negligible, even though the reduction degree obtained varied significantly ($X = 0.2 - 0.6$). This matches with the kinetic result obtained in a previous study, which indicated that the reaction progresses via a shrinking core principle (phase boundary controlled), where the conversion of iron oxide to iron starts at the surface and grows inwards, creating an oxide core with an iron shell surrounding it (see also Chapter 3).

(a) 722 K & 75 vol% H_2, $X = 0.29$ **(b)** 823 K & 75 vol% H_2, $X = 0.52$
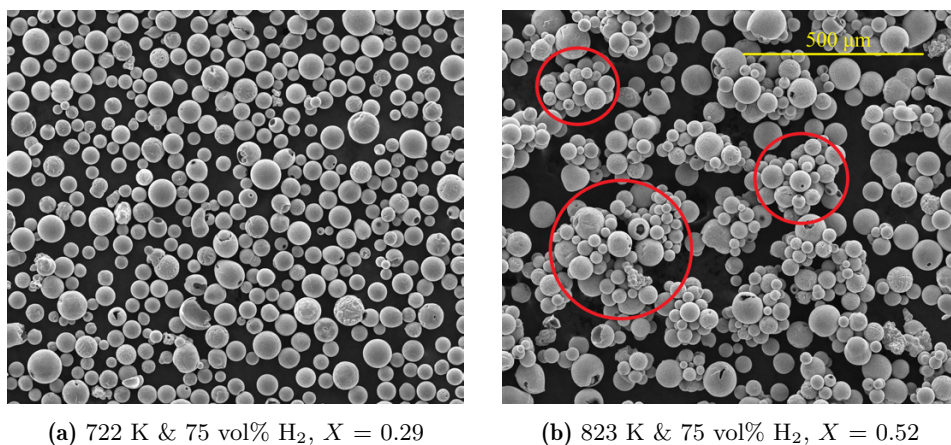
Figure 5.10: SEM images of the powder after reduction experiments showing agglomeration.

(a) 1000x magnification   **(b)** 5000x magnification
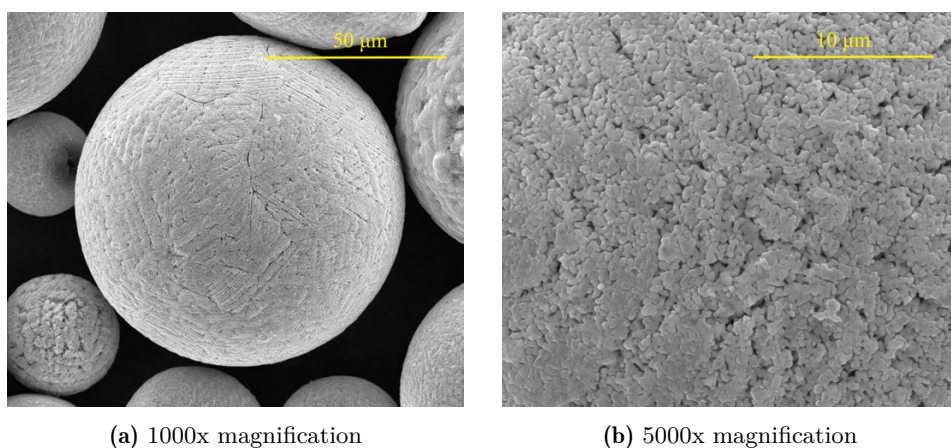
Figure 5.11: SEM images of the partially reduced powder ($X = 0.61$). Reduced at 807 K & 100 vol% H_2.

Trial combustion experiments are carried using powder from this fluidized bed, indicating that the produced powder can be combusted and has some advantages compared to commercially available powder. Details about these combustion experiments are given Appendix A.3.

(a) 640 K & 50 vol% H_2, $X = 0.08$

(b) 629 K & 75 vol% H_2, $X = 0.11$

(c) 624 K, 100 vol% H_2, $X = 0.13$

(d) 705 K & 50 vol% H_2, $X = 0.18$

(e) 722 K & 75 vol% H_2, $X = 0.29$

(f) 725 K, 100 vol% H_2, $X = 0.39$

(g) 828 K, 50 vol% H_2, $X = 0.37$

(h) 822 K, 75 vol% H_2, $X = 0.52$

(i) 807 K, 100 vol% H_2, $X = 0.61$

Figure 5.12: Scanning electron microscopy images of the particles after 5 hour reduction experiments (100x magnification).

(a) 640 K & 50 vol% H_2, $X = 0.08$

(b) 629 K & 75 vol% H_2, $X = 0.11$

(c) 624 K, 100 vol% H_2, $X = 0.13$

(d) 705 K & 50 vol% H_2, $X = 0.18$

(e) 722 K & 75 vol% H_2, $X = 0.29$

(f) 725 K, 100 vol% H_2, $X = 0.39$

(g) 828 K, 50 vol% H_2, $X = 0.37$

(h) 822 K, 75 vol% H_2, $X = 0.52$

(i) 807 K, 100 vol% H_2, $X = 0.61$

Figure 5.13: Scanning electron microscopy images of the particles after 5 hour reduction experiments (1000x magnification).

5.5 Conclusions

The fluidization and reduction behavior of combusted iron powder is investigated in a lab-scale fluidized bed. The minimum fluidization velocity is measured for different bed heights, temperatures and fluidizing gases:

- The influence of the static bed height on the minimum fluidization velocity at room temperature is insignificant for normalized static bed heights H/D above 0.5. However, below this value, the influence is not negligible due to shallow bed effects.

- The minimum fluidization velocity at elevated temperatures is reported for nitrogen and hydrogen. The measured minimum fluidization velocity starts to deviate from the Ergun correlation at temperatures above 560 K.

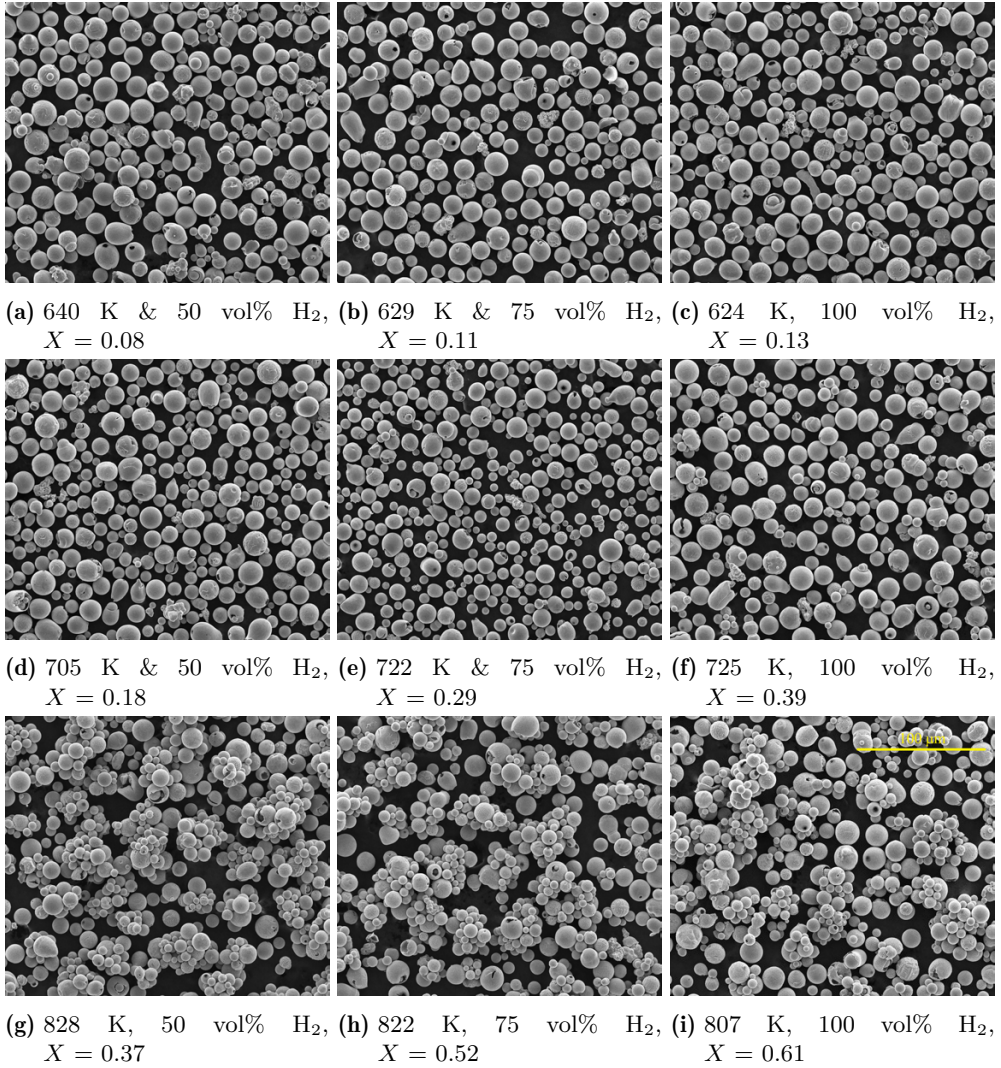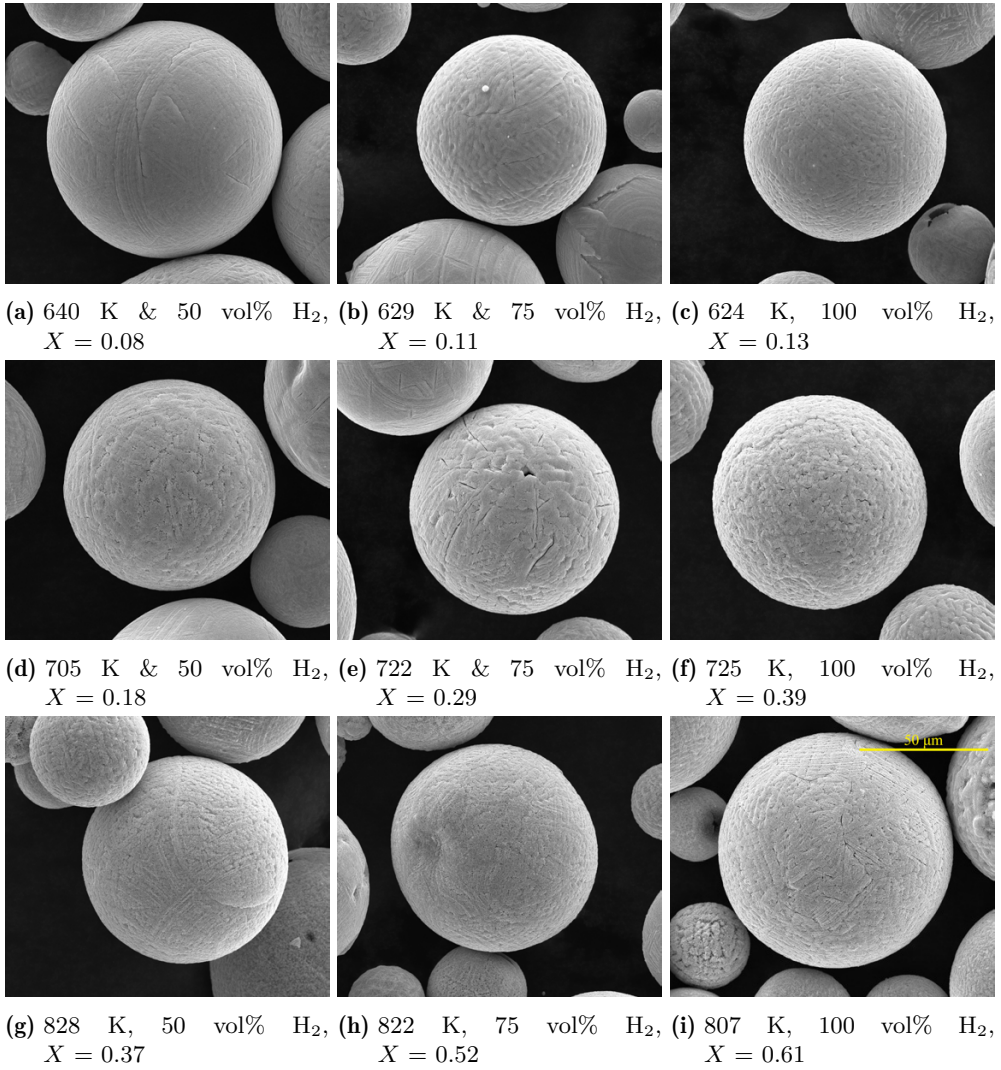- The Ergun equation is extended by considering the cohesive solid bridge force to better predict the u_{mf} at elevated temperatures. This new correlation is validated by our experimental results.

5 hour reduction experiments at equal excess velocity were carried out between 623 and 823 K and at hydrogen concentrations of 50, 75 and 100 vol%:

- Gradual defluidization occurs at temperatures above 800 K, due to the formation of many agglomerates.

- A maximum reduction degree of 61% is obtained at 807 K and 100 vol% hydrogen, even though defluidization occurs.

- The surfaces of the particles became highly porous during reduction. Since the particle surface morphology was equal for all experiments, even though the obtained reduction degree varied, it suggests that the surface already fully reduces to iron in an early stage of the reduction process, confirming a shrinking core principle.

This work contributes to the design of high temperature fluidized beds using metallic powders (such as for chemical looping combustion). It also supports the research being carried out on green steelmaking (DRI), and the metal energy carrier cycle.

6 Conclusions and Outlook
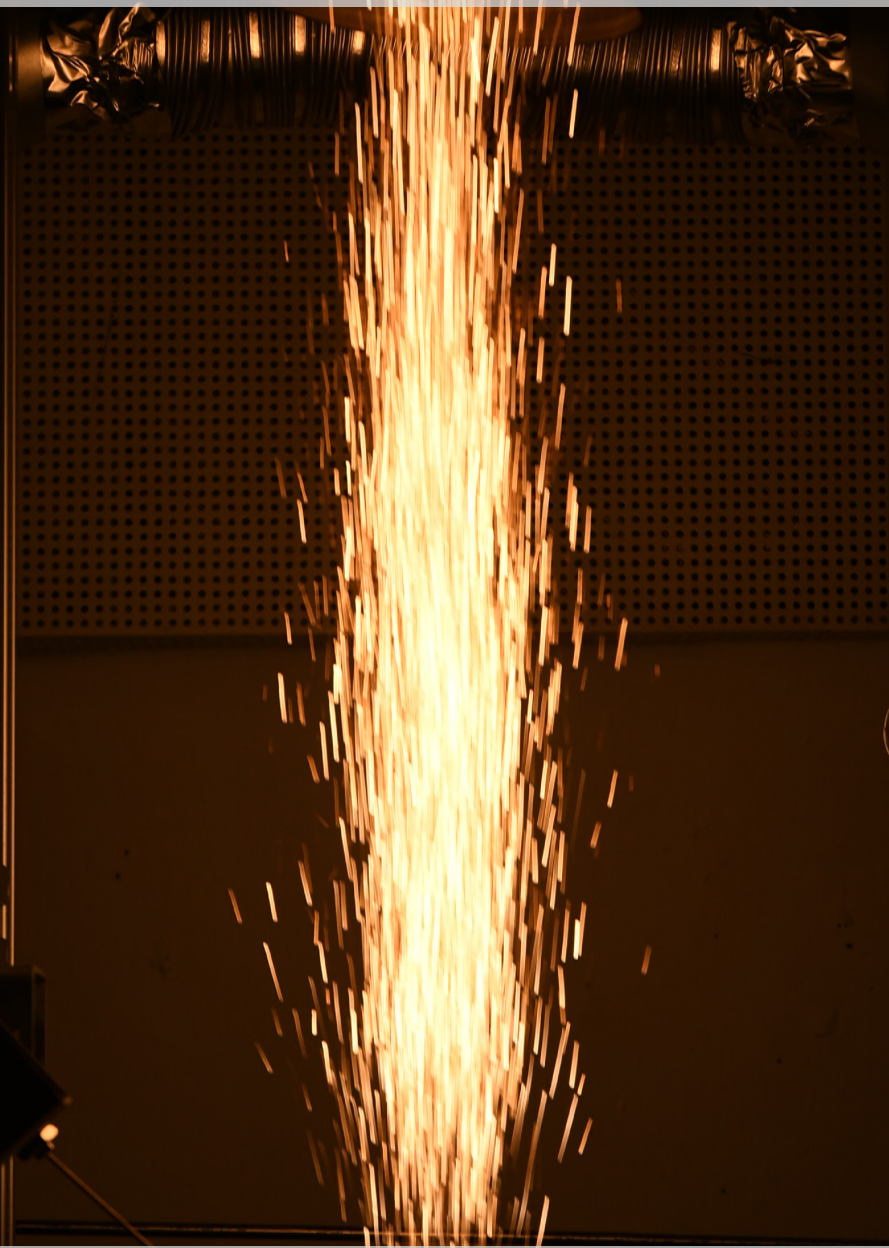
Background image: photograph of regenerated iron powder combusting in a jet-in-hot-coflow burner. See Appendix A.3 for more details. Image courtesy of J. Hameete.

Abstract

Each of the previous chapters of this thesis shine light on different aspects of the reduction process for the use of iron powder as a dense energy carrier. Moreover, the results of each chapter are acquired using a different reactor containing a different amount of powder ($\approx 0.1-1000$ g). This concluding chapter summarizes the key findings and provides recommendations for further investigation into the reduction process.

6.1 Conclusions

The goal of this thesis was to provide insight for the design of the reduction process of combusted iron powder using hydrogen. This was done by performing a detailed kinetic study using a thermogravimetric analyzer (Chapter 3), a sintering study using a packed bed reactor (Chapter 4), and a fluidization & reduction study using a fluidized bed reactor (Chapter 5). The findings from each study are summarized in the individual chapters. Here, the overall findings/insights are summarized in the following:

- The pore morphology of the produced sponge iron powder is strongly dependent on the reaction temperature (above 600 °C), while only to a minor extend on the hydrogen concentration. Pore size increases consistently with reduction temperature, while the overall porosity seems to be independent of temperature. This means that the effective surface area of the powder can be tuned using the reduction temperature, possibly leading to different (auto-)ignition behavior of the produced iron powder.

- Iron "whiskers" form on the surface of the particle during reduction at temperatures above 700 °C and hydrogen concentrations below 25 vol%. These whiskers can lead to increased sticking/agglomeration of the powder and reduced flowability. Furthermore, these whiskers are expected to break off during powder handling, producing (sub-)micron-sized fines. These fines pose health and safety risks due to dust formation. Conditions at which these whiskers are formed should therefore be avoided in reduction systems.

- Proper determination of the kinetic mechanism/triplet cannot be carried out by using solely the standard model fitting method, the iso-conversional method or the standard Hancock-Sharp method. The use of this might lead to incorrect interpretation of the mechanism and therefore to incorrect kinetic parameters. An extended version of the Hancock-Sharp method was proposed that can illuminate which mechanism is dominant and therefore helps in the correct interpretation of kinetic results.

- The reduction kinetics of iron-oxide are heavily influenced by the existence of wüstite as a stable intermediate species from around 600 °C. Below this temperature the reduction process, in excess amount of hydrogen, follows a classical single-step phase boundary controlled shrinking core model. Full reduction can be obtained within 10 minutes at 500 °C and 100 vol% H_2 for small powders

(< 50 μm). Although the initial reduction rate increases further with temperature, the reaction is strongly inhibited from a reduction degree of 60% onwards at these higher temperatures.

- Sintering of powder occured in both reducing (H_2) and non-reducing (N_2) atmospheres at temperatures from 600 °C onwards. The force required to break this sintering increases exponentially with temperature. It was found that a decrease in contact time has a much smaller effect on this sintering, indicating that a sole increase in superficial gas velocity in bubbling fluidized beds can most likely not prevent sintering. Locations in combustion and reduction systems where particles are in frequent contact (such as cyclones and bubbling fluidized beds) should therefore be kept below 600 °C to prevent sintering.

- The cohesiveness of combusted iron powder leads to an increase of the minimum fluidization velocity, from a bed temperature of 300 °C. This increase can be predicted accurately by incorporating the cohesive inter-particle force in the Ergun correlation.

- Reduction of combusted iron using a bubbling fluidized bed should be kept below 530 °C in order to prevent gradual defluidization from occurring. The produced powder is spherical and porous, providing good flowability and ignition behavior for cyclic combustion-reduction processes.

6.2 Outlook

In this study, many new insights were obtained on the reduction, sintering and fluidization behavior of iron-oxide powder using hydrogen, which are valuable for the future of the metal energy carrier cycle, but in a broader sense to fossil-free future of iron-making and chemical looping combustion. However, many new research questions also arise, which were not investigated due to time and recourse restrictions. These can be summarized as:

- The influence of particle size, initial composition and water vapor concentration on the reduction kinetics should be investigated in more detail, to extend and improve on the current understanding of the kinetic mechanism. Especially the influence of the water vapor concentration is needed for correct implementation of the kinetic model in numerical models of dense particle systems (such as fluidized beds).

- Cross-sections of partially reduced powder can provide valuable insight into the reduction behavior, by analyzing their morphology and local composition. Especially the local concentration and distribution of the different oxides (hematite, magnetite, wüstite and iron) can aid in further refinement of the kinetic mechanism.

- Brunauer-Emmett-Teller (BET) surface area analysis measurements can be used to quantify the effective surface area of the particle after reduction. This parameter determines the amount of area of the powder in direct contact with air and will therefore probably correlate to the reactivity and ignitability of the powder.

- The sintering behavior of the combusted and regenerated powder can be further understood by extending the current measurements presented in Chapter 4 to shorter contact times and by improving the compression method for better quantification.

- Reduction and combustion experiments should be carried out over multiple consecutive cycles to evaluate whether changes occur in the reduction and combustion behavior. It can also provide insights in the viability of the metal energy carrier cycle.

- The use of a circulating fluidized bed might allow for better hydrogen utilization, (slightly) higher temperatures and possibly allow for shorter reduction times. It can also provide more practical information for feasibility studies on the entire cycle.

- The influence of impurities, as stated in Chapter 2, was assumed negligible in this research, partly due to the use of high purity iron powder as "virgin" material. However, it is known that doping and coating of iron powder can improve the reduction behavior of iron-oxides. As long as these additives can be well controlled and maintained over multiple cycles, they have the potential to improve the energy carrier cycle efficiency.

6

A Appendices

Abstract

The appendices to this thesis contain additional results that were left out of the main chapters of this thesis. Appendix A.1 contains a cyclic oxidation and reduction experiment performed in the thermogravimetric analyzer as part of the kinetic research described in Chapter 3. These experiments suffer from severe sintering, limiting proper interpretation. Appendix A.2 presents drop tube reduction test that were performed to evaluate the reduction behavior at high temperatures. The residence times were too short for significant reduction. Finally, in Appendix A.3, the regenerated powder, similar to that produced in Chapter 5 is combusted as a trial experiment in a newly designed jet-in-hot-coflow burner. The burner was unfortunately not yet optimized for quantitative measurements.

A.1 Cyclic reduction-oxidation experiment

In an attempt to investigate both the oxidation and reduction kinetics of iron(-oxide), a cyclic experiment is carried out in the thermogravimetric analyzer described in Chapter 3. 118 mg of combusted iron powder, from the same batch as in Chapter 3, is used. The reactor temperature was set to 600 °C. Each reduction step was set to a duration of 40 minutes, using a flow rate of 0.48 NLPM of 50:50 vol% N_2:H_2. Each subsequent oxidation step was set for 90 minutes, using 0.48 NLPM of air (21 vol% O_2).

Figure A.1 shows the reduction degree in time for 8 reduction-oxidation (redox) cycles. It should be noted that for the first oxidation step, the duration was only 60 minutes.
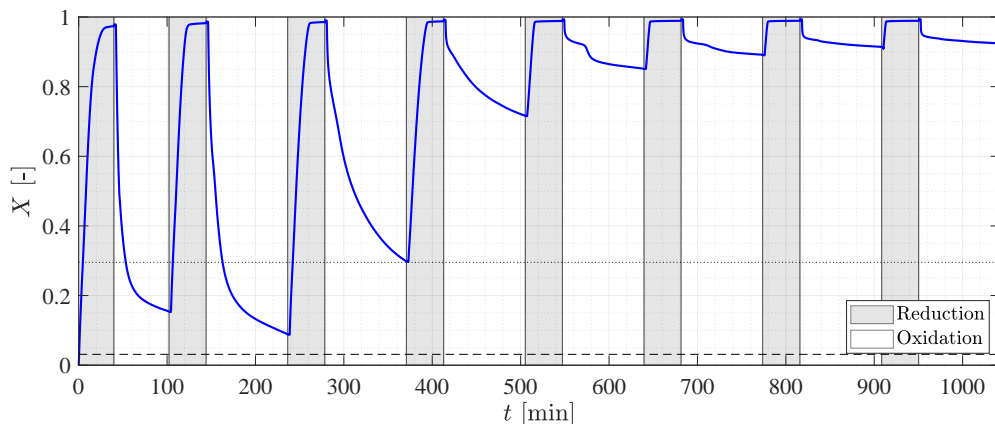

Figure A.1: Reduction degree in time for 8 redox cycles at 600 °C. The reduction time is 40 minutes using 50:50 vol% N_2:H_2, while the oxidation time is 90 minutes using air (21 vol% O_2). The black dashed and dotted horizontal lines in the figure represent full conversion to magnetite and wüstite, respectively, if the reactions take place step-by-step.
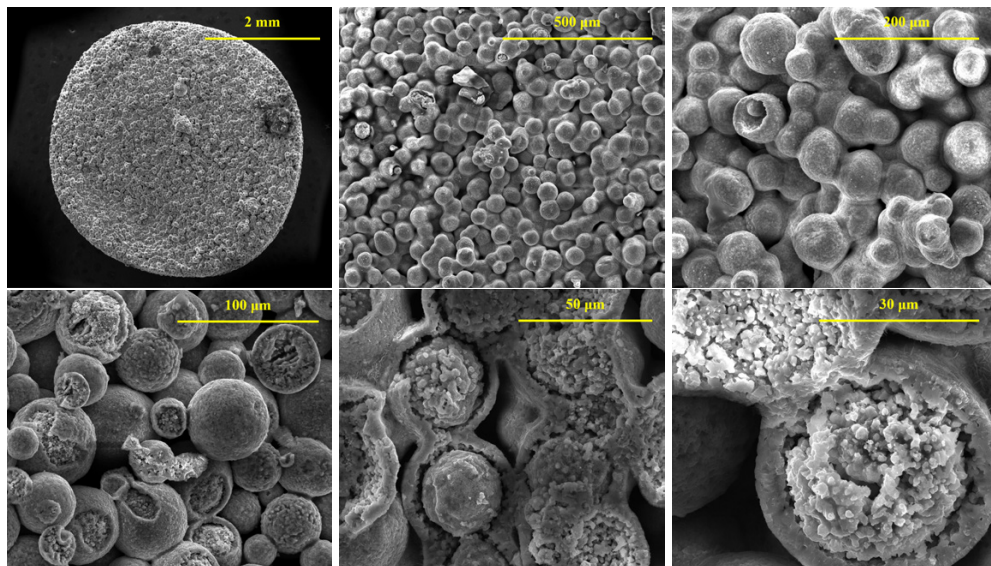
Figure A.2: Scanning electron microscope images of oxidized iron powder pellet after 8 reduction-oxidation cycles at 600 °C. The bottom three images are taken from a crosscut of the pellet.

From the reduction degree, we can see that (near) full reduction ($X = 1$) is consistently reached within the 40 minutes reduction time. Moreover, the reduction rate (slope) seems to be constant between cycles. However, we can see that full oxidation ($X = 0$) is not reached during any of the cycles. The oxidation potential of the powder seems to decrease over multiple cycles. That is, the obtained oxidation degree ($1 - X$) decreases for each subsequent oxidation step. After 8 cycles, less then 10% of the material is oxidized, of which most occurs in the first 5 minutes of exposure to air.

Figure A.2 shows scanning electron microscope images of the sample (including a crosscut) taken out of the thermogravimetric analyzer. It can be seen that the powder has fully sintered together, thereby strongly inhibiting the gas from reaching the interior iron. Moreover, from the crosscut images we can see that a shell has formed around each particle. Shell formation has previously been observed before during iron(-oxide) redox cycles with hydrogen by Qin *et al.* [63]. Since the last step of the redox cycle was oxidation, this shell most likely consists of iron-oxide, while the porous interior probably consists mostly of iron. This shell forms a dense/protective layer, prohibiting oxygen from reaching the particles interior, thereby limiting the oxidation rate. Since, during the reduction, pores are formed, these shells do not inhibit the hydrogen and therefore the reduction process.

However, a cyclic TGA study is not representative of the combustion step of the metal energy carrier cycle, which in a real burner has a very different, much more effective oxidation mechanism. We can conclude from this experiment that cyclic reduction-oxidation in a packed bed type of reactor, leads to a degradation of the powder during the oxidation stage. More research would be required to understand this degradation process as well as to find strategies to prevent it.

A.2 Drop tube reduction experiments

To investigate the reduction behavior of combusted iron powder with hydrogen at higher temperatures than presented in Chapter 3, experiments are carrier out in a drop tube furnace at Delft University of Technology at temperatures between 900-1100 °C with 100 vol% H_2. A schematic of the setup is provided in Figure A.3, while a full description can be found in Qu [136]. This setup has been used before to study the reduction and decomposition behavior of iron ores [67, 83, 137]. Similar research for the development of green steelmaking has been performed by Sohn *et al.* [66, 115, 138–140]. A 60 mm inner diameter "Alsint" tube is surrounded by an electrical heating element. A "carrier" gas flow (pre-heated to 500 °C) is used in conjunction with a syringe pump particle feeder to inject the powder into the top of the furnace (powder feeding rate is roughly 1-2 g/h). The injection tube has an inner diameter of 3 mm. A separate "main" gas flow is provided in a co-flow arrangement. The total length of the drop tube is 1100 mm, while the hot zone (heated region) is 410 mm. A sample collector is placed below the drop tube to capture the particles.

The combusted iron powder used is similar to the one used in Chapter 3. The composition is 45 wt% Fe_2O_3 and 55 wt% Fe_3O_4. The powder was manually sieved under 63 μm using mesh sieves, to prevent large particles/agglomerates from blocking the particle feeding system. The size distribution, determined using dynamic image analysis, as well as a scanning electron microscope image are presented in Figure A.4. The Sauter mean diameter d_{32} is 42.4 μm and $D_{v10} : D_{v50} : D_{v90} = 32.0 : 44.4 : 59.0$ μm. The experimental conditions used are mentioned in Table A.1. The residence time of the particle in the hot zone of the drop tube furnace is calculated using Newton's second law of motion (assuming Stokes flow), similar to the description given by Qu *et al.* [67].
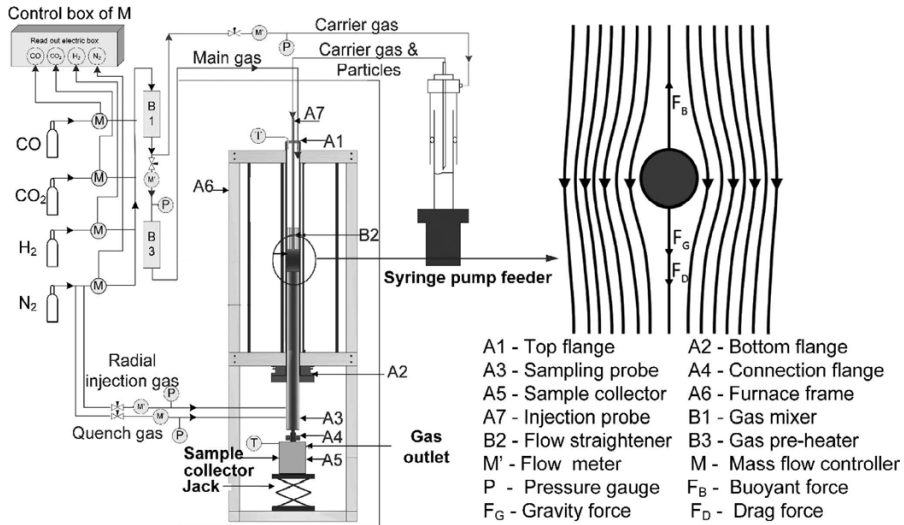
Figure A.3: Schematic of the high temperature drop tube furnace (left) and forces acting on a particle (top right). Adapted from Qu *et al.* [67].
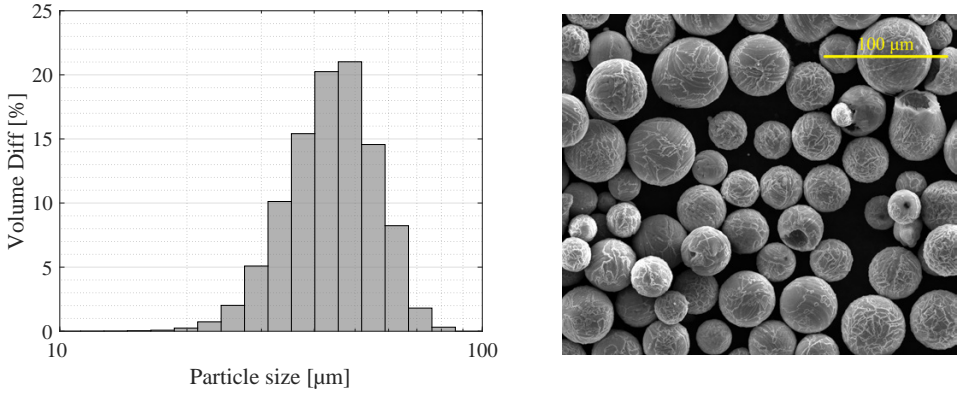
Figure A.4: Particle size distribution (left) and scanning electron microscope image (right) of the (sieved) combusted iron particles.

Table A.1: Experimental conditions used in the drop tube furnace experiments.

Gas composition	Temperature	Carrier gas	Main gas	Residence time
100 vol% H_2	900°C	0.3 NLPM	2.7 NLPM	~ 650 ms
100 vol% H_2	1000°C	0.3 NLPM	1.7 NLPM	~ 680 ms
100 vol% H_2	1100°C	0.3 NLPM	1.7 NLPM	~ 715 ms

(a) 900 °C **(b)** 1000 °C **(c)** 1100 °C
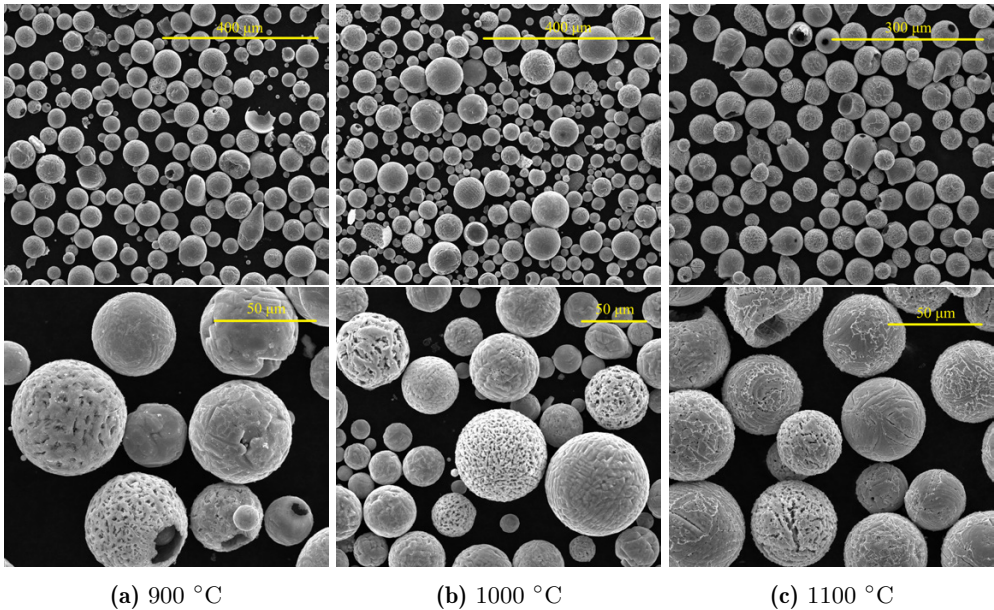
Figure A.5: Scanning electron microscope images of combusted iron powder, partially reduced in the drop tube furnace.

Table A.2: Semi-quantitative X-ray diffraction results of drop tube reduced powder.

Case	Fe	FeO	Fe$_3$O$_4$	Fe$_2$O$_3$	Unit
Original	0	0	33	67	wt%
900 °C	3	2	72	23	wt%
1000 °C	3	2	78	17	wt%
1100 °C	2	18	76	4	wt%

Scanning electron microscope images of the powder after reduction can be seen in Figure A.5. The particles become porous, indicating that the particles are (at least) partly reduced. However, there is quite some difference in porosity between individual particles in all three cases. Some particles, especially in the 900 °C case, look nearly identical to the original powder, while others have become significantly porous. This result is different from the other experiments presented in this thesis, and might be either a result of the short residence time, the high temperature or from improper dispersion of the powder.

Semi-quantitative X-ray diffraction is carried out to determine the changes in composition. The results can be seen in Table A.2. It should be noted that these results are semi-quantitative, meaning that relative differences can be inferred, but no quantitative factors. We can see that the hematite concentration decreases systematically with reduction temperature. This hematite is converted into magnetite. However, except for the 1100 °C, only a small amount of the magnetite is converted into wüstite and iron. This indicated that the hematite to magnetite reaction occurs faster than the magnetite to wüstite reaction.

The most important conclusion is that the conversion to iron is very low due to the short residence times in these experiments, rendering the drop tube experiment unsuited for studying full iron-oxide reduction. More experiments would be required to investigate the reduction behavior at even higher temperatures and/or longer residence times.

A.3 Combustion behavior of regenerated powder

The properties as well as combustion behavior of regenerated powder, produced using the fluidized bed described in Chapter 5, is compared with that of "virgin" iron powder, commercially produced using an arc furnace in combination with subsequent water atomization.

To produce the regenerated powder, a similar reduction experiment is performed as described in Section 5.4. An excess velocity of 26 mm/s (on top of the minimum fluidization velocity) is used in combination with 100 vol% H_2. The pressure drop and temperature profile in time can be seen in Figure A.6. Occasionally, short bursts of a higher hydrogen flow rate are provided in an attempt to break up any agglomerates. These bursts are visible in the graph by short spikes (increases) in the pressure drop profile. Furthermore the temperature was reduced during the experiment, in order to reduce the defluidization. However, the bed still defluidized over the course of the experiment. A maximum reduction degree of 75.6% is eventually obtained. X-ray diffraction indicated that the powder consists of around 70 wt% iron and 30% magnetite. No hematite or wüstite phases are present.

The produced regenerated powder is analyzed alongside the original (virgin) powder Rio Tinto (ATOMET95), as well as the combusted powder. Scanning electron microscopy images of the powders are presented in Figure A.7. The particle size distributions (from dynamic image analysis) are given in Figure A.8. Semi-quantitative X-ray diffraction indicated that the virgin powder consisted almost entirely out of iron, while the regenerated powder consisted of a mixture iron and magnetite (see Table A.4). Other determined material properties are summarized in Table A.3.

The results show that the virgin powder is quite different from the combusted and regenerated powder in particle size and shape (smaller and less round, respectively). Furthermore, the reduced powder is effectively the same size as the combusted powder, but has a much larger inner porosity. This, in combination with a lower reduction degree compared to the virgin iron powder, substantially lowers the energy density of the material in comparison to the virgin powder.
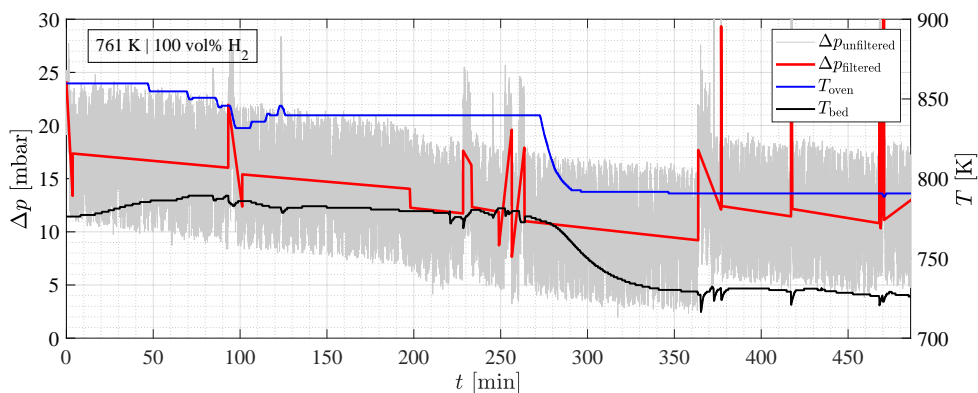
Figure A.6: Pressure drop and temperature profile during the reduction experiment.
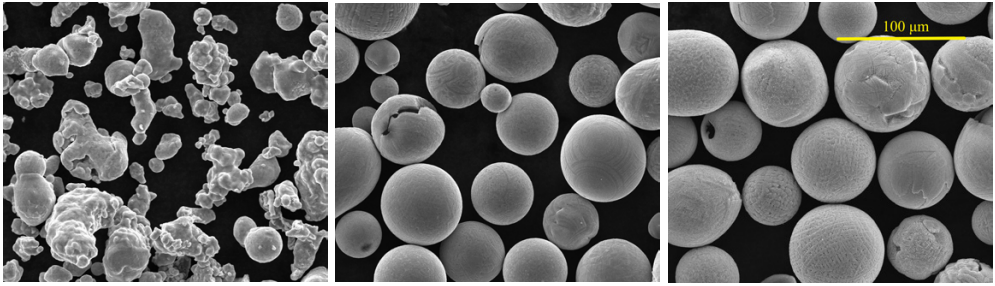
Figure A.7: Scanning electron microscope images of: virgin (left), combusted (center) and regenerated (right) iron power.
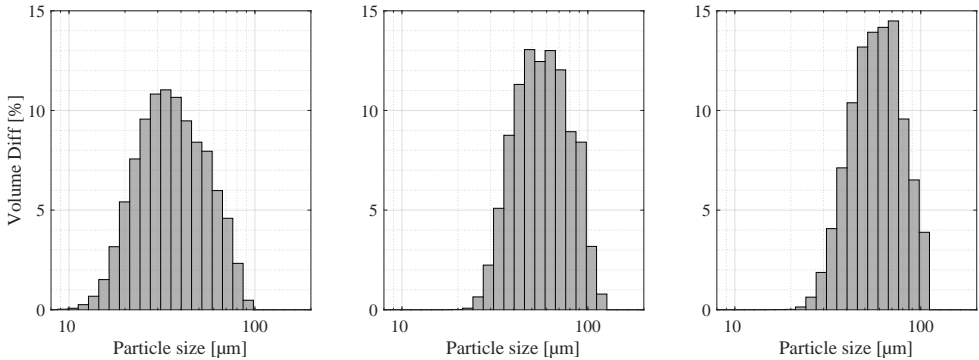
Figure A.8: Particle size distributions of: virgin (left), combusted (center) and regenerated (right) iron power.

Table A.3: Properties of virgin, combusted and reduced powder.

Property	Virgin	Combusted	Regenerated	Unit
Sauter diameter, d_{32}	32.7	53.6	54.6	µm
Average L/D, $\overline{LD}$	1.403	1.092	1.126	-
Bulk density[1], ρ_b	4027	2910	2320	kg/m^3
Particle density[2], ρ_p	7820	4700	3750	kg/m^3
Solid density[3], ρ_s	7820	5270	6835	kg/m^3
Internal porosity, ε_p	0	10	45	%
Reduction degree[4], X	-	-	75.6	%
Ferrite content[5]	99	7	71	wt%
Energy density[6]	29.5	-	12.5	MJ/L
Specific energy	7.3	-	5.4	MJ/kg

[1] Measured using a 100 mL measuring cylinder (vibrated).
[2] Based on a packing density of 0.62 (poured random packing) for combusted & regenerated powder.
[3] Estimated using known solid densities of pure constituents.
[4] Defined as the weight loss during reduction, divided by the weight loss for full conversion to Fe.
[5] Defined as the weight of α-Fe present, divided by the total mass.
[6] Based on the bulk density mentioned and full combustion to Fe_2O_3.

(a) 3 NLPM jet-flow   **(b)** 10 NLPM jet-flow   **(c)** 30 NLPM jet-flow
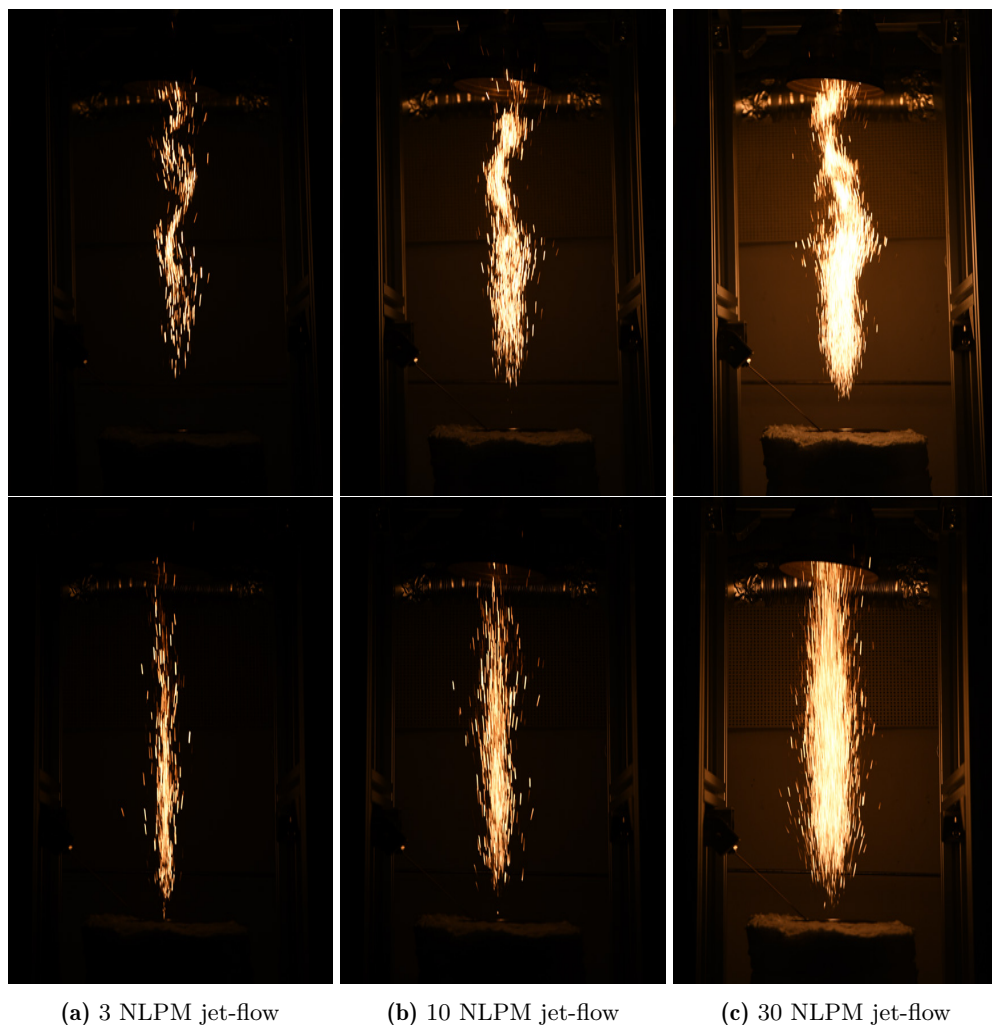
Figure A.9: Photographs of virgin (top) and regenerated (bottom) iron powder, combusting in a Jet-in-Hot-Coflow burner, using three different jet-flow velocities (and thus powder feeding rate). Camera placement and settings are identical for all cases. For reference, the distance between burner tip and suction hood is roughly 0.45 m. Photographs courtesy of J. Hameete.

To compare the combustion behavior of virgin and regenerated powder, experiments are conducted using a Jet-in-Hot-Coflow burner, developed by L. Boone. Details about the burner can be found in his master thesis [141]. A co-flow temperature of 993 K is used, measured at the height of the burner tip. The co-flow (600 NLPM air) and jet-flow (3-30 NLPM air) are set using Bronkhorst EL-Flow mass flow controllers. The jet-flow was also used to disperse the powder, using an air-knife & piston dispersion system. Unfortunately the exact powder feeding rates could not be determined, which means that the results can only be interpreted qualitatively.
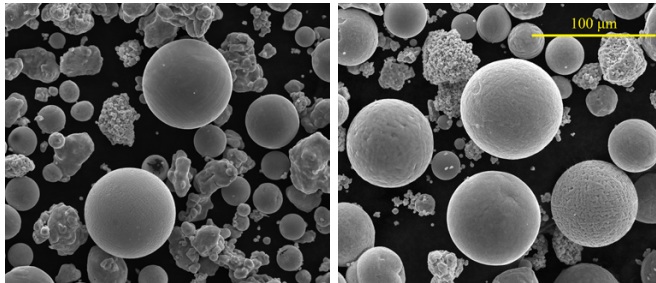
Figure A.10: Scanning electron microscope images of virgin (left) and regenerated (right) iron powder, after combusted in a Jet-in-Hot-Coflow burner.

Table A.4: Semi-quantitative X-ray diffraction results of Jet-in-Hot-Coflow combusted powder.

Case	Fe	FeO	Fe_3O_4	Fe_2O_3	Unit
Virgin	99	1	0	0	wt%
Combusted virgin	68	2	30	0	wt%
Regenerated	63	0	37	0	wt%
Combusted regenerated	49	13	36	2	wt%

Figure A.9 shows the combustion behavior of virgin and regenerated powder. All images are taken with equal camera settings (Nikon D7500, 56 mm, f/4.5 lens, 1/400 s exposure time). From the images a couple of observations can be made. First, we can observe that the regenerated powder results in less flame fluctuations/instabilities compared to the virgin powder. This most likely has to do with the lower density of the particles, meaning that they follow the flow better. Secondly, we can observe that the particles ignite earlier, i.e. at a lower height above the burner. This can be explained by the higher porosity of the regenerated powder, causing both a faster heat-up time and a larger effective surface area for initial oxidation. Finally, the accumulated light is consistently less in the case of regenerated powder. This matches with the fact that the energy density for this powder is lower.

Scanning electron microscope images of the powders are given in Figure A.10. From these two images we can observe that not all powder combusts (indicated by the irregularly shaped particles, matching the size and shape of Rio Tinto ATOMET95 powder). However, the particles that do combust seem to have a similar shape and size, indicating that the regenerated powder might produce similar powder after combustion. Results of semi-quantitative X-ray diffraction can be seen in Table A.4. We can see that a large amount of the original iron did not combust (fully). Interestingly, wüstite and magnetite are formed during the combustion of regenerated powder, while only magnetite is formed when virgin iron powder is combusted.

Further analysis using a well-defined combustion system is required to fully understand the combustion behavior of regenerated powder and the differences with virgin iron powder combustion.

Bibliography

[1]   J. M. Matsen, „Design and scale-up of CFB catalytic reactors", in *Circulating Fluidized Beds*, J. R. Grace, A. A. Avidan, and T. M. Knowlton, Eds. Dordrecht: Springer Netherlands, 1997, pp. 489–503.

[2]   D. I. A. McKay, A. Staal, J. F. Abrams, R. Winkelmann, B. Sakschewski, S. Loriani, I. Fetzer, S. E. Cornell, J. Rockström, and T. M. Lenton, „Exceeding 1.5 °C global warming could trigger multiple climate tipping points", *Science*, vol. 377, no. 6611, 2022.

[3]   European Commission and Directorate-General for Communication, *European green deal: delivering on our targets*. Publications Office of the European Union, 2021.

[4]   „Infographic: energy in figures", Energie Beheer Nederland (EBN), Tech. Rep., 2022.

[5]   „Global Hydrogen Review 2022", International Energy Agency (IEA), Paris, Tech. Rep., 2022.

[6]   D. Mignard and C. Pritchard, „A review of the sponge iron process for the storage and transmission of remotely generated marine energy", *International Journal of Hydrogen Energy*, vol. 32, no. 18, pp. 5039–5049, 2007.

[7]   J. M. Bergthorson, S. Goroshin, M. J. Soo, P. Julien, J. Palečka, D. L. Frost, and D. J. Jarvis, „Direct combustion of recyclable metal fuels for zero-carbon heat and power", *Applied Energy*, vol. 160, pp. 368–382, 2015.

[8]   S. Fischer and M. Grubelich, „Theoretical energy release of thermites, intermetallics, and combustible metals", Tech. Rep., 1998.

[9]   „Powder Metallurgy Market Size, Share & Trends Analysis Report By Material (Titanium, Steel), By Process (MIM, PM HIP), By Application (Automotive, Oil & Gas), By End-use (OEM, AM Operators), And Segment Forecasts, 2021 - 2028", Grand View Research, Tech. Rep.

[10] D. Nuber, H. Eichberger, and B. Rollinger, „Circored fine ore direct reduction", *Millennium steel 2006*, pp. 37–40, 2006.

[11] M. Pei, M. Petäjäniemi, A. Regnell, and O. Wijk, „Toward a Fossil Free Future with HYBRIT: Development of Iron and Steelmaking Technology in Sweden and Finland", *Metals*, vol. 10, no. 7, 2020.

[12] Z. Fan and S. J. Friedmann, „Low-carbon production of iron and steel: Technology options, economic assessment, and policy", *Joule*, vol. 5, no. 4, pp. 829–862, 2021.

[13] T. Battle, U. Srivastava, J. Kopfle, R. Hunter, and J. McClelland, „Chapter 1.2 - The Direct Reduction of Iron", in *Treatise on Process Metallurgy*, S. Seetharaman, Ed., Boston: Elsevier, 2014, pp. 89–176.

[14] J. L. Schenk, „Recent status of fluidized bed technologies for producing iron input materials for steelmaking", *Particuology*, vol. 9, no. 1, pp. 14–23, 2011.

[15] D. Spreitzer and J. Schenk, „Reduction of Iron Oxides with Hydrogen—A Review", *Steel Res. Int.*, p. 1 900 108, 2019.

[16]   A. Z. Ghadi, M. S. Valipour, S. M. Vahedi, and H. Y. Sohn, „A Review on the Modeling of Gaseous Reduction of Iron Oxide Pellets", *steel research international*, vol. 91, no. 1, p. 1 900 270, 2019.

[17]   M. Komatina and H. W. Guidenau, „The sticking problem during direct reduction of fine iron ore in the fluidized bed", *Metalurgija*, vol. 10, no. 4, pp. 309–328, 2004.

[18]   L. Guo, Q. Bao, J. Gao, Q. Zhu, and Z. Guo, „A Review on Prevention of Sticking during Fluidized Bed Reduction of Fine Iron Ore", *ISIJ International*, vol. 60, no. 1, pp. 1–17, 2020.

[19]   H. Y. Sohn, „Hydrogen-Based Flash Ironmaking Technology (HyFIT): A Novel Green Ironmaking Technology With Low Energy Consumption", in *Encyclopedia of Nuclear Energy*, Elsevier, 2021, pp. 122–130.

[20]   Ponor, *Electron-matter interaction volume and various types of signal generated*, CC BY-SA 4.0, Wikimedia Commons, 2020.

[21]   L. Choisez, N. E. van Rooij, C. J. M. Hessels, A. K. da Silva, I. R. Souza Filho, Y. Ma, P. de Goey, H. Springer, and D. Raabe, „Phase transformations and microstructure evolution during combustion of iron powder", *Acta Materialia*, vol. 239, p. 118 261, 2022.

[22]   J. G. Whiting, E. J. Garboczi, V. N. Tondare, J. H. J. Scott, M. A. Donmez, and S. P. Moylan, „A comparison of particle size distribution and morphology data acquired using lab-based and commercially available techniques: Application to stainless steel powder", *Powder Technology*, vol. 396, pp. 648–662, 2022.

[23]   RETSCH GmbH Haan, *Sieve Analysis: Taking a close look at Quality*, Verder Scientific, 2015.

[24]   F. A. L. Dullien, *Porous Media: Fluid Transport and Pore Structure*, 2nd. Academic Press, 1992.

[25]   D. L. Bish and J. E. Post, Eds., *Modern Powder Diffraction*, ser. Reviews in Mineralogy. Washington, D.C.: The Mineralogical Society of America, 1989, vol. 20.

[26]   Y. M. Mos, A. C. Vermeulen, C. J. N. Buisman, and J. Weijma, „X-Ray Diffraction of Iron Containing Samples: The Importance of a Suitable Configuration", *Geomicrobiology Journal*, vol. 35, no. 6, pp. 511–517, 2018.

[27]   P. I. Guntoro, Y. Ghorbani, P.-H. Koch, and J. Rosenkranz, „X-ray Microcomputed Tomography (μCT) for Mineral Characterization: A Review of Data Analysis Methods", *Minerals*, vol. 9, no. 3, p. 183, 2019.

[28]   A. du Plessis, P. Sperling, A. Beerlink, W. B. du Preez, and S. G. le Roux, „Standard method for microCT-based additive manufacturing quality control 4: Metal powder analysis", *MethodsX*, vol. 5, pp. 1336–1345, 2018.

[29]   S. Goroshin, J. Palečka, and J. M. Bergthorson, „Some fundamental aspects of laminar flames in nonvolatile solid fuel suspensions", *Prog. Energ Combust. Sci.*, vol. 91, p. 100 994, 2022.

[30]   D. Ning, Y. L. Shoshin, J. A. van Oijen, G. Finotello, and L. P. H. de Goey, „Burn time and combustion regime of laser-ignited single iron particle", *Combust. Flame*, vol. 230, p. 111 424, 2021.

[31] D. Ning, Y. L. Shoshin, M. van Stiphout, J. A. van Oijen, G. Finotello, and L. P. H. de Goey, „Temperature and phase transitions of laser-ignited single iron particle", *Combustion and Flame*, vol. 236, p. 111 801, 2022.

[32] J. Huang, S. Li, D. Sanned, L. Xu, S. Xu, Q. Wang, M. Stiti, Y. Qian, W. Cai, E. Berrocal, M. Richter, M. Aldén, and Z. Li, „A detailed study on the micro-explosion of burning iron particles in hot oxidizing environments", *Combustion and Flame*, vol. 238, p. 111 755, 2021.

[33] S. Li, D. Sanned, J. Huang, E. Berrocal, W. Cai, M. Aldén, M. Richter, and Z. Li, „Stereoscopic high-speed imaging of iron microexplosions and nanoparticle-release", *Opt. Express*, vol. 29, no. 21, pp. 34 465–34 476, 2021.

[34] D. Ning, Y. L. Shoshin, J. A. van Oijen, G. Finotello, and L. P. H. de Goey, „Critical temperature for nanoparticle cloud formation during combustion of single micron-sized iron particle", *Combustion and Flame*, vol. 244, p. 112 296, 2022.

[35] D. Ning, Y. L. Shoshin, J. A. van Oijen, G. Finotello, and L. P. H. de Goey, „Size evolution during laser-ignited single iron particle combustion", *Proceedings of the Combustion Institute*, 2022.

[36] P. Tóth, Y. Ögren, A. Sepman, P. Gren, and H. Wiinikka, „Combustion behavior of pulverized sponge iron as a recyclable electrofuel", *Powder Technol.*, vol. 373, pp. 210–219, 2020.

[37] N. Poletaev and M. Khlebnikova, „Combustion of Iron Particles Suspension in Laminar Premixed and Diffusion Flames", *Combustion Science and Technology*, vol. 0, no. 0, pp. 1–22, 2020.

[38] J. Huang, S. Li, W. Cai, Y. Qian, E. Berrocal, M. Aldén, and Z. Li, „Quantification of the size, 3D location and velocity of burning iron particles in premixed methane flames using high-speed digital in-line holography", *Combustion and Flame*, vol. 230, p. 111 430, 2021.

[39] P. Julien, S. Whiteley, S. Goroshin, M. J. Soo, D. L. Frost, and J. M. Bergthorson, „Flame structure and particle-combustion regimes in premixed methane - iron - air suspensions", *Proceedings of the Combustion Institute*, vol. 35, no. 2, pp. 2431–2438, 2015.

[40] M. McRae, P. Julien, S. Salvo, S. Goroshin, D. L. Frost, and J. M. Bergthorson, „Stabilized, flat iron flames on a hot counterflow burner", *Proceedings of the Combustion Institute*, vol. 37, no. 3, pp. 3185–3191, 2019.

[41] F.-D. Tang, S. Goroshin, and A. J. Higgins, „Modes of particle combustion in iron dust flames", *Proceedings of the Combustion Institute*, vol. 33, no. 2, pp. 1975–1982, 2011.

[42] J. Palečka, J. Sniatowsky, S. Goroshin, A. J. Higgins, and J. M. Bergthorson, „A new kind of flame: Observation of the discrete flame propagation regime in iron particle suspensions in microgravity", *Combustion and Flame*, vol. 209, pp. 180–186, 2019.

[43] J. Palečka, S. Goroshin, A. J. Higgins, Y. Shoshin, P. de Goey, J.-R. Angilella, H. Oltmann, A. Stein, B. Schmitz, A. Verga, S. Vincent-Bonnieu, W. Sillekens, and J. M. Bergthorson, „Percolating Reaction - Diffusion Waves (PERWAVES) - Sounding rocket combustion experiments", *Acta Astronautica*, vol. 177, pp. 639–651, 2020.

[44] M. Soo, X. Mi, S. Goroshin, A. J. Higgins, and J. M. Bergthorson, „Combustion of particles, agglomerates, and suspensions – A basic thermophysical analysis", *Combust. Flame*, vol. 192, pp. 384–400, 2018.

[45] E. I. Senyurt and E. L. Dreizin, „At what ambient temperature can thermal runaway of a burning metal particle occur?", *Combustion and Flame*, vol. 236, p. 111 800, 2022.

[46] L. C. Thijs, C. E. A. G. van Gool, W. J. S. Ramaekers, J. A. van Oijen, and L. P. H. de Goey, „Resolved simulations of single iron particle combustion and the release of nano-particles", *Proceedings of the Combustion Institute*, 2022.

[47] L. C. Thijs, C. E. A. G. van Gool, W. J. S. Ramaekers, J. G. M. Kuerten, J. A. van Oijen, and L. P. H. de Goey, „Improvement of heat- and mass transfer modeling for single iron particles combustion using resolved simulations", *Combustion Science and Technology*, vol. 0, no. 0, pp. 1–17, 2022.

[48] F.-D. Tang, A. J. Higgins, and S. Goroshin, „Effect of discreteness on heterogeneous flames: Propagation limits in regular and random particle arrays", *Combustion Theory and Modelling*, vol. 13, no. 2, pp. 319–341, 2009.

[49] T. Hazenberg and J. A. van Oijen, „Structures and burning velocities of flames in iron aerosols", *Proceedings of the Combustion Institute*, vol. 38, no. 3, pp. 4383–4390, 2021.

[50] X. Mi, A. Fujinawa, and J. M. Bergthorson, „A quantitative analysis of the ignition characteristics of fine iron particles", *Combustion and Flame*, vol. 240, p. 112 011, 2022.

[51] M. Muller, H. El-Rabii, and R. Fabbro, „Liquid phase combustion of iron in an oxygen atmosphere", *Journal of Materials Science*, vol. 50, no. 9, pp. 3337–3350, 2015.

[52] Y.-H. Li, A. Purwanto, and B.-C. Chuang, „Micro-Explosion mechanism of iron hybrid Methane-Air premixed flames", *Fuel*, vol. 325, p. 124 841, 2022.

[53] E. R. Wainwright, S. V. Lakshman, A. F. Leong, A. H. Kinsey, J. D. Gibbins, S. Q. Arlington, T. Sun, K. Fezzaa, T. C. Hufnagel, and T. P. Weihs, „Viewing internal bubbling and microexplosions in combusting metal particles via x-ray phase contrast imaging", *Combustion and Flame*, vol. 199, pp. 194–203, 2019.

[54] V. Khalajzadeh and C. Beckermann, „Simulation of Shrinkage Porosity Formation During Alloy Solidification", *Metallurgical and Materials Transactions A*, vol. 51, no. 5, pp. 2239–2254, 2020.

[55] H. Zheng, J. Schenk, D. Spreitzer, T. Wolfinger, and O. Daghagheleh, „Review on the Oxidation Behaviors and Kinetics of Magnetite in Particle Scale", *steel research international*, vol. 92, no. 8, p. 2 000 687, 2021.

[56] H. Zheng, J. Schenk, R. Xu, O. Daghagheleh, D. Spreitzer, T. Wolfinger, D. Yang, and Y. Kapelyushin, „Surface Morphology and Structural Evolution of Magnetite-Based Iron Ore Fines During the Oxidation", *Metallurgical and Materials Transactions B*, vol. 53, no. 3, pp. 1644–1660, 2022.

[57] H. Wiinikka, T. Vikstr om, J. Wennebro, P. Tóth, and A. Sepman, „Pulverized Sponge Iron, a Zero-Carbon and Clean Substitute for Fossil Coal in Energy Applications", *Energy & Fuels*, vol. 32, no. 9, pp. 9982–9989, 2018.

[58] H. Zheng, D. Spreitzer, T. Wolfinger, J. Schenk, and R. Xu, „Effect of Prior Oxidation on the Reduction Behavior of Magnetite-Based Iron Ore During Hydrogen-Induced Fluidized Bed Reduction", *Metallurgical and Materials Transactions B*, vol. 52, no. 4, pp. 1955–1971, 2021.

[59] T. Wolfinger, D. Spreitzer, H. Zheng, and J. Schenk, „Influence of a Prior Oxidation on the Reduction Behavior of Magnetite Iron Ore Ultra-Fines Using Hydrogen", *Metallurgical and Materials Transactions B*, vol. 53, no. 1, pp. 14–28, 2021.

[60] *DOE Fundamentals Handbook - Material Science (Volume 1 of 2)*. U. S. Department of Energy, 1993.

[61] L. von Bogdandy and H.-J. Engell, *The Reduction of Iron Ores: Scientific Basis and Technology*. Springer, 1971.

[62] J. Shao, Z. Guo, and H. Tang, „Effect of Coating MgO on Sticking Behavior during Reduction of Iron Ore Concentrate Fines in Fluidized Bed", *steel research international*, vol. 84, no. 2, pp. 111–118, 2012.

[63] L. Qin, A. Majumder, J. A. Fan, D. Kopechek, and L.-S. Fan, „Evolution of nanoscale morphology in single and binary metal oxide microparticles during reduction and oxidation processes", *J. Mater. Chem. A*, vol. 2, no. 41, pp. 17 511–17 520, 2014.

[64] Z. Cheng, L. Qin, J. A. Fan, and L.-S. Fan, „New Insight into the Development of Oxygen Carrier Materials for Chemical Looping Systems", *Engineering*, vol. 4, no. 3, pp. 343–351, 2018.

[65] Z. Wei, J. Zhang, B. Qin, Y. Dong, Y. Lu, Y. Li, W. Hao, and Y. Zhang, „Reduction kinetics of hematite ore fines with H2 in a rotary drum reactor", *Powder Technology*, vol. 332, pp. 18–26, 2018.

[66] M. Elzohiery, H. Y. Sohn, and Y. Mohassab, „Kinetics of Hydrogen Reduction of Magnetite Concentrate Particles in Solid State Relevant to Flash Ironmaking", *Steel Research International*, 2016.

[67] Y. Qu, Y. Yang, Z. Zou, C. Zeilstra, K. Meijer, and R. Boom, „Reduction Kinetics of Fine Hematite Ore Particles with a High Temperature Drop Tube Furnace", *ISIJ International*, vol. 55, no. 5, pp. 952–960, 2015.

[68] S. K. Kuila, R. Chatterjee, and D. Ghosh, „Kinetics of hydrogen reduction of magnetite ore fines", *International Journal of Hydrogen Energy*, vol. 41, no. 22, pp. 9256–9266, 2016.

[69] D. Spreitzer and J. Schenk, „Fluidization behavior and reducibility of iron ore fines during hydrogen-induced fluidized bed reduction", *Particuology*, vol. 52, pp. 36–46, 2020.

[70] K. Piotrowski, K. Mondal, T. Wiltowski, P. Dydo, and G. Rizeg, „Topochemical approach of kinetics of the reduction of hematite to wüstite", *Chemical Engineering Journal*, vol. 131, no. 1, pp. 73–82, 2007.

[71] R. Morales-Estrella, J. Ruiz-Ornelas, N. Ortiz-Lara, Y. Mohassab, and H. Y. Sohn, „Effect of mechanical activation on the hydrogen reduction kinetics of magnetite concentrate", *Journal of Thermal Analysis and Calorimetry*, vol. 130, no. 2, pp. 713–720, 2017.

[72] A. Pineau, N. Kanari, and I. Gaballah, „Kinetics of reduction of iron oxides by H2 Part I. Low Temperature Reduction of Hematite", *Thermochimica Acta*, vol. 447, no. 1, pp. 89–100, 2006.

[73] A. Pineau, N. Kanari, and I. Gaballah, „Kinetics of reduction of iron oxides by H2 Part II: Low Temperature reduction of magnetite", *Thermochimica Acta*, vol. 456, no. 2, pp. 75–88, 2007.

[74] P. Pourghahramani and E. Forssberg, „Reduction kinetics of mechanically activated hematite concentrate with hydrogen gas using nonisothermal methods", *Thermochimica Acta*, vol. 454, no. 2, pp. 69–77, 2007.

[75] H.-Y. Lin, Y.-W. Chen, and C. Li, „The mechanism of reduction of iron oxide by hydrogen", *Thermochimica Acta*, vol. 400, no. 1, pp. 61–67, 2003.

[76] S.-H. Kim, X. Zhang, Y. Ma, I. R. Souza Filho, K. Schweinar, K. Angenendt, D. Vogel, L. T. Stephenson, A. A. El-Zoka, J. R. Mianroodi, M. Rohwerder, B. Gault, and D. Raabe, „Influence of microstructure and atomic-scale chemistry on the direct reduction of iron ore with hydrogen at 700°C", *Acta Materialia*, vol. 212, p. 116 933, 2021.

[77] J. D. Hancock and J. H. Sharp, „Method of Comparing Solid-State Kinetic Data and Its Application to the Decomposition of Kaolinite, Brucite, and BaCO3", *Journal of the American Ceramic Society*, vol. 55, no. 2, pp. 74–77, 1972.

[78] T. Spee, „Toward the design of a MILD Cyclonic Combustor (MC2) for metal fuels", Master's thesis, Eindhoven University of Technology, 2018.

[79] K. Coenen, F. Gallucci, P. Cobden, E. van Dijk, E. Hensen, and M. van Sint Annaland, „Chemisorption working capacity and kinetics of CO2 and H2O of hydrotalcite-based adsorbents for sorption-enhanced water-gas-shift applications", *Chemical Engineering Journal*, vol. 293, pp. 9–23, 2016.

[80] E. T. Turkdogan and J. V. Vinters, „Gaseous reduction of iron oxides: Part III. Reduction-oxidation of porous and dense iron oxides and iron", *Metallurgical Transactions*, vol. 3, no. 6, pp. 1561–1574, 1972.

[81] A. A. El-Geassy, M. I. Nasr, and M. M. Hessien, „Effect of Reducing Gas on the Volume Change during Reduction of Iron Oxide Compacts", *ISIJ International*, vol. 36, no. 6, pp. 640–649, 1996.

[82] L. Yi, Z. Huang, T. Jiang, L. Wang, and T. Qi, „Swelling behavior of iron ore pellet reduced by H2–CO mixtures", *Powder Technology*, vol. 269, pp. 290–295, 2015.

[83] Y. Qu, L. Xing, L. Shao, Y. Luo, and Z. Zou, „Microstructural characterization and gas-solid reduction kinetics of iron ore fines at high temperature", *Powder Technology*, vol. 355, pp. 26–36, 2019.

[84] P. L. M. Wong, M. J. Kim, H. S. Kim, and C. H. Choi, „Sticking behaviour in direct reduction of iron ore", *Ironmaking & Steelmaking*, vol. 26, no. 1, pp. 53–57, 1999.

[85] J.-H. Shao, Z. Guo, and H.-Q. Tang, „Influence of Temperature on Sticking Behavior of Iron Powder in Fluidized Bed", *ISIJ International*, vol. 51, no. 8, pp. 1290–1295, 2011.

[86] L. Yi, Z. Huang, and T. Jiang, „Sticking of iron ore pellets during reduction with hydrogen and carbon monoxide mixtures: Behavior and mechanism", *Powder Technology*, vol. 235, pp. 1001–1007, 2013.

[87] Z.-X. Di, Z.-Y. Li, R.-F. Wei, Y. Liu, Q.-M. Meng, T.-J. Chun, H.-M. Long, J.-X. Li, and P. Wang, „Sticking behaviour and mechanism of iron ore pellets in COREX pre-reduction shaft furnace", *Ironmaking & Steelmaking*, vol. 46, no. 2, pp. 159–164, 2019.

[88] Q. Zhu, R. Wu, and H. Li, „Direct reduction of hematite powders in a fluidized bed reactor", *Particuology*, vol. 11, no. 3, pp. 294–300, 2013.

[89] C. Kuhn, A. Düll, P. Rohlfs, S. Tischer, M. Börnhorst, and O. Deutschmann, „Iron as recyclable energy carrier: Feasibility study and kinetic analysis of iron oxide reduction", *Appl. in Energy and Combust. Sci.*, p. 100 096, 2022.

[90] F. Thümmler and W. Thomma, „The sintering process", *Metall. Rev.*, vol. 12, no. 1, pp. 69–108, 1967.

[91] S. Sōmiya and Y. Moriyoshi, Eds., *Sintering Key Papers*. Springer Netherlands, 1990.

[92] G. C. Kuczynski, „Self-Diffusion in Sintering of Metallic Particles", *JOM Journal of the Minerals Metals and Materials Society*, vol. 1, pp. 169–178, 1949.

[93] T. Mikami, H. Kamiya, and M. Horio, „The mechanism of defluidization of iron particles in a fluidized bed", *Powder Technology*, vol. 89, no. 3, pp. 231–238, 1996.

[94] K. Kuwagi, T. Mikami, and M. Horio, „Numerical simulation of metallic solid bridging particles in a fluidized bed at high temperature", *Powder Technology*, vol. 109, no. 1, pp. 27–40, 2000.

[95] P. Knight, J. Seville, H. Kamiya, and M. Horio, „Modelling of sintering of iron particles in high-temperature gas fluidisation", *Chemical Engineering Science*, vol. 55, no. 20, pp. 4783–4787, 2000.

[96] X. Gong, B. Zhang, Z. Wang, and Z. Guo, „Insight of Iron Whisker Sticking Mechanism from Iron Atom Diffusion and Calculation of Solid Bridge Radius", *Metall. Mater. Trans. B*, vol. 45, no. 6, pp. 2050–2056, 2014.

[97] C. Lei, Q. Zhu, and H. Li, „Experimental and theoretical study on the fluidization behaviors of iron powder at high temperature", *Chemical Engineering Science*, vol. 118, pp. 50–59, 2014.

[98] J. Li, J. Kong, S. He, Q. Zhu, and H. Li, „Self-agglomeration mechanism of iron nanoparticles in a fluidized bed", *Chem. Eng. Sci.*, vol. 177, pp. 455–463, 2018.

[99] X. Liu, X. Zhang, J. Li, Q. Zhu, N. G. Deen, and Y. Tang, „Regeneration of iron fuel in fluidized beds, Part I: Defluidization experiments and theoretical prediction model", *Powder Technology*, p. 118 182, 2023.

[100] X. Liu, X. Zhang, J. Li, Q. Zhu, N. G. Deen, and Y. Tang, „Regeneration of iron fuel in fluidized beds Part II: Reduction experiments", *Powder Technology*, p. 118 183, 2023.

[101] S. P. Matthew, T. R. Cho, and P. C. Hayes, „Mechanisms of porous iron growth on wustite and magnetite during gaseous reduction", *Metallurgical Transactions B*, vol. 21, no. 4, pp. 733–741, 1990.

[102] Z. Du, Q. Zhu, C. Fan, F. Pan, H. Li, and Z. Xie, „Influence of Reduction Condition on the Morphology of Newly Formed Metallic Iron During the Fluidized Bed Reduction of Fine Iron Ores and its Corresponding Agglomeration Behavior", *steel research international*, vol. 87, no. 6, pp. 789–797, 2015.

[103] X. Zhang, S. He, H. Sun, Q. Zhu, J. Li, and H. Li, „Mechanism of surface morphology evolution in the reduction of fine iron ore in a conical fluidized bed reactor", *Chem. Eng. Sci.*, vol. 220, p. 115 468, 2020.

[104] H. C. H. Rumpf, „Zur Theorie der Zugfestigkeit von Agglomeraten bei Kraftübertragung an Kontaktpunkten", *Chemie Ingenieur Technik*, vol. 42, no. 8, pp. 538–540, 1970.

[105] G. Matsumura, „Sintering of iron wires", *Acta Metallurgica*, vol. 19, no. 8, pp. 851–855, 1971.

[106] H. F. Fischmeister and R. Zahn, „The Mechanism of Sintering of α-Iron", in *Modern Developments in Powder Metallurgy*, Springer US, 1966, pp. 12–25.

[107] A. T. Gorton, G. Bitsianes, and T. L. Joseph, „Thermal expansion coefficients for iron and its oxides from X-ray diffraction measurements at elevated temperatures", *Transactions of the Metallurgical Society of AIME*, vol. 233, no. 8, pp. 1519–1525, 1965.

[108] A. Navrotsky, C. Ma, K. Lilova, and N. Birkner, „Nanophase Transition Metal Oxides Show Large Thermodynamically Driven Shifts in Oxidation-Reduction Equilibria", *Science*, vol. 330, no. 6001, pp. 199–201, 2010.

[109] S. Schönecker, X. Li, B. Johansson, S. K. Kwon, and L. Vitos, „Thermal surface free energy and stress of iron", *Sci. Rep.*, vol. 5, no. 1, 2015.

[110] L. Himmel, R. F. Mehl, and C. E. Birchenall, „Self-Diffusion of Iron in Iron Oxides and The Wagner Theory of Oxidation", *JOM Journal of the Minerals Metals and Materials Society*, vol. 5, no. 6, pp. 827–843, 1953.

[111] F. S. Buffington, K. Hirano, and M. Cohen, „Self diffusion in iron", *Acta Metall.*, vol. 9, no. 5, pp. 434–439, 1961.

[112] C. E. A. G. van Gool, L. C. Thijs, W. J. S. Ramaekers, J. A. van Oijen, and L. P. H. de Goey, „Particle Equilibrium Composition model for iron dust combustion", *Applications in Energy and Combustion Science*, p. 100 115, 2023.

[113] O. Levenspiel, *Chemical Reaction Engineering*. WILEY, 1998, 704 pp.

[114] R. Nicolle and A. Rist, „The mechanism of whisker growth in the reduction of wüstite", *Metall. Trans. B*, vol. 10, no. 3, pp. 429–438, 1979.

[115] H. Wang and H. Y. Sohn, „Effects of Reducing Gas on Swelling and Iron Whisker Formation during the Reduction of Iron Oxide Compact", *Steel Res. Int.*, vol. 83, no. 9, pp. 903–909, 2012.

[116] E. Lucon, K. Abiko, M. Lambrecht, and B. Rehmer, „Tensile Properties of Commercially Pure, High Purity and Ultra High Purity Iron: Results of an International Round-Robin", Tech. Rep., 2015.

[117] N. C. Stevens, „Design of a high temperature lab-scale fluidized bed", Master's thesis, Eindhoven University of Technology, 2021.

[118] D. W. J. Lelivelt, „Characterization of the fluidization and reduction behavior of cyclically combusted and reduced iron(-oxide)", Master's thesis, Eindhoven University of Technology, 2022.

[119] S. He, H. Sun, C. Hu, J. Li, Q. Zhu, and H. Li, „Direct reduction of fine iron ore concentrate in a conical fluidized bed", *Powder Technology*, vol. 313, pp. 161–168, 2017.

[120] T. Zhang, C. Lei, and Q. Zhu, „Reduction of fine iron ore via a two-step fluidized bed direct reduction process", *Powder Technology*, vol. 254, pp. 1–11, 2014.

[121] Y. Zhong, Z. Wang, Z. Guo, and Q. Tang, „Defluidization behavior of iron powders at elevated temperature: Influence of fluidizing gas and particle adhesion", *Powder Technology*, vol. 230, pp. 225–231, 2012.

[122] Y.-W. Zhong, Z. Wang, X.-Z. Gong, and Z.-C. Guo, „Sticking behavior caused by sintering in gas fluidisation reduction of haematite", *Ironmaking & Steelmaking*, vol. 39, no. 1, pp. 38–44, 2012.

[123] Y. Zhong, J. Gao, Z. Wang, and Z. Guo, „Influence of Particle Size Distribution on Agglomeration/defluidization of Iron Powders at Elevated Temperature", *ISIJ International*, vol. 57, no. 4, pp. 649–655, 2017.

[124] D. Spreitzer and J. Schenk, „Iron Ore Reduction by Hydrogen Using a Laboratory Scale Fluidized Bed Reactor: Kinetic Investigation—Experimental Setup and Method for Determination", *Metallurgical and Materials Transactions B*, vol. 50, no. 5, pp. 2471–2484, 2019.

[125] D. Kunii and O. Levenspiel, *Fluidization Engineering*, 2nd. Elsevier, 1991.

[126] S. Ergun, „Fluid flow through packed columns", *Chemical Engineering Progress*, vol. 48, no. 2, pp. 89–94, 1952.

[127] C. C. Xu and J. Zhu, „Prediction of the minimum fluidization velocity for fine particles of various degrees of cohesiveness", *Chemical Engineering Communications*, vol. 196, no. 4, pp. 499–517, 2008.

[128] M. Mihajlovic, I. Roghair, and M. van Sint Annaland, „High temperature fluidization - influence of inter-particle forces on fluidization behavior", in *Progress in Applied CFD – CFD2017*, SINTEF Academic Press, 2017, pp. 107–114.

[129] J. Seville, C. Willett, and P. Knight, „Interparticle forces in fluidisation: a review", *Powder Technology*, vol. 113, no. 3, pp. 261–268, 2000, Neptis Symposium on Fluidization- Present and Future.

[130] C. Xu and J. Zhu, „Experimental and theoretical study on the agglomeration arising from fluidization of cohesive particles—effects of mechanical vibration", *Chemical Engineering Science*, vol. 60, no. 23, pp. 6529–6541, 2005.

[131] C. R. Wilke, „A Viscosity Equation for Gas Mixtures", *The Journal of Chemical Physics*, vol. 18, no. 4, pp. 517–519, 1950.

[132]   M. W. Chase jr., „NIST-JANAF Themochemical Tables, Fourth Edition", *Journal of physical and chemical reference data, Monograph 9*, pp. 1–1951, 1998.

[133]   Y. Hidaka, T. Anraku, and N. Otsuka, „Deformation of Iron Oxides upon Tensile Tests at 600–1250°C", *Oxidation of Metals*, vol. 59, no. 1/2, pp. 97–113, 2003.

[134]   A. Kamranian Marnani, A. Bück, S. Antonyuk, B. van Wachem, D. Thévenin, and J. Tomas, „The Effect of the Presence of Very Cohesive Geldart C Ultra-Fine Particles on the Fluidization of Geldart A Fine Particle Beds", *Processes*, vol. 7, no. 1, 2019.

[135]   J. Oh and D. Noh, „The reduction kinetics of hematite particles in H_2 and CO atmospheres", *Fuel*, vol. 196, pp. 144–153, 2017.

[136]   Y. Qu, „Experimental Study of the Melting and Reduction Behaviour of Ore Used in the HIsarna Process", PhD thesis, 2013.

[137]   Y. Qu, Y. Yang, Z. Zou, C. Zeilstra, K. Meijer, and R. Boom, „Thermal Decomposition Behaviour of Fine Iron Ore Particles", *ISIJ International*, vol. 54, no. 10, pp. 2196–2205, 2014.

[138]   M. E. Choi and H. Y. Sohn, „Development of green suspension ironmaking technology based on hydrogen reduction of iron oxide concentrate: rate measurements", *Ironmaking & Steelmaking*, vol. 37, no. 2, pp. 81–88, 2010.

[139]   H. Wang and H. Y. Sohn, „Hydrogen Reduction Kinetics of Magnetite Concentrate Particles Relevant to a Novel Flash Ironmaking Process", *Metallurgical and Materials Transactions B*, vol. 44, no. 1, pp. 133–145, 2012.

[140]   Z. Yuan, H. Y. Sohn, and M. Olivas-Martinez, „Re-oxidation Kinetics of Flash-Reduced Iron Particles in H_2-H_2O(g) Atmosphere Relevant to a Novel Flash Ironmaking Process", *Metallurgical and Materials Transactions B*, vol. 44, no. 6, pp. 1520–1530, 2013.

[141]   L. Boone, „Preheating combustion air in an iron particle Jet-in-Hot-Coflow burner", Master's thesis, Eindhoven University of Technology, 2022.

Publications & conference contributions

Publications

1. C.J.M. Hessels, T.A.M. Homan, N.G. Deen, and Y. Tang. Reduction kinetics of combusted iron using hydrogen. *Powder Technology, 407 (2022) 117540.*

2. L. Choisez, N.E. van Rooij, C.J.M. Hessels, A.K. da Silva, I.R. Souza Filho, Y. Ma, L.P.H. de Goey, H. Springer, and D. Raabe. Phase transformations and microstructure evolution during combustion of iron powder. *Acta Materialia, 239 (2022) 118261.*

3. C.J.M. Hessels, D.W.J. Lelivelt, N.C. Stevens, Y. Tang, N.G. Deen, and G. Finotello. Minimum fluidization velocity and reduction behavior of combusted iron powder in a fluidized bed. *Fuel, 342 (2023) 127710.*

4. C.J.M. Hessels, A.H.J. Smeets, G. Finotello, N.G. Deen, and Y. Tang. Sintering behaviour of combusted iron powder in a packed bed reactor with nitrogen and hydrogen. *Particuology, 83 (2023) 8-17.*

5. X. Liu, C.J.M. Hessels, N.G. Deen, and Y. Tang. CFD-DEM investigation on the agglomeration behavior of micron-sized combusted iron fines. *Fuel, 346 (2023) 128219.*

Conference contributions

1. C.J.M. Hessels, G. Finotello, Y. Tang, T.A.M. Homan, and N.G. Deen. Prediction of high temperature minimum fluidization of cohesive metallic particles (presentation). *11th International Conference on Multiphase Flow (ICMF 2023)*, Kobe, Japan (2023).

2. C.J.M. Hessels. IJZERsterke energietransitie met vuurwerk (webinar). *Koninklijk Instituut van Ingenieurs (KIVI), afdeling Elektrotechniek*, Eindhoven, the Netherlands (2023).

3. C.J.M. Hessels, J. Hameete, G. Finotello, Y. Tang, T.A.M. Homan, and N.G. Deen. Metal fuel production: fluidized bed reduction (presentation). *Combura 2022*, Soesterberg, the Netherlands (2022).

4. C.J.M. Hessels, Y. Tang, G. Finotello, T.A.M. Homan, and N.G. Deen. Direct reduction of combusted iron (poster). *1st Workshop on Metal-enabled Cycle of Renewable Energy (MECRE)*, Eindhoven, the Netherlands (2022).

5. C.J.M. Hessels, C.-C. Huang, A.H.J. Smeets, G. Finotello, Y. Tang, T.A.M. Homan, and N.G. Deen. Reduction and sintering behaviour of combusted iron powder in a packed bed reactor (presentation, given by C.-C. Huang). *1st International Workshop on Reacting Particle-Gas Systems*, Bochum, Germany (2022).

6. C.J.M. Hessels, D.W.J. Lelivelt, G. Finotello, Y. Tang, and N.G. Deen. Minimum fluidization velocity of combusted iron fines using H_2 and N_2 in a lab-scale fluidized bed (presentation). *24th Fluidized Bed Conversion Conference (FBC24)*, Gothenburg, Sweden (2022).

7. C.J.M. Hessels, T.A.M. Homan, Y. Tang, and N.G. Deen. Iron powder regeneration using H_2 as part of the metal fuel cycle (presentation). *Combura 2021*, Soesterberg, the Netherlands (2021).

8. C.J.M. Hessels, Y. Tang, T.A.M. Homan, and N.G. Deen. Modeling the direct reduction of iron oxide powder using experimentally-measured reaction kinetics (online presentation). *14th International Conference on Computational Fluid Dynamics in the Oil & Gas, Metallurgical and Process Industries (CFD2020)*, Trondheim, Norway (2020).

9. C.J.M. Hessels, X. Liu, Y. Tang, T.A.M. Homan, and N.G. Deen. Regenerating iron for carbon-neutral energy storage (presentation, together with X. Liu). *16th Netherlands Process Technology Symposium (NPS16)*, Eindhoven, the Netherlands (2019).

10. C.J.M. Hessels, T.A.M. Homan, Y. Tang, and N.G. Deen. Storing green energy in a grey powder (poster). *Combura 2019*, Soesterberg, the Netherlands (2019).

11. C.J.M. Hessels, Y. Tang, T.A.M. Homan, and N.G. Deen. Derusting the energy carrier of the future (poster). *Burgers Symposium*, Lunteren, the Netherlands (2019).

12. C.J.M. Hessels, Y. Tang, T.A.M. Homan, and N.G. Deen. Dealing with rust: a solution to the energy problem (pitch). *Burgers Symposium*, Lunteren, the Netherlands (2018).

Acknowledgements

Although obtaining a PhD is often described as a personal achievement, the opposite is true. This thesis would not have been possible without the support, help, discussions, advice and (occasionally needed) distraction by many valuable colleagues, friends, and family. In this section I would like to acknowledge them.

First, I would like to thank my promotor: Niels. I am very glad that you gave me the opportunity to do a PhD. Evermore since there wasn't even a project available when I finished my master's degree. I am still amazed by how you can make time in your busy schedule for all your PhD's for both minor questions as well as in-depth research discussions, while simultaneously being the head of the group. I truly enjoyed your social positive nature, from handing out Christmas gifts, your jokes during progress meetings, to joining for lunch in the "Vuurplaats". I also appreciate your patience when I was again going into one of my many sidetrack-explorations.

I would also like to thank my co-promotors: Yali and Tess. It was an honor to be both your first PhD student. Yali, I really appreciate that you always made time for me, and I am grateful for you helping me break through my first paper gridlock. Your critical view and honest advice were exactly what was needed to balance my own stubbornness. Tess, I enjoyed your positive vibe whenever we talked. You always made me realize how much I had accomplished and made me truly proud of my own work.

Giulia, thank you very much for all your advice, discussions, and time. I really appreciate that you were always available for ad-hoc meetings. Our joint supervision of many bachelor and masters students was one of the highlights of my PhD. I also greatly appreciate you allowing me to use some of your personal grant for my research.

Nico, thank you for your advice, especially in the beginning of my PhD. I am 100% sure I would have never even started my PhD without your supervision and down-to-earth nature during my masters.

Several bachelors and masters' students had to endure me as their supervisor during their studies. Out of these I would like to specifically call out Anke, Daniël, and Nicole. Without your contributions this thesis would not have been possible.

I would like to thank my opponents: Marc Geers, Ruud van Ommen, David Pallarès, and Ekaterina Makarova. I feel very honored that each of you set aside some of your valuable time to evaluate my thesis and to attend my defense.

I also would like to thank the following people for allowing me to use their equipment and to learn from their immense experience: (1) Marc van Maris and Mark Vissers of the Multiscale Lab; (2) Solomon Wassie and Ivo Roghair of the Chemical Process Intensification research group; (3) Zhiyuan Chen and Yongxiang Yang of the Metals Production, Refining and Recycling research group at Delft University of Technology; (4) Laurine Choisez and Isnaldi Souza Filho of the Sustainable Synthesis of Materials group of the Max-Planck-Institut für Eisenforschung. Laurine, our online and in person discussions were besides insightful also always very enjoyable.

Marjan, thank you for all your advice, humor, and support. Our coffee chats, Thursday drinks and teams' meetings were truly invaluable. I would also like to thank the TFE lab technicians: Bart, Hans, Henri, Jan, Martin, Theo, Frank, and Thijs for their support during the project.

Work is so much easier when you have nice colleagues. First, I would like to thank my colleagues in the offices GEM-N 1.21 & GEM-Z 1.114: Aromal, Robin, Camila, Xin, Chih-Chia, Thijs, Ravi, Swagnik, Pourya, and Max. Thinking back at that time when we made a puzzle together still makes me laugh every time. Or the multiple times when people in the other offices asked us to be quiet. I truly landed in the best office of our group.

I would like to specifically call out office colleagues Thijs and Xin. Thijs, our brainstorming about propositions, hunt for each other's "roast"-material, and "guess the grade"-games were always very enjoyable. Our shared style of humor made it great to be in the office and almost hard to spend time in the lab. Xin, we shared not only an office, but also a research topic, supervisors, and even progress meetings. I learned a lot from you, both academically and socially.

I also very much appreciated my interactions with the "metal fuel group", with in particular Daoguan, Jesse, Niek, and Tim. Your contributions to my research and my work-life were invaluable. Similarly, many thanks to the "intervision group" for all the funny, social, and occasionally very useful Thursday' lunches. Thanks to Mengting for all the nice coffee breaks.

Special thanks to Abhijit, Michel, Noud, and Robbert for all the enjoyable conversions. Of course, thanks to all other colleagues in the combustion technology → multiphase and reactive flow → power and flow research group. I wish all of you a great time in HEL (heat exchange lunch).

Besides my colleagues, I also would like to thank my friends. Shout out to my international friends: Emma & Fredrik, Evelyn, Matthew and Helena. The fact that we still are in contact after so many years is truly amazing. Emma & Fredrik, our in-person interactions and skype sessions, not only change the way I see things, but also who I am (for the better).

Helen, you have for the last 2 years always been on my side, both in the office and at home. As we often joke, both in research and in life, we are yin and yang. Thanks for everything.

Harmen en Thomas. Bedankt dat jullie mijn paranimfen willen zijn. Jullie hebben beiden mijn gehele PhD-tijd van dichtbij meegemaakt en kennen al mijn up's-en-down's. De avondprogramma's geven mij naast de katers en vermoeidheid ook altijd heel veel energie. Verder wil ik de volgende vrienden bij naam bedanken: David, Kyrola, Jetze, Sebastian, en Jeroen. Bedankt voor alle intens leuke avonden.

Als laatste wil ik mijn familie bedanken. Pa en ma, bedankt dat jullie mij altijd alle vrijheid en steun hebben gegeven, zowel voor mijn studie, mijn PhD, de boerderij en eigenlijk mijn hele leven.

About the author

Conrad Hessels was born on the 12th of April 1994 in Breda, the Netherlands. After finishing his pre-univerisity study (VWO) at het Dongemond College in Raamsdonkveer, he started his bachelor study in mechanical engineering at Eindhoven University of Technology (TU/e) in 2012. He subsequently started his master in mechanical engineering in 2015 within in power and flow research group at TU/e. He did his internship at the Volvo Car Corporation in Gothenburg, Sweden, working on post-processing of metal and optical petrol engine test data. He subsequently did his master's thesis on the use of spontaneous Raman spectroscopy for quantitative analysis of non-premixed flames. His master thesis was awarded the "TU/e Mechanical Engineering MSc Thesis Award 2018" as well as the 2nd prize of the "KHMW Nederlandse Gasindustrie Prijzen 2018". From May 2018 he started a PhD project at TU/e of which the results are presented in this dissertation. In 2022 he was a member of the research assessment committee for the department of aerospace engineering at Delft University of Technology. He has also been a board member of the section Mechanics of the Royal Dutch Society of Engineers (KIVI) since 2015 and co-owner of his family's farm in Lage Zwaluwe since 2020.